Thermal induced cracking of granite:
Laboratory investigations and numerical simulations

To the Faculty of Geosciences, Geoengineering and Mining

of the Technischen Universität Bergakademie Freiberg

approved

THESIS

to attain the academic degree of

Doctor of Engineering

Dr.-Ing.

submitted

by Dipl.-Ing. Fei, Wang

born on the Jan. 06, 1990 in Shandong, China

Reviewers: Prof. Dr.-Ing. habil. Heinz Konietzky, Freiberg, Germany

Prof. Dr. Arno Zang, Potsdam, Germany

Prof. Dr. Yawei Li, Wuhan, China

Dr. Philipp Hartlieb, Leoben, Austria

Date of the award: 03.03.2020

Acknowledgements

First and foremost, I want to thank my supervisor Prof. Heinz Konietzky. His enthusiasm for scientific work was contagious and motivational for me during my Ph.D. study at the TU Bergakademie Freiberg, Germany. He has taught me how a good research in rock mechanics is done. I appreciate all his contributions of time, inspirations, and careful guidance to make my research work more comprehensive and innovative. I also want to express my gratitude to Prof. Konietzky and his wife Ms. Haina Chen-Konietzky for the delicious tea and dessert that they prepared for us during Christmas time in conjunction with the annual 'Bergparade'. It will always be a wonderful memory of the Christmas holidays.

The group at the Geotechnical Institute has been a source of friendship. I received good advices and experienced a wonderful collaboration. Dr. Martin Herbst who is also my office roommate, has always been helpful and has given specific support in numerical modelling. As the leader of the rock mechanical laboratory, Dr. Thomas Frühwirt and I worked together on the granite heating experiments. His professional abilities in lab testing enabled us to finish the planned work on time. Dr. Yajie Dai from WUST shared the DIC knowledge with me and made a big contribution in DIC analysis. Our group's administrative assistant Mrs. Angela Griebsch who keep us organized was always ready to help. To a large extend I enjoyed the leisure time with my Chinese friends and colleagues, especially my roommate Mr. Zhengyang Song, I am grateful for the pleasant time spent with them. I would also like to thank my sport friends, including Mr. Yufeng Zhao, Mr. Min Zhang, Dr. Natalie Krupko etc. for doing workout/sport together in Freiberg.

I gratefully acknowledge China Scholarship Council (CSC), for providing me financial support to carry out my research in Germany.

Lastly, I would like to thank all my family members for their unconditional love, care, tolerance, and encouragement. On a more personal level, I also want to thank Karolina for the continuous love and accompany.

Fei Wang

TU Bergakademie Freiberg

June 2019

II

Abstract

The impact of temperature up to 1000 °C on physical, mechanical, and thermal properties of Eibenstock granite (EG) were investigated. Thermo-mechanical behaviors of EG applying heating rates of 5 °C/min, 200 °C/min, 300 °C/min, and according to ISO 834 standard fire curve were also studied. A supersonic frequency induction heating system was used to conduct the required heating scenarios and to perform uniaxial compression tests under the desired temperatures. P-wave velocity test and Digital Image Correlation (DIC) technique were used for analyzing the cracking behavior of granite with various heating scenarios. Lab testing results show that except for friction angle, all the other investigated granite properties show obvious temperature-dependent characteristics. The maximum temperature has the dominant impact on mechanical properties of granite sample, while the influence of heating rate is relatively small. The DIC analysis shows the crack initiation and progressive crack propagation before the main crack is formed at failure. The final failure patterns prove that different heating scenarios lead to different microcrack structures and consequently influence the failure mode at the macroscopic scale.

General temperature-dependent relations of properties for most granites have been deduced based on comprehensive data compilation. These relations are combined with classical Mohr-Coulomb model with strain softening and tension cut-off. A new methodology combining Weibull functions and the real mineral composition of granite is also proposed. It overcomes the shortcomings of using existing methods for the heterogeneity characterization of rocks at the grain size level. The proposed modelling strategy is able to duplicate the thermal induced cracking which results in reduced peak strength, pronounced softening and transition from brittle to ductile behaviour. The simulation results reveal that the thermal induced microcracks are randomly distributed across the whole sample. UCS reduction of granite due to heating is mainly caused by the increase of shear failures at high temperatures. The dominant impact of α-β quartz transition is widening pre-existing cracks rather than the formation of new microcracks. The small strength variation in respect to different heating rates is caused by a different induced cracking structure. The presented results help to understand the damage mechanisms of granite caused by fire or other high temperature conditions, and can be used to develop guidelines for repair and maintenance as well as assessment of risks of tunnels and historical buildings after fire accidents.

IV

Table of Contents

List of Figures

XIII

List of Tables

Notation

B	Thickness of disc
C	Correlation coefficient
$C_{vi}(T)$	Temperature-dependent specific heat of element i
C_v, C_v/C_{v0}	Specific heat and corresponding normalized value
D	Diameter of disc
E, E/E_0	Young's modulus and corresponding normalized value
E_c	Young's modulus calculated from peak axial stress and strain
E_{input}	Back-calculated Young's modulus
E_s	Young's modulus deduced from linear part of stress-strain curve
$E(x)$	Mean value of Weibull distribution
$E_i(T)$	Temperature-dependent Young's modulus of element i
$F(x)$	Cumulative distribution function
G	Shear modulus
K	Bulk modulus
L, ΔL	Length of the sample and length increment
P_{max}	Maximum load
P_0, P_i	Property of the sample and the element i
T, T_0, T_{max}	Temperature, room temperature, and maximum temperature
$T_{\alpha\text{-}\beta}$	Temperature of α-β quartz transition
$Var(x)$	Variance of Weibull distribution
ΔT	Temperature increment
∇T	Temperature gradient
Δz_{min}	Smallest width of adjoining zone in normal direction
Γ	Gamma function
a, b	Coefficients of linear equation
c, c/c_0	Cohesion and corresponding normalized value
f	Specifies the grey levels of the reference states ($\underline{X}$)
$f_{Cv/Cv0}$	Fitting equation of normalized specific heat
$f_{c/c0}$	Fitting equation of normalized cohesion
$f_{E/E0}$	Fitting equation of normalized Young's modulus
$f_{k/k0}$	Fitting equation of normalized thermal conductivity
$f_{\alpha t/\alpha t0}$	Fitting equation of normalized linear thermal expansion coefficient
$f_{v/v0}$	Fitting equation of normalized Poisson's ratio
$f_{\sigma t/\sigma t0}$	Fitting equation of normalized tensile strength
$\overline{f_D}$, $\overline{g_D}$	Averages of grey level values on subset D
$f_{\varphi/\varphi0}$	Fitting equation of normalized friction angle

g	Grey levels of the deformed states ($\underline{x}$)
k, k/k_0	Thermal conductivity and corresponding normalized value
m	Shape parameter of Weibull distribution
q_i	Heat-flux vector
q_v	Volumetric heat-source intensity
t	Time
p_i	Probability of discrete random variable
x	Weibull distributed random variable
x_0	Scale parameter of Weibull distribution
x_i	Weibull random variable for element i
x_u	Threshold value of Weibull variable
$\alpha_{ti}(T)$	Temperature-dependent linear thermal expansion coefficient of element i
α_t, α_t/α_{t0}	Linear thermal expansion coefficient and corresponding normalized value
β_t, β_t/β_{t0}	Volumetric thermal expansion coefficient and corresponding normalized value
δ_{ij}	Kronecker delta
δ_σ, δ_ε	Relative error of stress and strain
σ_t, σ_t/σ_{t0}	Tensile strength and corresponding normalized value
ε^e, ε^p	Elastic strain and plastic strain
ε^{pt}, ε^{ps}	Plastic tension strain and plastic shear strain
ε_v	Volumetric strain
v, v/v_0	Poisson's ratio and corresponding normalized value
$v_i(T)$	Temperature-dependent Poisson's ratio of element i
ρ	Density
$\rho(T)$	Temperature-dependent density
σ_1, σ_3	Maximum and minimum principal stress
σ_c, ε_{1c}	Peak axial stress and axial strain obtained from lab test
σ_{cs}, ε_{cs}	Peak axial stress and axial strain obtained from simulation
$\Delta\sigma_{ij}$, $\Delta\varepsilon_{ij}$	Thermal stress and strain increments
φ, φ/φ_0	Friction angle and corresponding normalized value
$\varphi_i(T)$	Temperature-dependent friction angle of element i
ψ	Dilation angle

1 Introduction

Due to the demand for high temperature applications in geosciences and geoengineering, the study of the thermo-mechanical behavior of rocks at high temperatures has become of great importance (Vázquez et al. 2015; Kumari et al. 2017a). Understanding the thermo-mechanical behavior of rocks is necessary for safe and effective geoengineering applications, especially at great depths like geothermal energy extraction, deep geological disposal of nuclear waste, deep mining, fire accidents in tunnels and mines etc. As one of the most common rocks on earth, granite is often met in underground constructions like nuclear waste repositories, mines and tunnels, or serves as foundation for buildings, bridges or dams. In general granite is very resistant, but under high temperature impact like generated in geothermal processes or during a fire the properties can change significantly. The main mechanism of this change is attributed to the generation or coalescence of thermal cracks (Heuze 1983; Dwivedi et al. 2008; Gautam et al. 2016). These irreversible damages reduce strength and integrity of the granite.

Besides deep geoengineering applications like tunnels also historical sites, buildings, sculptures etc. are often damaged by high temperatures during fire accidents (Larsson 2006; Sippel et al. 2007; Nordlund et al. 2014). In Europe natural stones were often used as building material and numerous historical buildings have been built from rocks such as granite (Hajpál 2010; Freire-Lista et al. 2016). These buildings have been frequently damaged by fire in history till present (Hajpál 2002), such as the disastrous fire accident of the Notre Dame Cathedral in 2019 (Figure 1-1). During the last twenty years a number of tunnel fires with fatalities have also taken place all over the world (Larsson 2006). Rocks such as granite, gneiss, sandstone etc. can be quickly exposed to high temperatures caused by a tunnel fire (Nordlund et al. 2014). However, the understanding of rock behavior during fire is limited, and there is still a lack of an unequivocal approach for the assessment of rock damaged by fire (Hajpál 2002; Sippel et al. 2007; Nordlund et al. 2014). Although the temperature influence on rocks has been investigated by many researchers (Heuze 1981; Dwivedi et al. 2008; Vázquez et al. 2015; Gautam et al. 2016; Kumari et al. 2017b), the results obtained are usually based on slow heating rates and the mechanical properties are obtained at room temperature. Only limited research efforts have been made in the area of fire-induced damage of rocks (Nordlund et al. 2014).

This study aims at investigating the physical, mechanical, and thermal properties of granite for various thermal scenarios including fire conditions, and developing a new numerical scheme to simulate the thermal induced damage of granite. The research strategy underlying this thesis is illustrated in Figure 1-2.

Figure 1-1 Fire accident of Notre-Dame Cathedral in Paris (Wikipedia 2019)

Thermal Induced Cracking of Granite
Introduction and state of the art (chapter 1 and 2)

General analysis of thermo-mechanical properties of granites at elevated temperatures (chapter 2)

Lab tests: Thermo-mechanical properties of Eibenstock granite under temperature (chapter 3)

Development of constitutive law incl. sensitivity analysis of thermo-mechanical properties and spatial parameter distributions (chapter 5 and 6)

Lab tests: Properties of Eibenstock granite after heat treatments (chapter 4)

Numerical simulation of Eibenstock granite (chapter 7)

Conclusions and outlook (chapter 8)

Figure 1-2 Research strategy and structure of thesis

2 State of the art

2.1 Theoretical background of thermal cracking of rocks

High temperatures have an obvious impact on physical and mechanical properties of rocks. These changes are complex and different for different types of rock (Brotóns et al. 2013; Gautam et al. 2016). Like many other brittle materials, granites can be damaged by the accumulation of internal stresses induced by thermal loading. Thermal stresses are mainly controlled by (a) the constituents of the rocks (minerals and pore fillings have different thermal expansion characteristics), (b) thermal expansion anisotropy within individual minerals and, (c) thermal gradients (Yong and Wang 1980; Heap et al. 2013; Wang and Konietzky 2019).

Johnson et al. (1978) proposed three models to demonstrate the importance of the mismatch of thermal expansions of neighboring grains and illustrate why both, grain-boundary and intra-granular cracking occur. The bicrystal model (see Figure 2-1) is used to illustrate the development of intergranular cracks. Isotropic crystal 1 and crystal 2 have linear thermal expansion coefficients α_{t1} and α_{t2}, elastic moduli E_1 and E_2, and Poisson's ratios v_1 and v_2. They are bonded along a planar boundary with a temperature increment ΔT. Crystal 1 attempts to expand $\alpha_{t1}\cdot\Delta T$, whereas the crystal 2 expands $\alpha_{t2}\cdot\Delta T$. These expansions are not compatible, and intermediate intergranular stresses develop to constrain the different expansions. Crystal 1 is restricted by a compressive stress which is equal to the tensile stress in crystal 2. The tensile stress σ_t in crystal 2 is given by (compression is positive) (Johnson et al. 1978):

$$\sigma_t = (\alpha_{t2} - \alpha_{t1})\Delta T \frac{E_1 E_2}{(1-v_2)E_1 + (1-v_1)E_2} \tag{2-1}$$
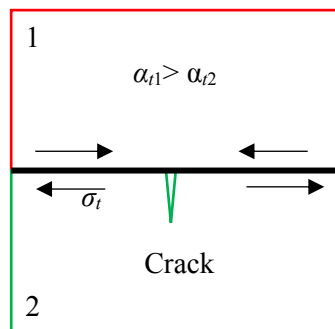
Figure 2-1 Bicrystal model (modified from Johnson et al. 1978)

Because the bicrystal model is not capable to illustrate the development of grain boundary cracks, a spherical-inclusion model (see Figure 2-2) is built. This model simulates a spherical, isotropic inclusion 1 imbedded in a finite, isotropic matrix 2. For a uniform temperature increase, a hydrostatic stress σ_h develops in the inclusions equal to (Johnson et al. 1978):

$$\sigma_h = \frac{2(\alpha_{t1} - \alpha_{t2})\Delta T E_1 E_2}{(1+\nu_2)E_1 + 2(1-2\nu_1)E_2} \tag{2-2}$$

where subscripts 1 and 2 refer to inclusion and matrix, respectively. The radial stress σ_r and tangential stress σ_θ induced in the surrounding matrix in spherical coordinates are (Davidge and Green 1968; Johnson et al. 1978):

$$\sigma_r = \frac{\sigma_h R^3}{r^3}, \ \sigma_\theta = -\frac{\sigma_h R^3}{2r^3} \tag{2-3}$$

where R is the radius of the inclusion, and r is the radial distance from its center.

If $\alpha_{t1} > \alpha_{t2}$, radial cracks are likely to form in the adjacent matrix (Figure 2-2a); if $\alpha_{t1} < \alpha_{t2}$, thermal induced microcracks should form at the interface (Figure 2-2b).

(a) $\alpha_{t1} > \alpha_{t2}$ (b) $\alpha_{t1} < \alpha_{t2}$
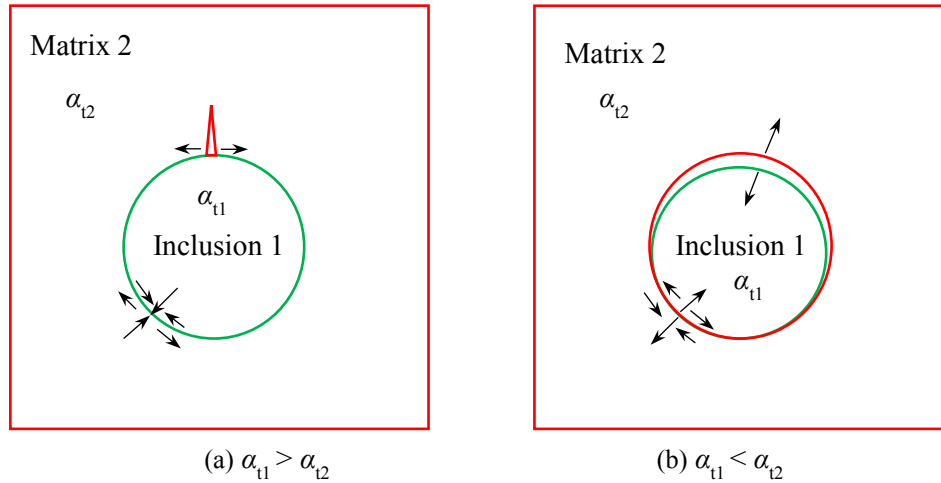
Figure 2-2 Sketch of spherical-inclusion model (modified from Johnson et al. 1978)

In a monomineralic aggregate like Quartzite, the greater the crystallographic mismatch of neighboring grains, the greater the intergranular stresses. The maximum tensile stress (fracture is assumed not to occur) in the Quartzite is given approximately by (Johnson et al. 1978):

$$\sigma_{max} = (\alpha_{tc} - \alpha_{ta})\Delta T \frac{2E_a E_c}{E_a + E_c} \tag{2-4}$$

where subscripts refer to the a and c crystallographic axes. Due to the α-β transition of quartz at 573 °C, thermal expansion and Young's modulus will change significantly, thus leading to a significant thermal stress variation.

2.2 Temperature-dependent properties

Many researchers have conducted lab tests to investigate the physical properties and the mechanical behavior of granites at room temperature after heating or directly at elevated temperatures (see Table 2-1). Since different granites have different property values, normalized values are used to detect tendencies without considering the influence of the individual granite type. Normalized property values P_t/P_{t0} relate the property values at elevated temperature or property value at room temperature after heating to the desired temperature (P_t) to the value at room temperature (P_{t0}) without any heating. The selected mechanical and thermal properties of granite are shown as functions of temperature in Figure 2-3 and Figure 2-4, respectively. The corresponding fitting equations (Wang and Konietzky 2019) are documented in Table 2-1.

Generally, tensile strength of granites decreases with increasing temperature from 25 to 1050 °C. The tensile strength variation with increasing temperatures has the greatest rate of change at $T_{\alpha\text{-}\beta}$ (α-β quartz transition) of about 573 °C (see Figure 2-3a). Cohesion will generally decrease with increasing temperatures (see Figure 2-3b). However, the temperature dependency of friction angle is less significant and to some extend questionable (Wang and Konietzky 2019). Young's modulus usually decreases with increasing temperatures but some granites exhibit a slight increase within a certain temperature range (e.g. 25 to 200 °C) (see Figure 2-3c). Poisson's ratio decreases gradually with increasing temperature between 25 °C and 600 °C, but the value is likely increasing strongly beyond a critical temperature (around 600 °C) (see Figure 2-3d). Thermal expansion coefficients will increase sharply before the phase transition of quartz at $T_{\alpha\text{-}\beta} = 573$ °C and then reduce strongly within a short time (see Figure 2-4a). However, granite could also experience another further jump in thermal expansion between 800 and 900 °C due to a further phase-transition of quartz to hexagonal tridymite (Hartlieb et al. 2016). The increase of specific heat with temperature will experience a discontinuity close to the α-β transition (see Figure 2-4b), while the thermal conductivity show a continuous decrease with rising temperature (see Figure 2-4c).

Table 2-1 Data compilation of temperature-dependent properties of granite (see Fig. 2-3 and 2-4)

Property	Fitting equations
Tensile strength	Remiremont granite, Charcoal granite, Senones granite, Westerly granite, Indian granite (Dwivedi et al. 2008); Patrik granite, Mauthausen granite (Török and Török 2015). $$f_{\sigma_t/\sigma_{t0}} = \begin{cases} 0.9912(1-4.10T/2483.30)^{(1/4.10)}, & 0°C \le T \le 600°C \\ 2.610e^{-0.0036T}, & 600°C < T \le 1050°C \end{cases}$$
Cohesion	Westerly granite (Bauer and Johnson 1979); Granite X (Xu et al. 2014), Strathbogie granite (Kumari et al. 2017b); Westerly granite 1 (Dwivedi et al. 2008); Westerly granite 2 (Dwivedi et al. 2008); Charcoal granodrite (Friedman et al. 1979); Granite T (Tian et al. 2016). $$f_{c/c_0} = 0.1699(6.9845 - e^{0.001876T}), 0°C < T \le 1000°C$$
Young's modulus	Strathbogie granite (Shao et al. 2015); Remiremont granite, Senones granite, Salisbury granite, British granite, Indian granite (Dwivedi et al. 2008); Granite Y (Yang et al. 2017); Granite C (Chen et al. 2017b); Granite X (Xu et al. 2014). $$f_{E/E_0} = \begin{cases} 1.2665/(1+e^{-1.430+0.0034T}), & 0°C < T \le 600°C \\ 1/(-109.953+17.542\ln(T)), & 600°C < T \le 1250°C \end{cases}$$
Poisson's ratio	Granite Y (Yang et al. 2017); Granite T (Tian et al. 2016); Strathbogie granite (Kumari et al. 2017b). $$f_{v/v_0} = \begin{cases} -7 \times 10^{-4}T + 1.0052, & 0°C \le T \le 600°C \\ 2.240/(1+e^{13.11-0.020T}), & 600°C < T \le 800°C \end{cases}$$
Thermal expansion coefficient	Shield granite α (Ramana and Sarma 1980); Granite α H (Heuze 1983); Quartz β (Van der Molen 1981); Granite α C (Chayé d'Albissin and Sirieys 1989); Westerly granite β (Cooper and Simmons 1977); Quartz-a-axis α, Quartz-c-axis α (Polyakova 2014); Stripa granite β (Dwivedi et al. 2008). $$f_{\alpha_t/\alpha_{t0}} = \begin{cases} (0.8383 - 0.00142T)^{(-1/1.7085)}, & 0°C \le T \le 573°C \\ (-5.4160 + 0.0095T)^{(-1/1.5719)}, & 573°C < T \le 625°C \\ f_{T=625}, & 625 < T \le 800°C \end{cases}$$
Specific heat	Salisbury granite, USSR granite (Dwivedi et al. 2008); Charcoal gray granite, Rockville granite, Jasper quartzite (Lindroth and Krawza 1971). $$f_{C_v/C_{v0}} = \begin{cases} 0.957 + 6.59 \times 10^{-4}T, & 0°C \le T \le 575°C \\ 1.173 + 1.238 \times 10^{-4}T, & 573°C \le T \le 1000°C \end{cases}$$
Thermal conductivity	Granite H (Hartlieb et al. 2016); Granite R (Romine et al. 2012); Granite W (Wen et al. 2015); Granite Z (Žák et al. 2006); Empirical law (Heuze 1983). $$f_{k/k_0} = -5.8126 + 6.8485 \times 0.9995^T + 0.002172T, 0°C \le T \le 1200°C$$

(a) Normalized tensile strength

(b) Normalized cohesion

(c) Normalized Young's modulus

(d) Normalized Poisson's ratio
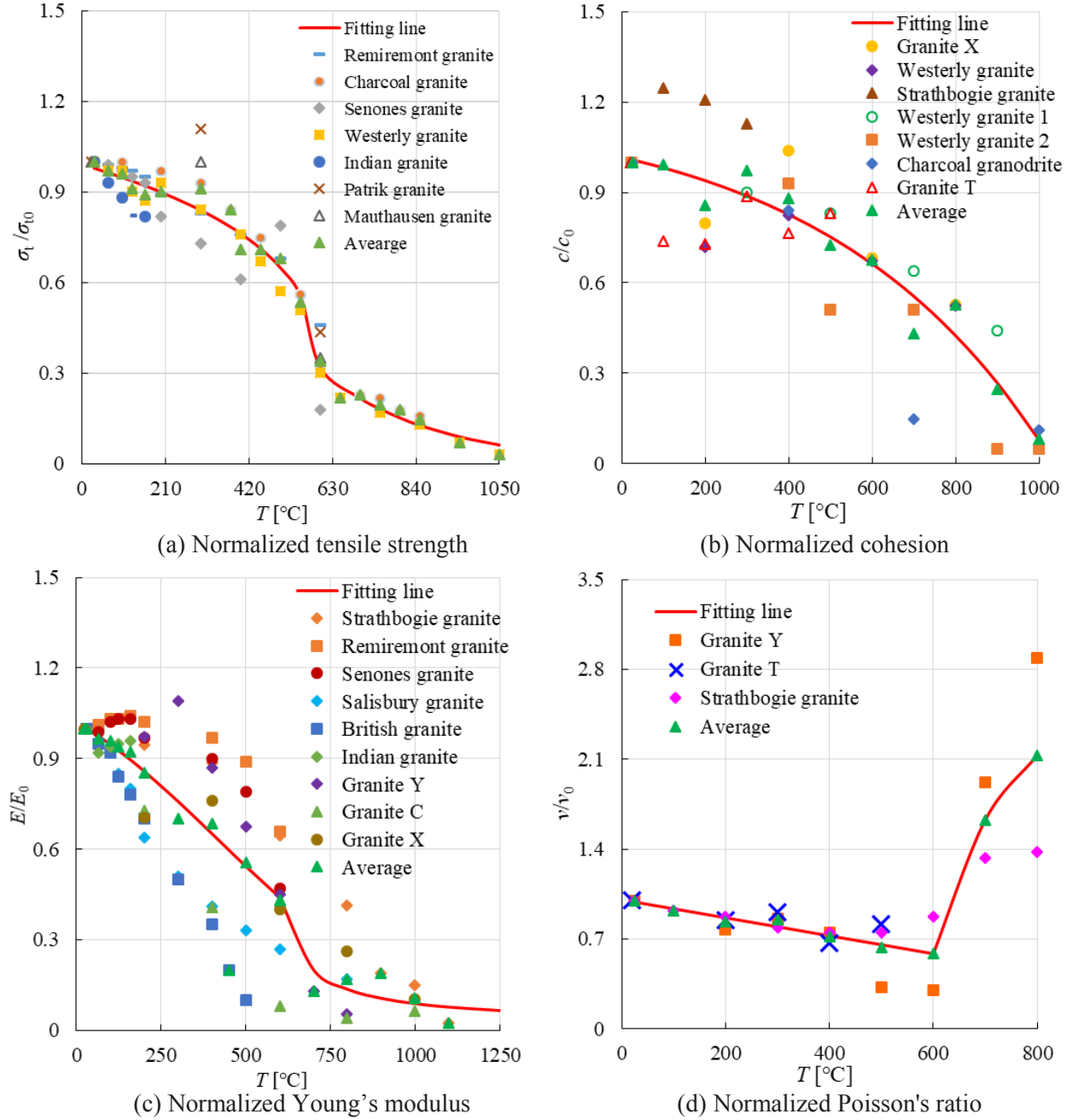
Figure 2-3 Normalized mechanical properties vs. temperature

Therefore, a significant change in material parameters is usually caused by the α-β transition of quartz at 573 °C. The quartz phase transition is a displacive transition, and only a distortion of the structure without breakage of bonds (see Figure 2-5) (Xie et al. 2012; Dong et al. 2015). Expansion through the high-low transformation (i.e. α-β transition) is reversible and continuous. The maximum linear coefficients of expansion at the transformation can be up to $400 \pm 50 \times 10^{-6}$/°C

between 572 and 574 °C (Ackermann and Sorrell 1974). As a result, the α-β transition will strongly influence the thermal cracking behaviour of granite at elevated temperatures.
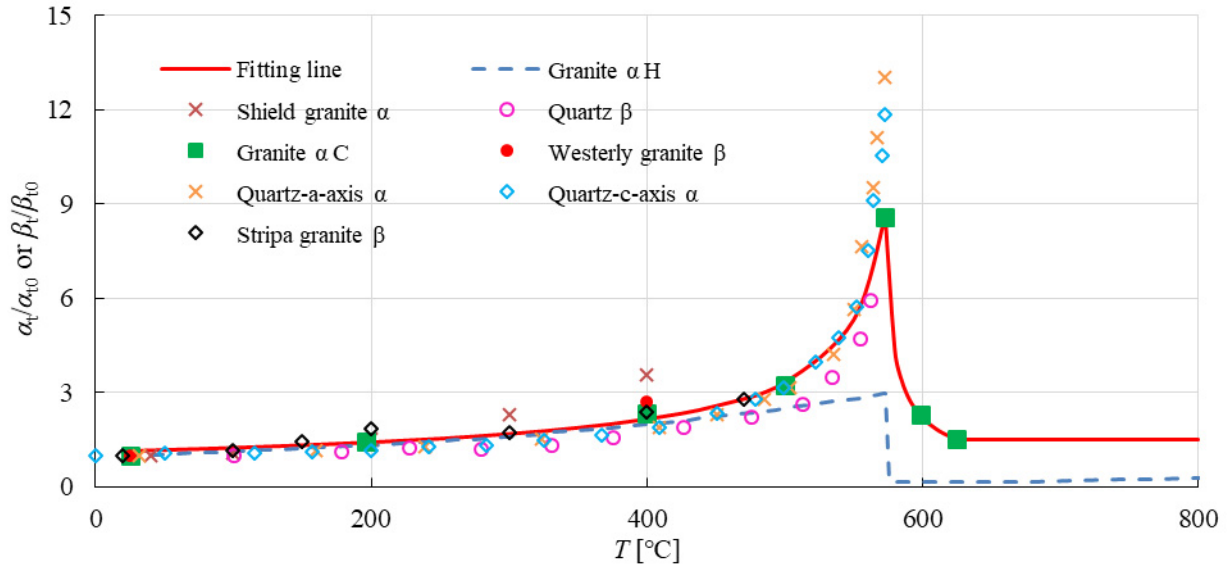
(a) Normalized thermal expansion coefficient
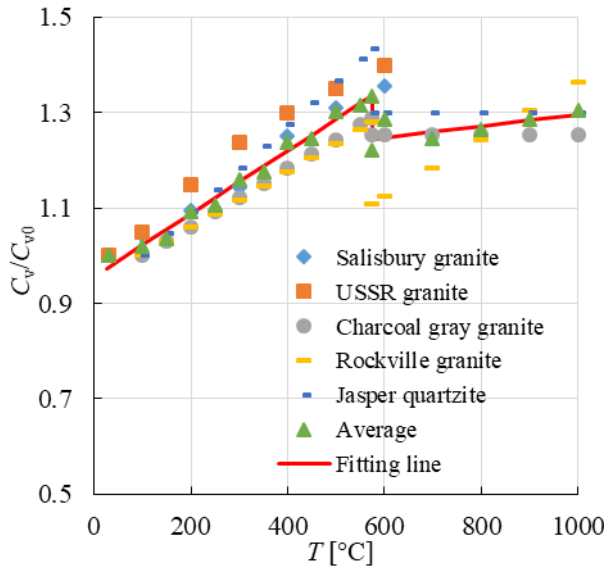
(b) Normalized specific heat
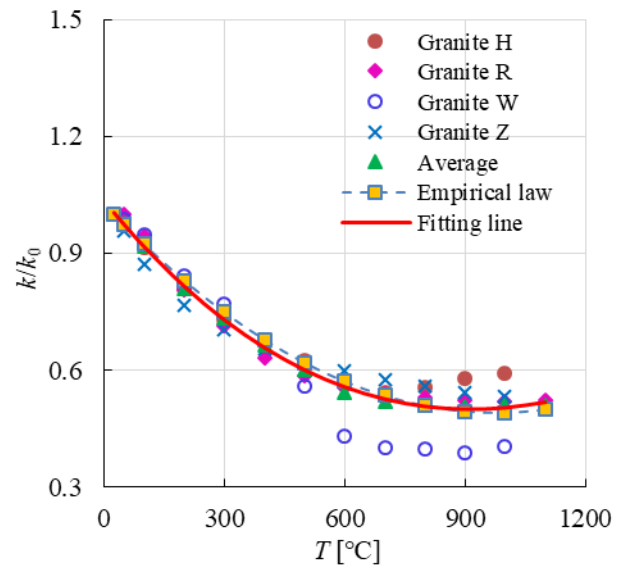
(c) Normalized thermal conductivity

Figure 2-4 Normalized thermal properties vs. temperature

Some scholars attribute the property (especially strength) change to the large amounts of newly developed microcracks induced by the α-β quartz transition. Glover et al. (1995) reported about acoustic-emission (AE) experiments that monitor the process of thermal cracking during heating. They proposed that the peak in AE hit rate represents acoustic emissions that occur as a result of

the gross microcracking induced by the quartz phase transition. Consequently, the generation of a large number of new cracks has a significant effect on other properties of the granite. Chen et al. (2017) used AE monitoring, ultrasonic velocity measurements and scanning electron microscope (SEM) observations to assess the thermal effect on physical and mechanical properties of granite. They think the pronounced weakening at 573 °C is due to newly developed intragranular cracks caused by the phase transition of quartz. Chaki et al. (2008) conducted laboratory measurements to investigate the influence of thermal damage on physical properties of granitic rocks. They also believe that the α-β phase transition is an important factor to induce microcracks. Inserra et al. (2013) deem that the marked structural changes in heated granite are due to drastic changes in the microstructure connected with the generation of new cracks at elevated temperatures, especially at the α-β transition temperature of quartz at 573 °C. Yang et al. (2017) used X-ray micro CT and investigated the thermal damage of granite after high temperature treatments. They believe the transition results in a large increase in volume of quartz, and therefore a substantial amount of thermal microcracking occurs.

(a) α-quartz   (b) β-quartz
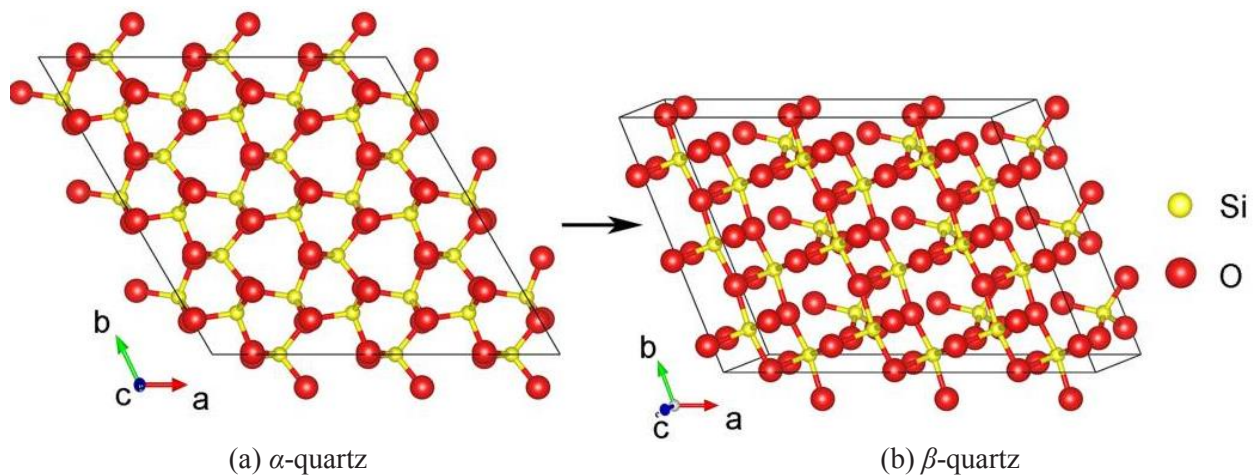
Figure 2-5 Structural changes of quartz (Dong et al. 2015)

However, other studies reveal that quartz expansion might predominantly be caused by the extension of already existing microcracks. Which means that the majority of microcracks are induced before the quartz phase transition takes place, and that these cracks will be only widened during the quartz transition. Johnson et al. (1978) investigated the longitudinal wave velocity and porosity of Westerly granite, and found that - above 573 °C - the porosity increase is associated primarily with microcrack-gap widening rather than new microcrack formation. Lin (2002)

measured microcrack density by using optical microscopes. He found that the crack density begins to increase gradually after crack generation, but no abrupt change happens up to 600 °C. This means the quartz transition at 573 °C does not have an effect on accelerating the generation of new cracks. However, the crack width and width increment experience a rapid increase from 500 to 600 °C, indicating a crack expansion caused by the quartz transition at 573 °C. Bauer and Johnson (1979) measured the variation of longitudinal wave velocity and crack density of Westerly and Charcoal granites with maximum temperature attained during a thermal cycle. Although the velocities decreased rapidly between 500 °C and 600 °C with the greatest rate at 573 °C, no rapid increase of crack density happens in both, Westerly and Charcoal granite. This means the quartz transition does not have an obvious contribution to the crack density evolution (i.e. new crack generation), but can influence the opening of pre-existing cracks. This is confirmed by a deeper going SEM study of Westerly granite by Bauer and Johnson (1979). In their study, specimens were sequentially heated to 200 °C, 450 °C, and 750 °C to observe microcrack development and widening. Cracks that had existed at 200 °C have widened at 450 °C with aperture increase by a factor of two. Heating to 750 °C results primarily in widening of cracks existing at 450 °C, with aperture widening further by a factor of two to six. In addition, a few new cracks are observed. Besides the authors mentioned above, Homand-Etienne and Houpert (1989) used SEM technique to observe thermal cracking in a temperature range between 20 to 600 °C for two different types of granite. SEM observations showed that during the thermal treatment, the crack width enlargement is intensified with ongoing temperature increase. Especially between 500 °C and 600 °C, such cracks manifest that openings could be more than tripled. Nasseri et al. (2007) also found that at lower temperatures up to 450 °C, the widths measured in intragranular (IG) and grain boundary (GB) cracks remained more or less constant. However, at higher temperature, especially after 600 °C, an exponential increase of crack width for IG and GB microcracks was observed.

The conflict between the above-mentioned explanations is based on the used techniques. For example, the signals of AE monitoring can be influenced by both, number and width of cracks. It is practically impossible to discriminate their influences. As for microscopic observations, the accuracy is limited by the resolution of the device. This problem is also discussed in this study.

2.3 Numerical simulation of thermal induced cracking of granite

Compared to the numerous documented lab tests of heated granite, numerical simulations of brittle rocks at very high temperatures (e.g. above 500 °C) are quite marginal. Jiao et al. (2015) proposed a 2D discontinuum model for simulating thermal cracking of brittle rocks within the framework of the Discontinuous Deformation Analysis (DDA) method (see Figure 2-6a), but the material deformation rate was assumed to be zero in the proposed model, i.e., the influence of material deformation on temperature was not considered. Shao et al. (2015) built a 2D Finite Element (FE) model for compression tests carried out on granite specimens at elevated temperatures (see Figure 2-6b). One of the drawbacks of this model is that, uniform temperature across the entire granite is assumed. Therefore, thermal cracking cannot be simulated in a correct manner. Zhao (2016) elucidated the mechanisms responsible for temperature-dependent mechanical properties of granite using a particle-based approach (see Figure 2-6c), indicating that the strength reduction mainly results from the increasing thermal stresses and the generation of tensile microcracks. The boundary temperature was limited to 400 °C because the model could not simulate some significant changes induced by the α-β quartz phase transition, and also only monotonous changes of the mechanical behavior were obtained because no temperature-dependent parameters were assigned in this model. Xu et al. (2017) proposed a two-dimensional thermo-mechanical model based on Weibull distributions for the parameters to describe the time-dependent brittle deformation (brittle creep) of granite considering confining pressures and temperature-independent properties for different constant temperatures (maximum temperature was set to only 90 °C) (see Figure 2-6d).

Previous simulations have usually applied specific loading, constant properties and low or fixed temperatures. However, for some cases like buildings or sculptures exposed to fire, unconfined boundary conditions are realistic with different heating rates, extremely high temperatures (e.g. 800 °C) and significant changes in properties. Comprehensive models for this issue are still missing. Continuum based methods are quite attractive, because they can reproduce different failure phenomena, from brittle to ductile including softening by averaging the effect of crack evolution and coalescence (Wang and Konietzky 2019). Therefore, in this study the Finite Difference (FD) continuum code FLAC^{3D} (Itasca 2019) is used with the aim to develop a new numerical scheme to simulate the thermal induced damage of granite at high temperatures.

(a) Fracture pattern   (b) Plastic strain distribution

(c) Microcrack distribution   (d) Strength distribution
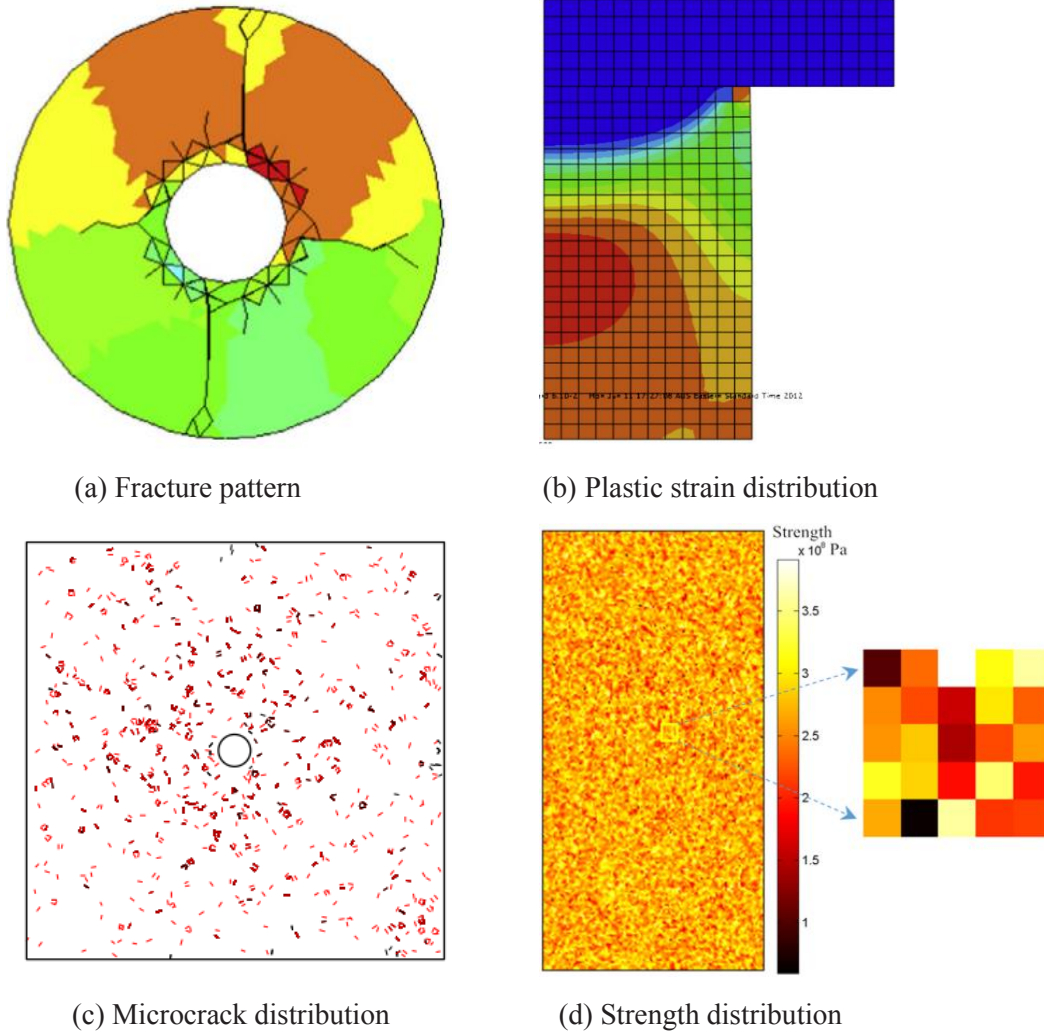
Figure 2-6 Numerical methods used in previous thermo-mechanical studies: (a) DDA method (Jiao et al. 2015), (b) FE model (Shao et al. 2015), (c) particle based approach (Zhao 2016), (d) heterogeneous continuum based model (Xu et al. 2017)

Another important issue in numerical simulation is how to characterize the heterogeneous nature of granite. Granite is a medium to coarse grained igneous rock that is rich in quartz and feldspar. The percentage of different minerals varies in different granites. There are two popular approaches to reproduce the heterogeneous nature of granite. One of them is that the spatial distribution of mineral grains is modelled in a direct way based on the real mineral composition obtained from some techniques including X-ray diffraction and digital images of a real piece of rock. Chen and Konietzky (2014) simulated the time-dependent damage process of Lac du Bonnet granite with the discrete element method considering the microstructure including different mineral components and grain size. They found that the proposed modelling strategy is able to reproduce the

macroscopic short- and long-term behaviour of brittle rocks. By using integrated microscopic observations, image analysis and numerical modelling, Wang (2015) presented a simulation method characterizing heterogeneous rock breakage behaviour according to its actual microstructure. The results demonstrated that minerals and their distributions play a major role in the breakage process. Tan et al. (2016) set up a numerical discrete element model based on digital image processing (DIP) data. They documented the influence of heterogeneities and microstructure of granitic rock on the fracture pattern. Mahabadi et al. (2014) presented a thin section analysis to detect microcracks and to investigate the influence of heterogeneity on the failure behaviour and the mechanical response of crystalline rocks. They concluded that heterogeneity and microcracks should be considered to accurately predict tensile strength and failure behaviour. Yang et al. (2018) generated numerical particle-based models using results of X-ray diffraction to study the failure behaviour of pre-holed granite specimens after elevated temperature treatment. His simulation results reproduced the experimental results to some extent. Besides the authors mentioned above, many other researchers (e.g. Chen et al. 2004; Liu et al. 2004) also used this mineral-based method to study the failure behaviour of rocks considering its advantage in reproducing the heterogeneous characteristics.

However, the mineral based method has some obvious drawbacks: (i) it heavily depends on detailed micro-observations and DIP; (ii) reconstruction of three-dimensional bodies of heterogeneous materials is restricted; (iii) only one specific configuration is duplicated; (iv) models at the grain size level are restricted in size due to the restricted computational power. To avoid these difficulties, statistical methods like the Weibull distribution has been considered to characterize the heterogeneity (Vales and Rezakhanlou 1999; Tham et al. 2001; Cao et al. 2004). The problem which has not been mentioned in previous studies is that, the statistical distribution method lacks the factual mineral composition of the rocks. Therefore, a new method to characterize the heterogeneity of rocks is needed to improve the accuracy and rationality of such simulations.

3 Thermo-mechanical properties of Eibenstock granite at elevated temperature

In this Chapter, the thermo-mechanical behaviour of Eibenstock granite under the temperature of 400 °C and 800 °C was studied applying heating rates of 5 °C/min, 200 °C/min, 300 °C/min, and according to ISO 834 standard fire curve. A supersonic frequency induction heating system was used to conduct the required heating scenarios and to perform uniaxial compression tests under the desired temperatures. A threshold modulus E_c obtained from dividing peak axial stress by the peak axial strain is defined to characterize the stiffness of the sample at various temperatures. Both, tangent Young's modulus and threshold modulus are greatly influenced by maximum temperature, while the influence of heating rate is relatively small. The maximum temperature has the dominant impact on the uniaxial strength of granite samples, while the influence of heating rates is again negligible. The peak axial strain increases obviously with rising temperature. It first increases at 200 °C/min heating rate and then reduces slightly in scenarios with heating rates of 300 °C/min or heating according to ISO 834. The observed failure modes after uniaxial compression tests are influenced by peak temperature and heating rates. The granite specimen can be thermally crushed into blocks, fragments or powder. The deduced friction angle for various heating scenarios is more or less unchanged, while the cohesion shows a strong temperature-dependent characteristic.

Thermal properties including specific heat, thermal conductivity, thermal diffusivity, and linear thermal expansion coefficient are measured at elevated temperatures with slow heating rate of 5 °C/min. All thermal properties are temperature-dependent, especially the expansion coefficient which shows a steep increase around 573 °C as well as at 870°C.

3.1 Influence of various heating rates on granite properties

The general temperature rise during a building fire is described in ISO 834 (see Figure 3-1), which was developed based on wood fuel burning furnaces, and was later modified slightly to consider a faster temperature rise for the first few minutes of burning to represent gas fired furnace temperatures (Szumiga 2015; Rodrigues and Laím 2017). The ISO 834 standard fire time-temperature curve can be described by the equation $T = T_0 + 345 \cdot log(8t+1)$, where T_0 is the room temperature, T is the actual fire temperature in °C, and t is time in minutes. This results in an average temperature rising rate in the first minute of about 330 °C/min, followed by a gradual

decrease to only 5 °C/min after 30 minutes. The temperature rising variation during a fire makes it necessary to investigate the granite behaviour at different heating rates and temperatures. However, almost all the existing data about granite heating are obtained at low to moderate heating rates (usually 1 °C/min to 10 °C/min) (Cooper and Simmons 1977; Ramana and Sarma 1980; Wang et al. 1989; Kumari et al. 2017b; Griffiths et al. 2018).
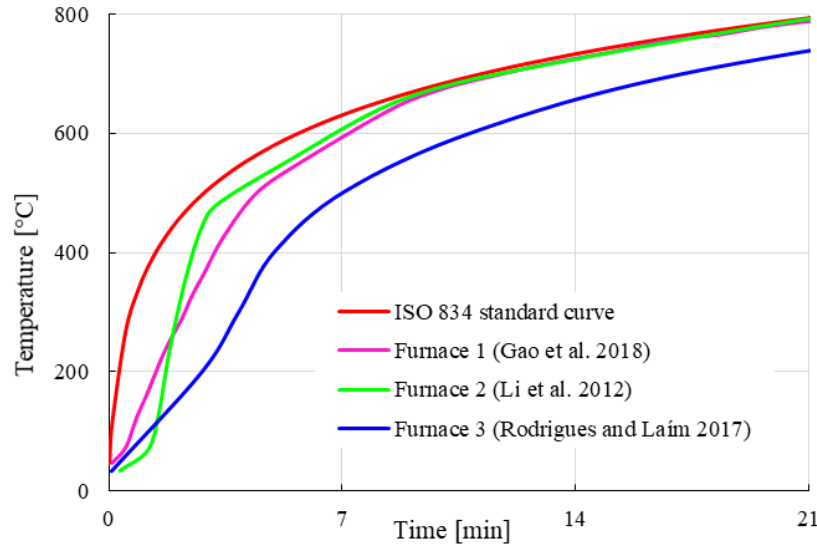
Figure 3-1 Heating curves of furnaces and according to ISO 834 (from $T_0 = 25$ °C to $T = 800$ °C)

Compared with the large number of researches on the influence of constant heating rates on granite properties after heat treatment, studies of the influence of variable heating rates on granite properties determined at elevated temperature are also marginal. Ramana and Sarma (1980) studied the thermal expansion of granite samples at two different rates (2 and 5 °C/min). Results show that the linear coefficient of thermal expansion deduced from a rate of 5 °C/min is higher than that obtained at 2 °C/min. Chen et al. (2017a) investigated the thermal damage of Beishan granite subjected to temperatures from 100 °C to 800 °C at different heating rates (ranging from 1 to 15 °C/min). The heating rate has an obvious impact on the thermal induced cracks. Dwivedi et al. (2008) performed uniaxial compression tests on granite continuously heated to 65, 100, 125 and 160 °C, and found that the compressive strength is higher than those measured at room temperature. Shao et al. (2015) carried out uniaxial compression strength (UCS) tests while samples were kept at desired temperatures of 800, 900 and 1100 °C. Stress-strain curves show that increasing

temperature influences the failure mechanisms of Strathbogie granite and ductility becomes dominating at temperatures above 800 °C.

To study the fire effects in laboratories, the use of ovens to simulate the heating generated by fire is the most common way. Oven heating has the following advantages: availability, automatic functions and high degree of standardization and replication (Gomez-Heras et al. 2009). The wealth of published results obtained with this technique provides a sound database for comparison with new results. However, oven temperatures usually exhibit a delay in the first few minutes in relation to the ISO 834 standard fire time-temperature curve (see Figure 3-1). High heating rates cannot be reproduced by an electric oven. This effect becomes even worse for larger ovens with high thermal inertia (Li et al. 2012; Rodrigues and Laím 2017; Gao et al. 2018).

Therefore, to investigate the change of granite properties during a fire, two major challenges have to be met: (1) reaching high speed heating with variable rates and reproduction of ISO 834 fire time-temperature curve of thermal loading and (2) determination of granite properties in the stage of high temperatures (i.e. mechanical testing at constant high temperature). Besides the slow heating methods, this chapter documents how these questions about high speed heating were solved and which corresponding results were obtained.

3.1.1 Sample description and testing system

The investigated granite (see Figure 3-2) is from the Eibenstock Massiv in Saxony, Germany. Figure 3-3 shows the mineral composition of Eibenstock granite (EG). The grains have irregular shapes like fan-shaped, strip-shaped, xenomorphic etc. The grain size also varies significantly. Orthoclase accounts for a large share of mineral composition with a proportion of 40 %. The minerals usually have a grain size between 1 mm to 4 mm, though some grains show a maximum and minimum size of 7 mm and 0.04 mm, respectively. Plagioclase accounts for 10 % of the minerals and usually concentrates in individual areas compared to other detectable minerals. Quartz has a mineral proportion of 44 %, which is very close to the value for orthoclase. The maximum quartz grain size ranges from 1.5 mm to 4.8 mm. Siderophyllite grains are usually scaly and xenomorphic, and account for 6 % of the mineral composition. The largest mineral grains reach a diameter of 3.5 mm, whereas the smallest have a size of 0.02 mm. Besides the minerals mentioned

above, accessory minerals account for less than 1 %. Cylindrical samples are prepared for high speed heating tests. The cylindrical samples have a nominal diameter of 50 mm and a length of 100 mm. Both, top and bottom of the samples were grinded and polished in order to make end-faces smooth and parallel. All the samples were dried at room temperature before testing.

Figure 3-2 Cylindrical sample of Eibenstock granite at room temperature
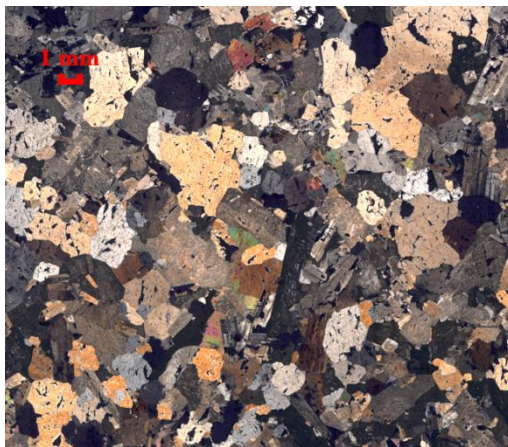
| (a) Microscopy image (thin section) | (b) Dominant mineral composition |
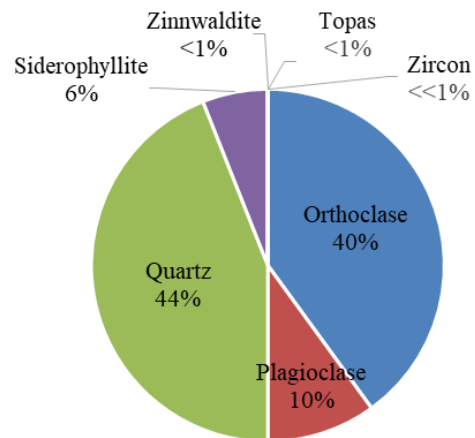
Figure 3-3 Mineral composition of Eibenstock granite

Since an ordinary heating oven cannot reach the required high heating rates, we used a supersonic frequency induction heating equipment as heating device (Figure 3-4). This device was designed by scientists at Wuhan University of Science and Technology (WUST) in China. The induction coil, in which cooling water flows, does not produce heat directly. It actuates the high-strength graphite surrounding the granite sample to generate intense heat flux. The heating system adopts

the Yudian artificial intelligence temperature controller (AI-5097) for temperature adjustment. The AI controller has an accuracy of ± 1 °C. The linear actuator, which controls the movement of the thermocouple, guarantees the contact between the sample surface and the thermocouple. The outer and inner diameters of the cylindrical graphite are 75 mm and 60 mm, respectively. The height of the graphite cover is about 66 mm, which leaves enough spaces for the deformation of granite during heating and compression. The diameter of the hole (about 8 mm) on graphite is slightly larger than that of the thermocouple. It allows to measure the temperature at the surface of the sample. Calcium silicate cotton is used as thermal insulation. Since the metal loading plates of the mechanical machine cannot be exposed to high temperatures, we used grinded mullite cubes as spacer blocks for load transmission. Mullite has excellent high temperature properties with improved thermal shock and stress resistance. The Young's modulus of mullite is about 220 GPa at room temperature and the variation up to 1500 °C will usually be unmeasurably small and negligible in practice (Hamidouche et al. 2003; Pabst et al. 2013). It has a higher strength and stiffness than Eibenstock granite. Uniaxial tests were performed once thermal treatment was done. The specimens were compressed by the universal testing machine with electromechanical system with a loading rate of 0.5 mm/min. Axial load and displacement were measured and recorded by the testing machine until final failure.
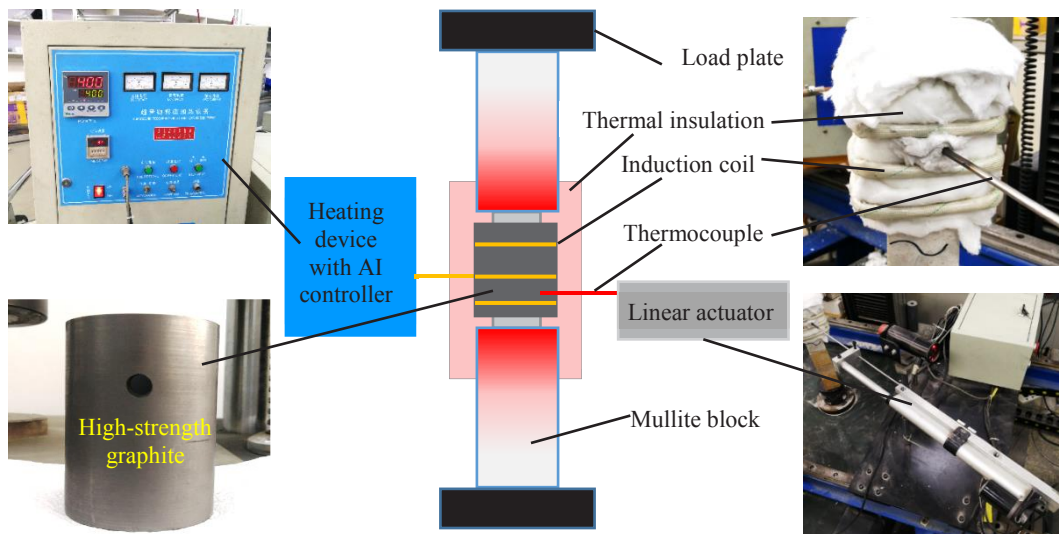
Figure 3-4 Experimental system for realizing high speed heating rates

Figure 3-5 shows the measured temperature values for heating scenerios with a target temperature of 800 °C and a holding time of 1 hour at target temperature. For constant heating rates (5 °C/min, 200 °C/min, 300 °C/min), the heating device can well reproduce the desired curves. In case of the standard fire curve with variable heating rates the measured temperature is in good agreement with the temperature-time curve according to ISO 834. However, since the heating rates of ISO 834 curve vary significantly within a short time, the used equipment proved to be not sensitive enough to adjust the temperature accurately during the transition from high speed heating to slow speed heating. As a result, the temperature in the test is slightly higher than the standard value when heating rates are decreasing until approaching the target temperature (see Figure 3-5). Only the termperature-time curves of the 800 °C scenarios are presented in Figure 3-5. The 400 °C heating scenerios are almost the same as the 800 °C scenarios, but they are less challenging and more easily to achieve by the heating device.

The heating system is characterized by two limitations. One of them is that the maximum temperature is usually 20 to 50 °C higher than the designed value (see Figure 3-5). This overshoot is caused by the heat flux induced at the time before the target temperature is reached, especially when heating rate is high (e.g. 200 °C/min and 300 °C/min). The second one is that the system records only temperatures above 75 °C, data below this temperature are not collected. But this is not a serious problem since our target temperatures are well above this lower limit for data acquisition.
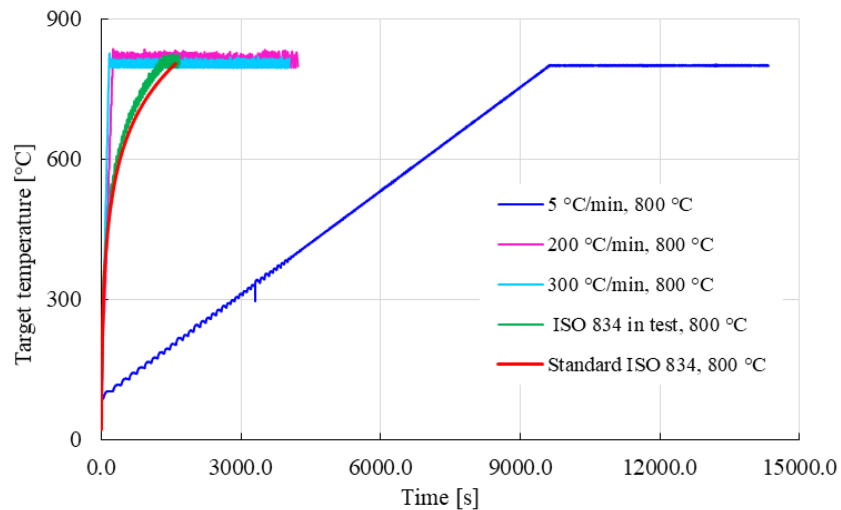
Figure 3-5 Temperature curves for different heating scenarios by using the supersonic frequency induction heating.

19

3.1.2 Test method

The tests were subdivided into three consecutive stages. A thermal treatment phase including stage 1 and 2 was followed by a mechanical loading stage, in which the specimens were exposed to thermo-mechanical-coupled scenarios (see Table 3-1): (1) Heating stage: temperature increase up to target value; (2) Dwelling stage: holding temperature constant at target value for 1 h; (3) Mechanical loading stage: uniaxial compression test while specimen is still exposed to desired temperature.

Table 3-1 Sample dimensions and heating scenarios

No.	Samples	Diameter [mm]	Length [mm]	Density [g/cm³]	Heating rate	Target temperature + holding time	Compression at desired temperature
1	C-1-1*	50.37	100.71	2.59	400 °C/min	400 °C+1h	Yes
2	C-1-2	50.31	100.88	2.59	5 °C/min	400 °C+1h	Yes
3	C-1-4	50.36	100.70	2.59	5 °C/min	800 °C+1h	Yes
4	C-1-5	50.32	100.97	2.59	5 °C/min	800 °C+1h	Yes
5	C-1-6	50.35	100.79	2.58	5 °C/min	400 °C+1h	Yes
6	C-2-1	50.33	100.82	2.58	300 °C/min	400 °C+1h	Yes
7	C-2-2	50.31	101.27	2.59	300 °C/min	400 °C+1h	Yes
8	C-2-4	50.33	100.97	2.59	300 °C/min	800 °C+1h	Yes
9	C-2-5	50.33	101.10	2.59	300 °C/min	800 °C+1h	Yes
10	C-3-1	50.33	101.37	2.59	200 °C/min	400 °C+1h	Yes
11	C-3-2	50.33	101.38	2.59	200 °C/min	400 °C+1h	Yes
12	C-3-4	50.36	101.12	2.58	200 °C/min	800 °C+1h	Yes
13	C-3-5	50.33	101.24	2.58	200 °C/min	800 °C+1h	Yes
14	C-4-1	50.33	100.40	2.59	ISO 834	400 °C	Yes
15	C-4-2	50.33	101.00	2.58	ISO 834	400 °C	Yes
16	C-4-4	50.32	100.58	2.59	ISO 834	800 °C	Yes
17	C-4-5	50.31	101.31	2.58	ISO 834	800 °C	Yes
18	C-4-6	50.32	101.08	2.58	ISO 834	800 °C	Yes

* Since the sample was damaged by the trial rate of 400 °C/min, we did not analyze it further

For some selected specimens, stage 2 was skipped. They were tested without dwelling (holding) time immediately after reaching target temperature (see Table 3-1). Different heating scenarios are performed to test the influence of heating rates on granite properties considering different desired final temperatures. Specimens were heated with constant rates, i.e. 5 °C/min, 200 °C/min and 300 °C/min, are then kept in the heating device for one hour at target temperature to ensure uniformity in temperature distribution across the specimen. The test results of granites with 5 °C/min heating rate can serve as reference for samples with higher heating rate. For specimens

heated according to ISO 834 standard fire temperature-time curve, no holding time is set to investigate the sample behavior during a fire. Uniaxial tests were performed once thermal treatment was done. The specimens were compressed with a rate of 0.5 mm/min. Axial load and displacement were measured and recorded by the testing machine until final failure. During the loading process, temperatures were kept constant at target values for samples without cooling stage (see Table 3-1).

3.1.3 Uniaxial compression tests of granite at desired temperature

Figure 3-6 shows the results of uniaxial compression tests of granite specimens at different temperatures whereby the samples experienced different heating rates before. The properties of Eibenstock granite at room temperature (25 °C) have been determined in the Rockmechanical Laboratory of the Geotechnical Institute, TU Bergakademie Freiberg, Germany. The stress-strain curves of the three samples tested at room temperature (Ref. 1, Ref. 2, and Ref. 3) are documented in Figure 3-6 as well. It is obvious that both, maximum temperature and heating rate have a significant influence on granite properties. In order to compensate the deformation behavior of the loading system (stiffness of the loading frame) as well as the deformation of single mullite cubes and the interfaces between connected cubes, calibration tests have been conducted. By determining the load dependent deformation of the system comprising of the testing machine with realistic test setup including mullite cubes but without inserted rock specimen, the measured data in the tests can be corrected for inherent deformation portions. Following this procedure, measured and calculated quantities such as failure strain and Young's modulus are very reliable. Comparative analysis and conclusions are valid in any case, since all thermo-mechanical properties are obtained using the same loading conditions. A qualitative analysis of the influence of maximum temperature and heating rates on elastic modulus, uniaxial compressive strength and axial strain of granite, is documented in the following sections.

3.1.3.1 Young's modulus

The axial stress-strain curves of granite specimens after heat treatment show noticeable nonlinearity and yielding phase before reaching peak strength (see Figure 3-6). To characterize the stiffness of the sample, a threshold modulus E_c obtained from dividing peak axial stress σ_c by peak

axial strain ε_c is defined. The commonly used tangent Young's modulus E_t, which is measured at a stress level equal to 50% of the uniaxial compressive strength (ISRM 1979), is also calculated.
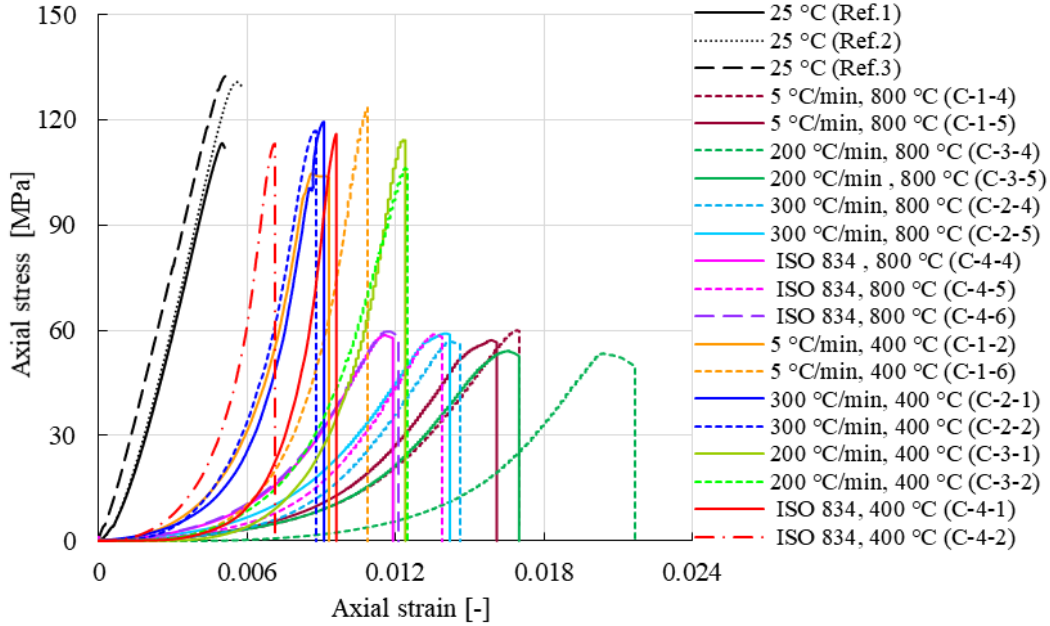
Figure 3-6 Stress-strain curves of Eibenstock granite for different target temperatures and different heating rates

Figure 3-7 shows Young's modulus of granite at different temperatures considering various heating rates. The tangent Young's modulus E_t (200 °C/min heating rate) shows a continuous decrease at elevated temperatures (see Figure 3-7b). However, slight increase in stiffness is observed at 400 °C with heating rates of 300 °C/min (see Figure 3-7c) and according to ISO 834 (see Figure 3-7d). At 800 °C, reached after various heating rates, E_t reduces to a value of about 10 % - 30 % of the value at room temperature (25 °C).

Temperature treatment at all levels exerts a significant influence on the reduction of threshold modulus E_c. This indicates that higher temperatures lead to increased axial deformation of granite samples during the whole compression process until final failure. The biggest difference between E_t and E_c is measured for sample C-4-1 at 400 °C applying ISO 834 heating curve, showing a difference of 27.59 GPa (see Figure 3-7d). This may be caused by internal structural changes due to continuous change in heating rates according to the ISO 834 curve, which varies from 342 °C/min in the first minute to about 67 °C/min in the second one. This significant change alters crack initiation in specimens compared with samples which experience only constant heating rates.

Another possible reason could be that there is no dwelling stage of 1 hour according to ISO 834 heating scenario. However, the differences between E_t and E_c at room temperature and 800 °C are very similar for all heating scenarios (including constant heating with dwelling stage and ISO 834 case without dwelling stage), indicating that the big difference of 27.59 GPa is not likely to be attributed to the dwelling stage. Considering the significant difference in the value of tangent modulus E_t and threshold modulus E_c, using tangent Young's modulus at high temperatures might cause problems in engineering practice. It can overestimate the stiffness of the material at higher temperatures. The threshold modulus E_c, which can better quantify the stiffness of granite at high temperatures during the whole process until final failure, seems to be more practical.
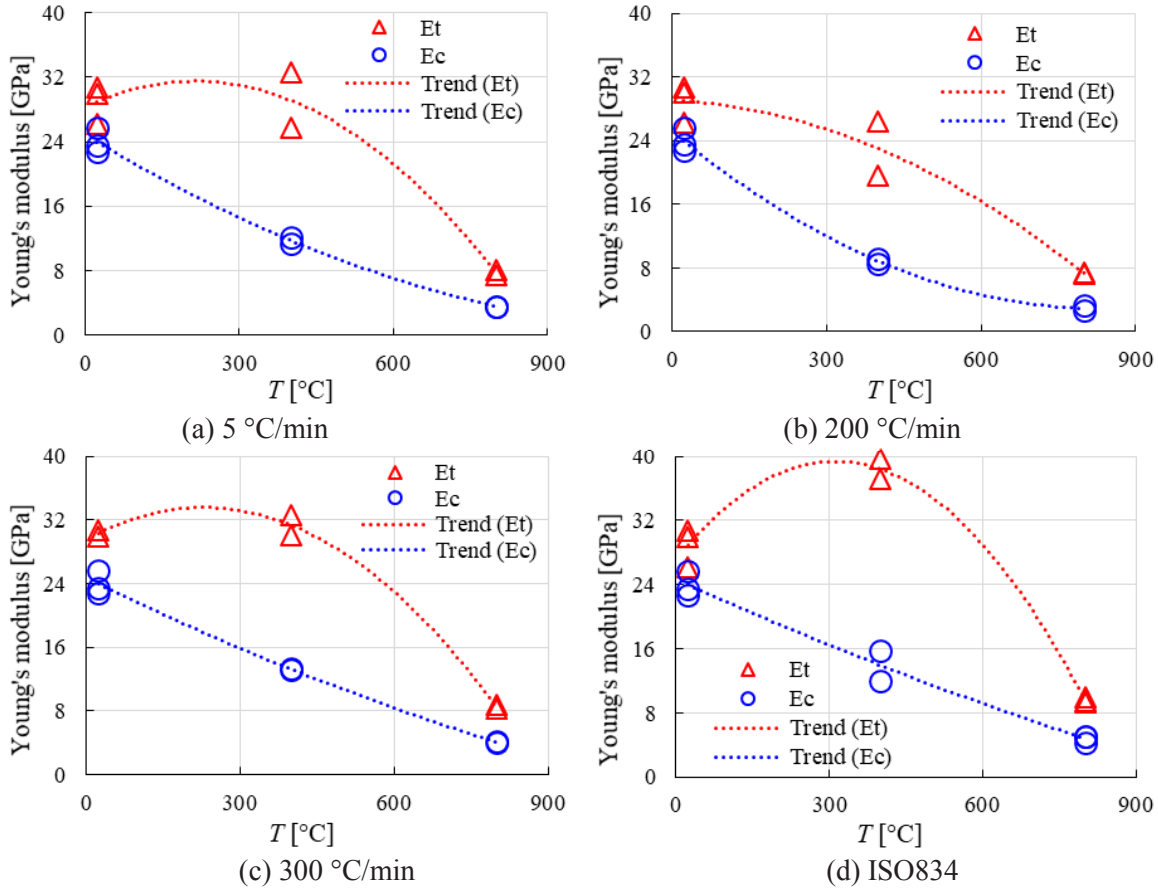
Figure 3-7 Variations of Young's modulus E_t and threshold modulus E_c at different temperatures considering various heating rates

The influence of heating rate on Young's modulus is not as strong as that of maximum temperature, especially for tangent modulus E_t (see Figure 3-8). Another noticeable phenomenon is that heating rate of 200 °C/min shows a negative effect on Young's modulus, while 300 °C/min enhance the

modulus slightly. A preliminary conclusion could be that Young's modulus will decrease slightly with increasing heating rate until about 200 °C/min. Heating rates higher than app. 200 °C/min slightly increase the stiffness of granite. Compared with the significant influence of temperature, the effect of heating rate is negligible. To obtain more reliable conclusions about the influence of heating rates on Young's modulus, more tests with a series of elevated heating rates are needed.

(a) Target temperature 400 °C (b) Target temperature 800 °C
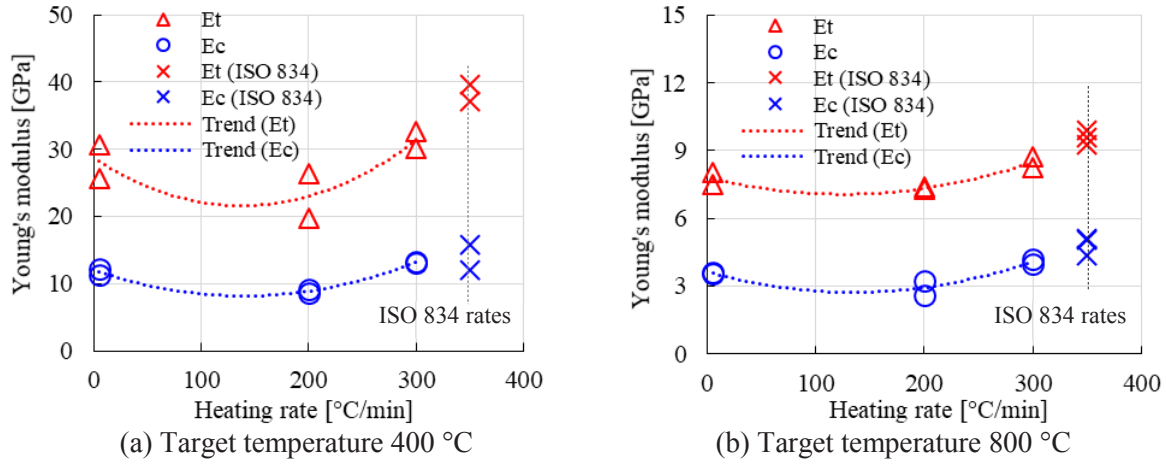
Figure 3-8 Young's modulus determined at desired temperature for different heating rates

Since granites have different property values after different heating scenarios, normalized values are used to detect the tendencies of temperature or heating-rate dependent properties. Normalized properties of various heating scenarios related the values at room temperature are shown in Figure 3-9 and Figure 3-10. The threshold modulus E_c is more temperature-dependent than the tangent modulus E_t, since E_t shows a big dispersion at 400 °C (see Figure 3-9a). The general trend is that the tangent Young's modulus E_t decreases significantly after 400 °C while the threshold modulus E_c shows a continuous decrease with rising temperature.

Figure 3-10 shows normalized Young's modulus versus heating rate after applying different heating scenarios. Tangent Young's modulus E_t of specimens heated up with 200 °C/min shows a slight decrease of 10 % compared to a heating rate of 5 °C/min (Figure 3-10a). When the heating rate rises to 300 °C/min, E_t experiences an increase of about 6% and 16% compared to 5 °C/min and 200 °C/min, respectively. The threshold modulus E_c shows a similar trend. Compared with the rate of 5 °C/min, a reduction of 7% and an increase of 5% in E_c can be observed for 200 °C/min and 300 °C/min, respectively. The average Young's modulus (E_c and E_t) of the specimens heated according to ISO 834 are almost the same as the values obtained by applying a heating rate of

300 °C/min. Therefore, high speed heating has both, negative and positive influence on the stiffness of granite. Despite the significant difference in heating rate (e.g. 5 °C/min vs. 300 °C/min), Young's modulus does not change remarkably. Compared with the influence of temperature, the impact of heating rate on Young's modulus can be neglected.

(a) Tangent modulus E_t (b) Threshold modulus E_c
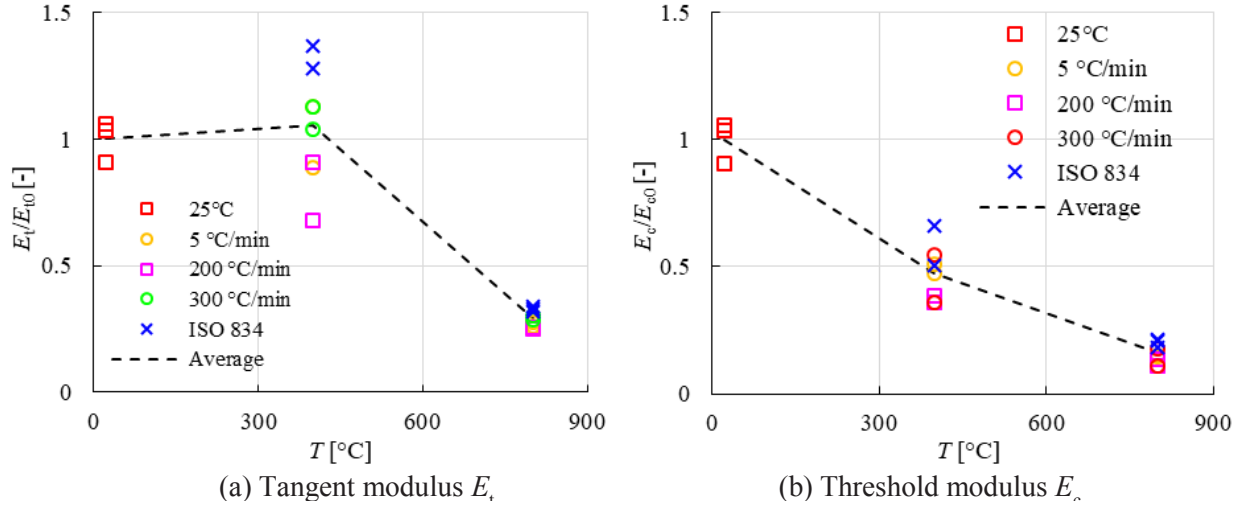
Figure 3-9 Normalized Young's modulus versus temperature for different heating rates

(a) Tangent modulus E_t (b) Threshold modulus E_c
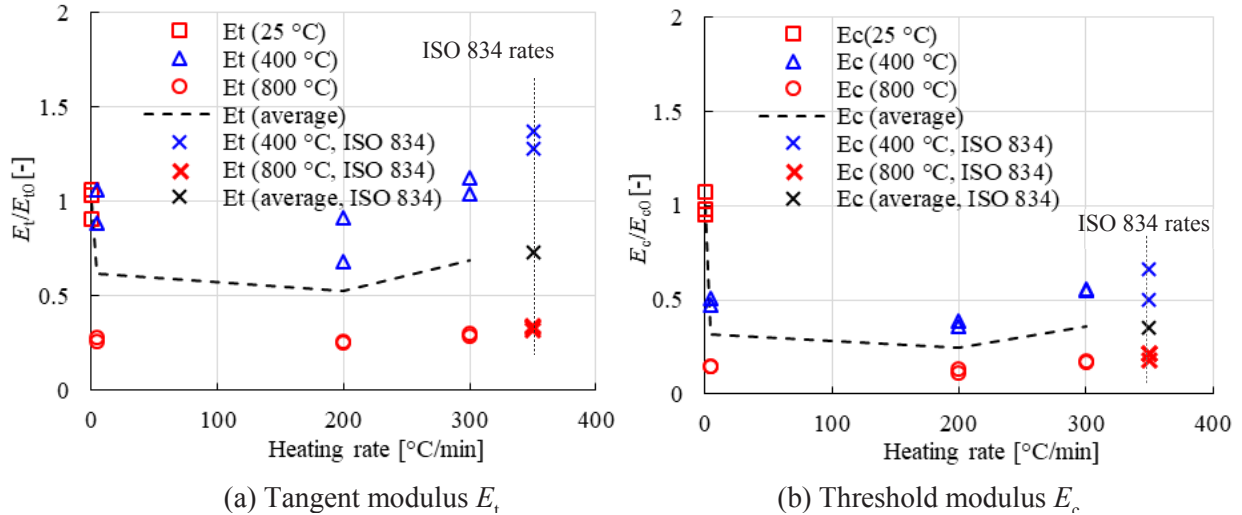
Figure 3-10 Normalized Young's modulus versus heating rate at different desired temperatures

3.1.3.2 Uniaxial compressive strength

Figure 3-11 shows the influence of maximum temperature and heating rate on UCS of granite. For specimens tested with the same heating rate, a pronounced dependence of UCS on maximum

temperature is observed (see Figure 3-11a). The decrease of average uniaxial compressive strength is about 9 % at 400 °C, and then becomes 54 % at a temperature of 800 °C. However, heating rates do not have a strong influence on UCS (see Figure 3-11b). When heated to 400 °C, the average UCS for rates of 5 °C/min, 200 °C/min, 300 °C/min and according to ISO 834 are 114.17 MPa, 110.28 MPa, 118.19 MPa and 114.56 MPa, respectively. These similar values indicate that the variation of UCS is more likely caused by the inhomogeneity of granite specimens. Compared to the impact of temperature, the influence of heating rate on UCS can be neglected.

(a) Target temperature (b) Heating rate
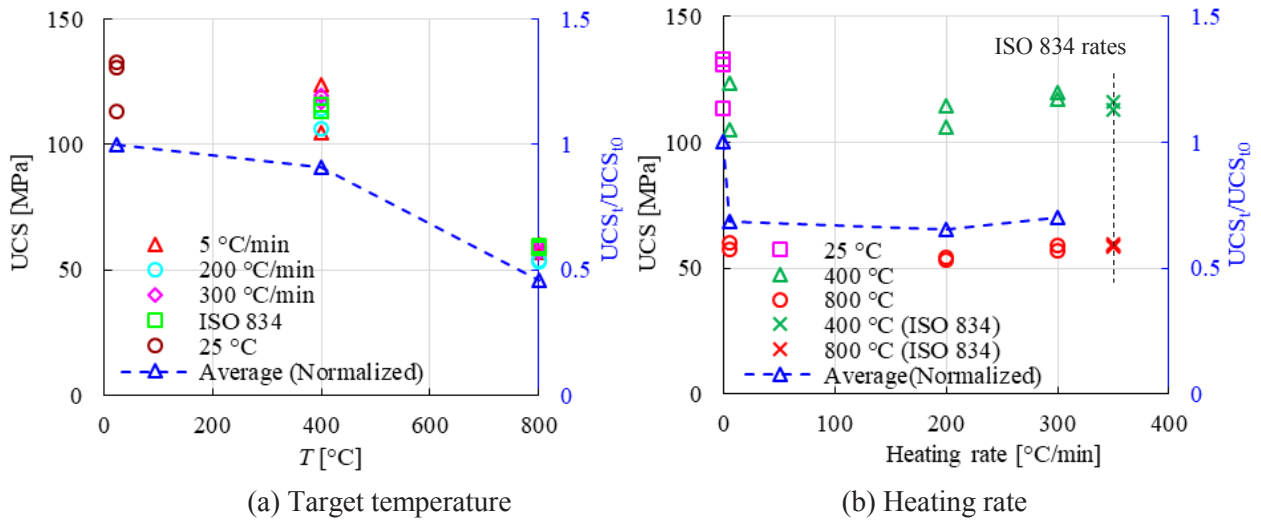
Figure 3-11 UCS versus temperature and heating rate

3.1.3.3 Deformation

The peak axial strain shows an obvious temperature dependence (see Figure 3-12a). The average peak axial strains at 400 °C and 800 °C are about 2 and 3 times the value at room temperature, respectively. The peak axial strain is also influenced by the heating rate to some extend (see Figure 3-12b). When being heated to 800 °C with 200 °C/min, the average strain is 12.5 % larger than applying a rate of 5 °C/min. Compared with 5 °C/min, the value for 300 °C/min shows a strain reduction of 14 % at 800 °C. A temperature dependence of strain is also observed for the 400 °C heating scenario. Compared to the 5 °C/min case, the strain will increase firstly for 200 °C/min and then decrease to a lower level for 300 °C/min.

The normalized average values ($\varepsilon_t/\varepsilon_{t0}$) show that the peak axial strains at 400 °C and 800 °C are 1.9 and 2.8 times higher than that of 25 °C, respectively (see Figure 3-12a). However, the peak axial

strains for 200 °C/min and 300 °C/min are only 1.20 and 0.89 times the value for 5 °C/min (see Figure 3-12b). Therefore, the heating rate has an obvious influence on the deformation of granite, but is relatively small compared to the influence of maximum temperature.

(a) Target temperature (b) Heating rate
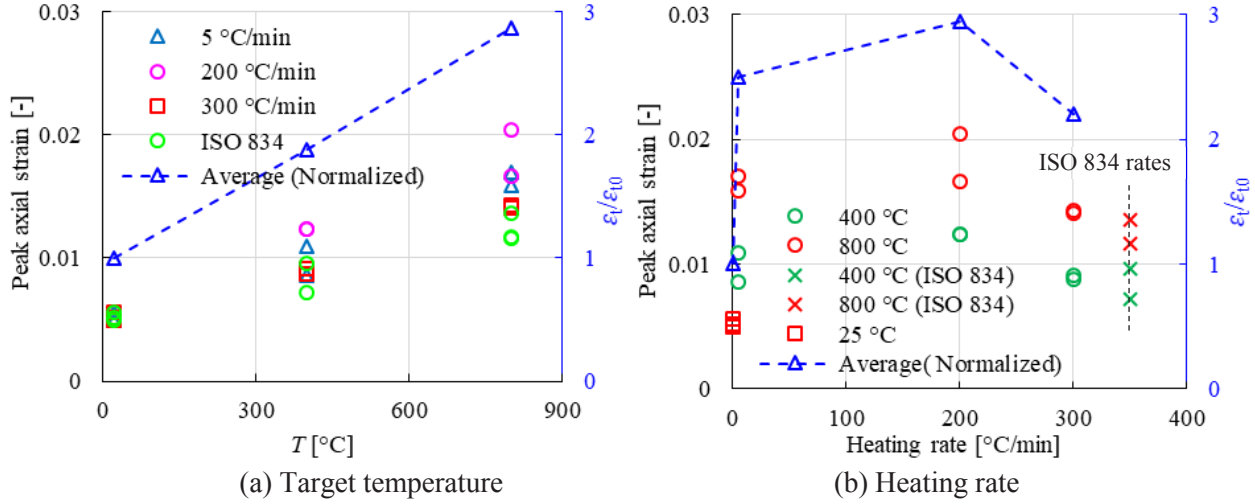
Figure 3-12 Peak axial strain versus temperature and heating rate

3.1.3.4 Failure modes

All the tested samples showed a clear shear fracture mode. Therefore, the Mohr–Coulomb strength criterion which is based on cohesion and friction angle may be used as failure criterion. In respect to the shear plane, the relationship between the internal friction angle φ (see Figure 3-13a) and the failure angle α (see Figure 3-13b) is:

$$\alpha = \pi/4 + \varphi/2 \tag{3-1}$$

UCS σ_c is related to cohesion c (see Figure 3-13a) and friction angle φ by:

$$\sigma_c = 2c \cdot \cos\varphi/(1-\sin\varphi) \tag{3-2}$$

The observed failure modes of the granite samples which experienced various heating scenarios are documented in Table 3-2. The samples are more likely to be crushed into smaller blocks and more segments/powder at higher temperatures. Compared with the specimens at room temperature and low heating rate of 5 °C/min, those which experienced high speed heating (200 °C/min, 300 °C/min and ISO 834) usually generate tapered blocks at failure. The red lines in Table 3-2 indicate the failure angle α (see Figure 3-13b). Based on Eq. (3-1) and (3-2), the corresponding values for cohesion and friction angle are back-calculated and documented in Table 3-3.

(a)   (b)
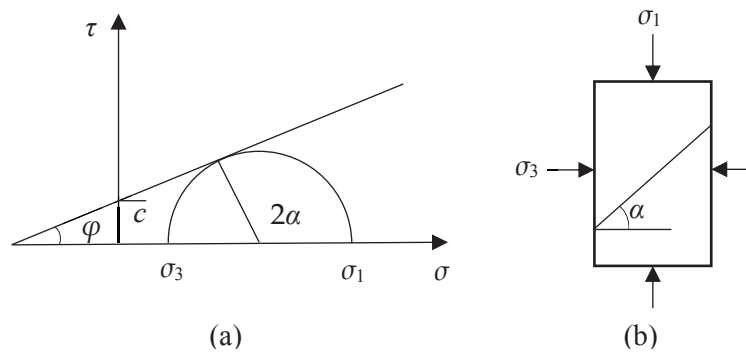
Figure 3-13 Sketch of the Mohr-Coulomb strength criterion: (a) Strength envelop in the shear stress - normal stress diagram, (b) shear plane inside the specimen

Table 3-2 Failure modes of granite after various heat treatments
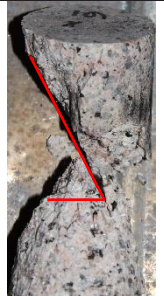
| **Ref. 1** | **Ref. 3** | **C-1-2** | **C-1-6** | **C-1-4** | **C-1-5** |
| Room temperature, 25 °C | | 5 °C/min, 400 °C | | 5 °C/min, 800 °C | |

| **C-3-1** | **C-3-2** | **C-3-4** | **C-3-5** | **C-2-1** | **C-2-2** |
| 200 °C/min, 400 °C | | 200 °C/min, 800 °C | | 300 °C/min, 400 °C | |

| **C-2-4** | **C-2-5** | **C-4-1** | **C-4-2** | **C-4-4** | **C-4-6** |
| 300 °C/min, 800 °C | | ISO 834, 400 °C | | ISO 834, 800 °C | |

Table 3-3 Failure angles and backcalculated shear parameters

No.	Specimens	Heating rate, target temp.	α [°]	σ_c [MPa]	φ [°]	c [MPa]
1	Ref.1	0 °C/min, 25 °C	65	113.37	40	26.43
2	Ref.3	0 °C/min, 25 °C	64	132.78	38	32.38
3	C-1-2	5 °C/min, 400 °C	65	104.75	40	24.42
4	C-1-4	5 °C/min, 800 °C	63	59.97	36	15.27
5	C-1-5	5 °C/min, 800 °C	69	57.25	48	10.98
6	C-1-6	5 °C/min, 400 °C	63	123.59	36	31.48
7	C-2-1	300 °C/min, 400 °C	62	119.5	34	31.76
8	C-2-2	300 °C/min, 400 °C	67	116.88	44	24.80
9	C-2-4	300 °C/min, 800 °C	63	56.88	36	14.49
10	C-2-5	300 °C/min, 800 °C	65	59.11	40	13.78
11	C-3-1	200 °C/min, 400 °C	63	114.28	36	29.11
12	C-3-2	200 °C/min, 400 °C	59	106.28	28	31.92
13	C-3-4	200 °C/min, 800 °C	64	53.35	38	13.01
14	C-3-5	200 °C/min, 800 °C	65	54.09	40	12.61
15	C-4-1	ISO 834, 400 °C	62	116.03	34	30.84
16	C-4-2	ISO 834, 400 °C	68	113.09	46	22.84
17	C-4-4	ISO 834, 800 °C	65	58.68	40	13.68
18	C-4-6	ISO 834, 800 °C	66	59.82	42	13.31

Note: C-4-3 was not analyzed due to the abnormal stress-strain behavior, while the failure mode of C-4-5 was not documented by mistake.

To investigate the variation of cohesion and friction angle, normalized friction angle φ_t/φ_{t0} and normalized cohesion c_t/c_{t0} (in each case related to value at room temperature) are calculated for different heating scenarios (see Figure 3-14 and Figure 3-15). For a heating rate of 5 °C/min, the friction angle at 400 °C is almost the same as the value at room temperature while the value at 800 °C is slightly higher (see Figure 3-14a). For a rate of 200 °C/min, the friction angle shows a slight reduction at 400 °C and the value at 800 °C does not show a change compared with room temperature (see Figure 3-14b). For heating rates of 300 °C/min or according to ISO 834, the friction angles are nearly the same as the value at room temperature. This is in agreement with previous findings that friction angle does not change significantly at elevated temperatures (Tian et al. 2016; Kumari et al. 2017b; Wang and Konietzky 2019). Also, the friction angle is not heating-rate dependent as well. Except for a slightly lower value at 400 °C reached with a heating rate of 200 °C/min (Figure 3-15a), the friction angles do not show obvious variations for different heating rates (see Figure 3-15). However, the cohesion shows a significant temperature dependence (see Figure 3-14). When heated to 400 °C, the cohesion is similar to that one at room temperature. A significant decrease of about 50 % occurs at 800 °C for all the specimens independent on various heating rates. Compared with maximum temperature, the influcence of heating rate is negligible.
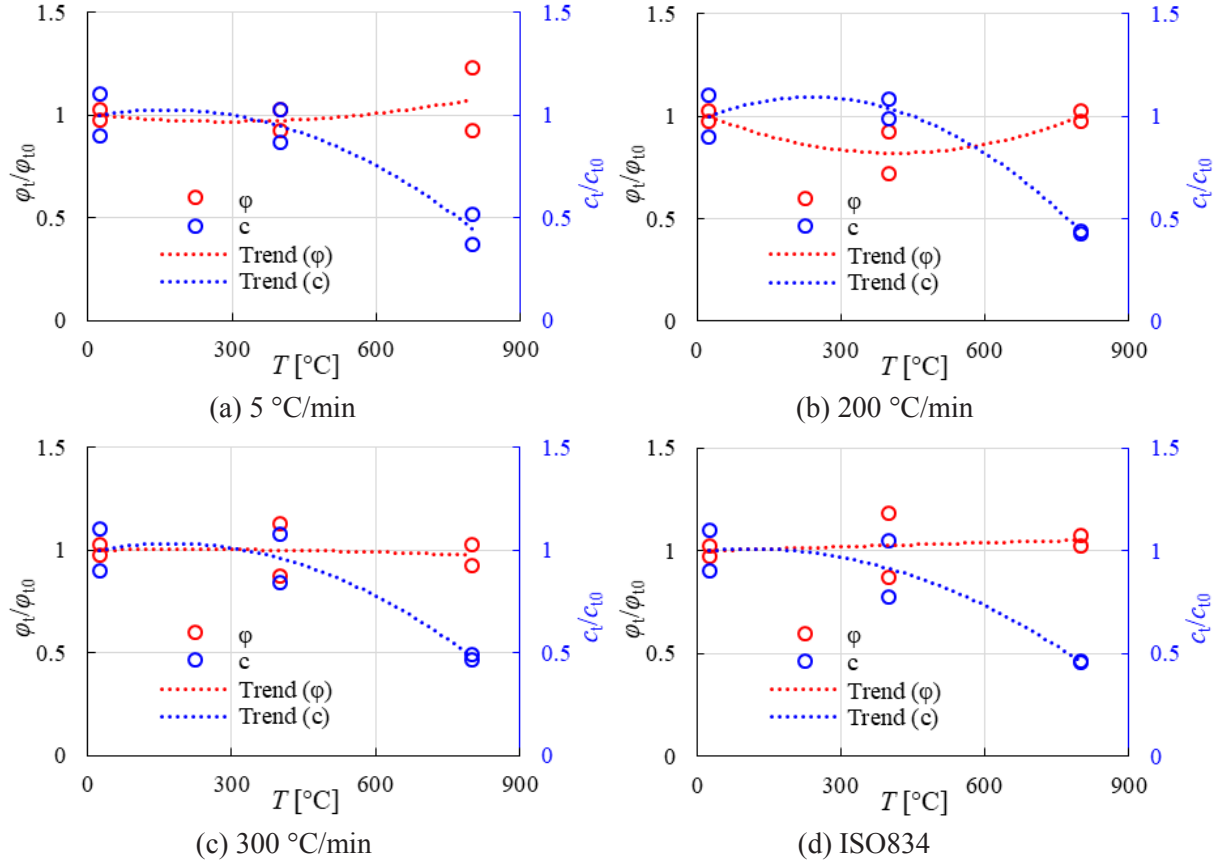
Figure 3-14 Normalized friction angle φ and cohesion c at different temperatures considering various heating rates
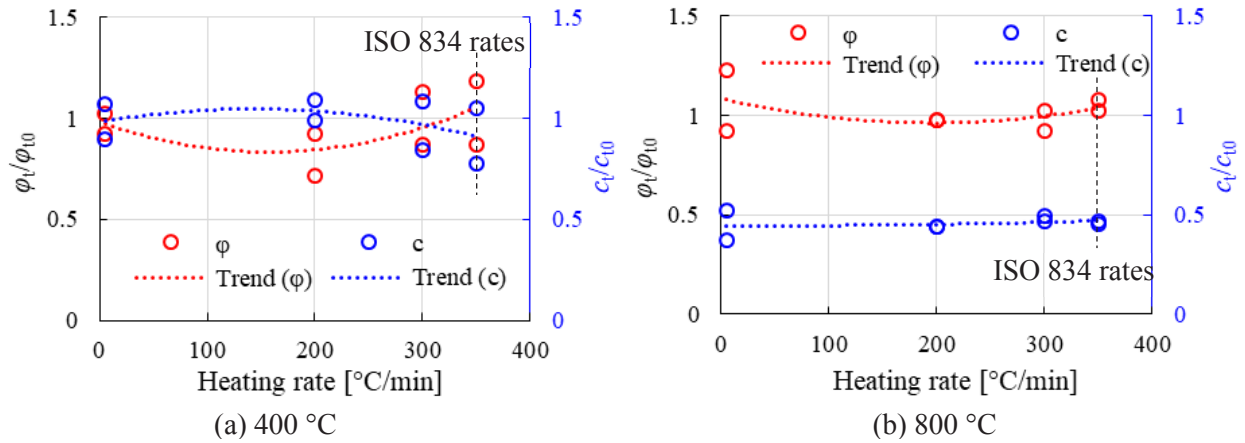
Figure 3-15 Normalized friction angle φ and cohesion c at different heating rates considering various temperatures

3.2 Thermal properties of Eibenstock granite

Except for the test of thermal conductivity (conducted at Wuhan University of Science and Technology), thermal expansion tests were finished at TU Bergakademie Freiberg, Germany (Weinhold 2018).

To determine the coefficient of linear thermal expansion, four granite samples with a diameter of 5 mm and nominal length of 20 mm were heated up to 1000 °C with 5 °C /min. The test was conducted with a dilatometer at the Institute of Ceramic, Glass and Construction Materials at TU Bergakademie Freiberg. Thermal diffusivity, thermal conductivity and specific heat capacity were measured using a NETZSCH Laser Flash Apparatus LFA 457 at Wuhan University of Science and Technology, China. The nominal specimen dimension of the three discs is 12.5 mm in diameter and 2.5 mm in thickness. The thermal conductivity is calculated by the following equation:

$$\lambda(T) = \kappa(T) \cdot C_p(T) \cdot \rho(T) \tag{3-3}$$

where λ is thermal conductivity [W/(m K)], κ is thermal diffusivity [mm^2/s], C_p is specific heat [J/(g K)], ρ is bulk density [g/cm^3].

3.2.1 Specific heat , thermal conductivity and thermal diffusivity

Figure 3-16 shows specific heat (Figure 3-16a), thermal conductivity (Figure 3-16b) and thermal diffusivity (Figure 3-16c) measured by the Laser Flash Apparatus. The specific heat capacity shows a continuous increase with temperature from 0.706 J/(g K) at 25 °C to 0.912 J/(g K) at 600 °C. Afterwards, it decreases slightly to 0.895 J/(g K) at 800 °C. Thermal conductivity and thermal diffusivity show a similar trend and decrease monotonically with rising temperature. At room temperature, thermal conductivity of the tested granite is 3.65 W/ (m K). At higher temperatures, especially for temperatures higher than 600 °C, thermal conductivity decreases much slower and approaches a nearly constant value of approximately 1.2 W/(m K). Similar, the thermal diffusivity diminishes from 2.0 mm²/s at room temperature to app. 0.5 mm²/s at 600 °C and 800 °C.

The reason why thermal diffusivity and thermal conductivity approach constant values at high temperatures is explained by Wen et al. (2015): Thermal diffusivity is connected with the number

of phonons within the primitive unit cell, and an increasing temperature no longer significantly changes the number of phonons when temperature is high enough; the phonons are limited in space with a constant lattice size, and the mean free phonon path no longer decreases with increasing temperatures, which limits the thermal conductivity values of the rocks at high temperatures.

(a) Specific heat (b) Thermal conductivity (c) Thermal diffusivity
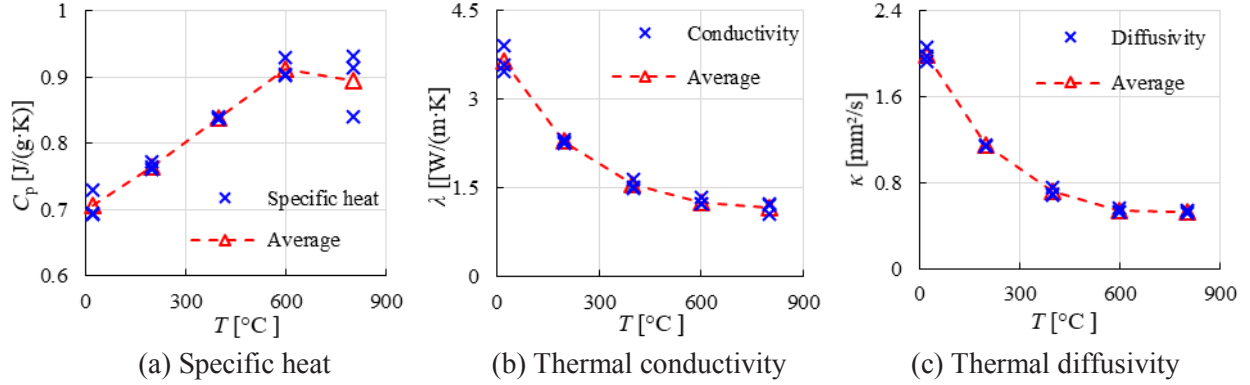
Figure 3-16 Thermal properties measured by the Laser Flash Apparatus

3.2.2 Linear thermal expansion coefficient

The formulas for calculating the thermal expansion coefficient can be grouped into two categories, depending on whether the expansion relates to a temperature range or a single temperature (James et al. 2001). The most general definition of average coefficient of linear thermal expansion over a temperature range is:

$$\alpha_m = \frac{(L_2 - L_1)/L_0}{T_2 - T_1} = \frac{1}{L_0}\frac{\Delta L}{\Delta T} \tag{3-4}$$

where L_0 is the initial length of specimen at temperature T_0 which expands to L_1 at T_1 and then to L_2 at T_2, ΔL is the change in length for the temperature change ΔT.

The true coefficient of linear thermal expansion is related to the derivative dL/dT, and it can be defined as follows (James et al. 2001):

$$\alpha_T = \frac{dL/L}{dT} = \frac{1}{L}\frac{dL}{dT} \tag{3-5}$$

Based on the equations above, the average coefficient over a temperature range of 25 °C at target temperature (Figure 3-17a) and the true coefficient at a single temperature (Figure 3-17b) are

plotted. The coefficient defined over a temperature range is significantly different from that defined at a single temperature. This difference has important implications if used in numerical models and engineering applications. Since TM-coupled calculations use the parameters at a certain temperature, we only use the true coefficient in the numerical models presented in this study. It reveals that the coefficient of linear thermal expansion shows the first sharp increase at around 573 °C and experiences a second increase in the range between 870 - 980 °C.
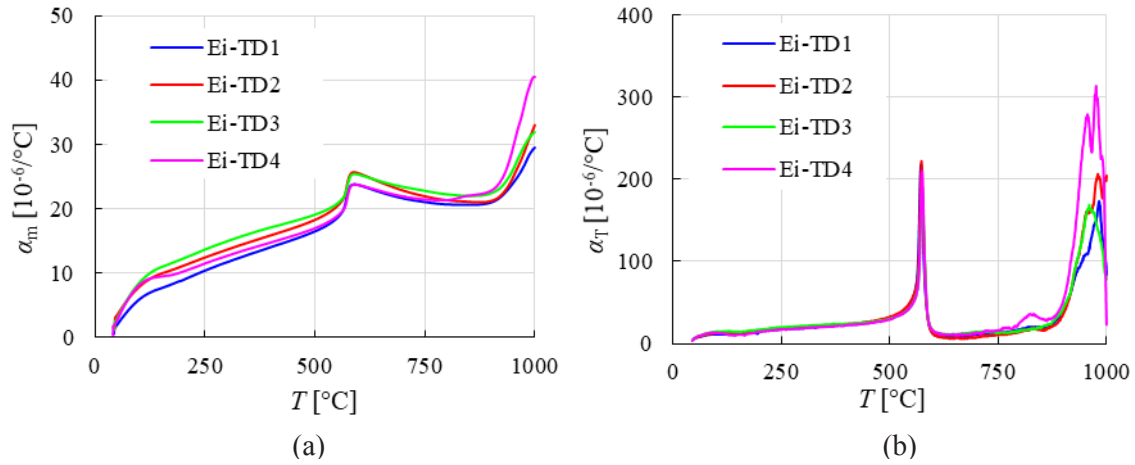
Figure 3-17 Linear thermal expansion coefficient of granite after heat treatment: (a) Average over 25 °C and (b) for single temperature

4 Properties of Eibenstock granite after heat treatments

This chapter describes the influence of temperature and high speed heating on properties of granite after heat treatments, that means the physical and mechanical properties were tested at room temperature after the samples have exposed to elevated temperature.

Chapter 4.1 focus on thermal induced cracks and tensile strength of Eibenstock granite after being subjected to high speed heating. The Digital Image Correlation (DIC) technique was used for analysing the damage behaviour of granite during the high speed heating process. For samples heated-up to 800 °C with heating rates of 200 °C/min and 300 °C/min, thermal induced macrocracks become visible to the naked eyes, while no obvious macrocracks are observed on samples heated according to ISO 834 curve. Compared to the influence of temperature, the selected heating rates only have a negligible impact on tensile strength and axial displacement. The DIC analysis shows the crack initiation and progressive crack propagation before the main crack is formed at failure. Compared to the samples heated-up to 400 °C, the samples heated-up to 800 °C show less brittle fracture behaviour, and the tensile strength is greatly reduced. The final failure patterns confirm that different heating scenarios lead to different microcrack pattern and consequently influence the failure mode at the macroscopic scale.

Chapter 4.2 documents the impact of temperature up to 1000 °C on physical and mechanical properties and the general thermo-mechanical coupled behaviour of Eibenstock granite. The measured physical properties including mineral composition, density, P-wave velocity, and open porosity are temperature-dependent. P-wave velocity and porosity variations indicate continuous crack evolution at elevated temperatures and pronounced crack coalescence from 600 °C to 1000 °C. Uniaxial compression and Brazilian tests were carried out to measure UCS, Young's modulus, stress-strain relationship, and tensile strength of Eibenstock granite before and after thermal treatment, respectively. Test results show that UCS slightly increases from 25 °C to 400 °C before decreasing rapidly up to 1000 °C, while Young's modulus and tensile strength decrease continuously with rising temperature. Failure characteristics changes from brittle failure up to a temperature of about 600 °C to ductile behaviour at 800 °C and 1000 °C.

4.1 The influence of high speed heating on tensile behavior of granite

4.1.1 Sample description and test setup

21 Brazilian discs are prepared for Brazilian tests (see Table 4-1). Both ends of the samples were grinded and polished in order to make both ends smooth and parallel. The Brazilian discs have a nominal diameter of 50 mm and a thickness of 25 mm (thickness to diameter ratio of 0.5). To meet the requirements of high speed heating, the supersonic frequency induction heating equipment (see Figure 3-4 and Figure 4-1a) was used. Three unheated (stored at room temperature of about 25 °C) Brazilian discs are prepared as reference samples. The other specimens are heated at ambient pressure to predetermined temperatures (400 °C and 800 °C) with high heating rates of 200 °C/min and 300 °C/min. Besides the constant heating rates, samples are also heated to 400 °C and 800 °C according to ISO 834 fire time-temperature equation (ISO 1999). Three samples are prepared for each heating scenario to consider statistical scatter of individual test results. Except for the samples at room temperature and those with ISO 834 heating scenario, all the other samples were kept at target temperature for a dwelling time of 1 hour (Richter and Simmons 1974; Brotóns et al. 2013; Heap et al. 2013) to guarantee uniform temperature distribution across the specimen. The ISO 834 heating scenario is used for testing the temperature resistance of the granite sample during a real fire. The test load for the Brazilian tests was applied by Wance Universal Testing Machine (Shenzhen) with a maximum load of 100 kN. The loading jaws (Figure 4-1b) were used for indirect tension tests as recommended by ISRM (1978).

Generally, crack investigations can be divided into direct and indirect methods (Lin 2002). Microscope and scanning electron microscope (SEM) observations are direct methods for detecting the shape and features of microcracks. Monitoring of AE, differential strain analysis (DSA), mercury intrusion porosimetry etc. are often used for the evaluation of structural and physical features of microcracks as indirect methods. Compared with these detecting methods, Digital Image Correlation (DIC) is as promising alternative to obtain full-field measurements (Fourmeau et al. 2014). This non-contact measurement technique can be used to visualize the surface deformation of the loaded specimen after heat treatment. As a non-contact full-field measurement method, DIC can track homologous points on the specimen surface at different deformation stages and fracture processes (Dai et al. 2017). The DIC technique is applied as an effective way for

detecting crack propagation of granite after heat treatment. The DIC analysis makes it possible to locate the crack initiation and monitor the development of crack pattern accurately.

Table 4-1 Heating scenarios for Brazilian discs

No.	Diameter [mm]	Thickness [mm]	Heating scenario	Target temperature + Holding time	DIC
1	50.35	26.02	No heating	25 °C	Yes
2	50.33	25.31	No heating	25 °C	Yes
3	50.33	25.24	No heating	25 °C	Yes
4	50.37	25.42	300 °C/min	400°C+1h	Yes
5	50.33	25.41	300°C/min	400°C+1h	Yes
6	50.35	25.17	300°C/min	400°C+1h	Yes
7	50.31	25.53	300°C/min	800°C+1h	Yes
8	50.36	25.45	300°C/min	800°C+1h	Yes
9	50.37	25.82	300°C/min	800°C+1h	Yes
10*	50.32	26.48	200°C/min	400°C+1h	Yes
11	50.37	25.49	200°C/min	400°C+1h	Yes
12	50.34	25.85	200°C/min	400°C+1h	Yes
13	50.36	25.84	200°C/min	800°C+1h	Yes
14	50.37	25.42	200°C/min	800°C+1h	Yes
15	50.36	25.35	200°C/min	800°C+1h	Yes
16	50.34	25.31	ISO 834	400°C	Yes
17	50.32	25.07	ISO 834	400°C	Yes
18	50.34	25.70	ISO 834	400°C	Yes
19	50.35	25.25	ISO 834	800°C	Yes
20	50.36	25.44	ISO 834	800°C	Yes
21	50.34	25.39	ISO 834	800°C	Yes

* The stress-displacement data of #10 was lost by accident

All the samples are naturally cooled down inside the heating device to room temperature and then prepared for Brazilian tests with DIC measurement. White spots are sprayed on a thin black opaque layer of the Brazilian discs after cooling to room temperature (see Figure 4-2). This helps to increase the contrast and to obtain a random distribution of grey level on the specimen surface (Dai et al. 2017). The Brazilian discs were compressed with 0.25 mm/min to obtain the tensile strength of the granite specimen experienced elevated temperatures according to following equation:

$$\sigma_t = \frac{2P_{max}}{\pi DB} \tag{4-1}$$

where P_{max} is the maximum load, D is the diameter of the disc, and B is the thickness of the disc.

In order to investigate the fracture evolution characteristics of the specimens during compression, the DIC camera continuously monitored the discs (see Figure 4-1b). The DIC camera was placed

at a distance of around 1.0 m away from the specimen to protect the camera optics from granite fragments (Figure 4-1b). The type of the camera is AVT Stingray 504, which has a maximum frame rate of 9 fps at full resolution of 2452 (H) × 2056 (V) pixels. Pictures of the sample were captured at a frequency of 1 picture per second.

(a) Induction heating device   **(b)** Configuration of DIC system
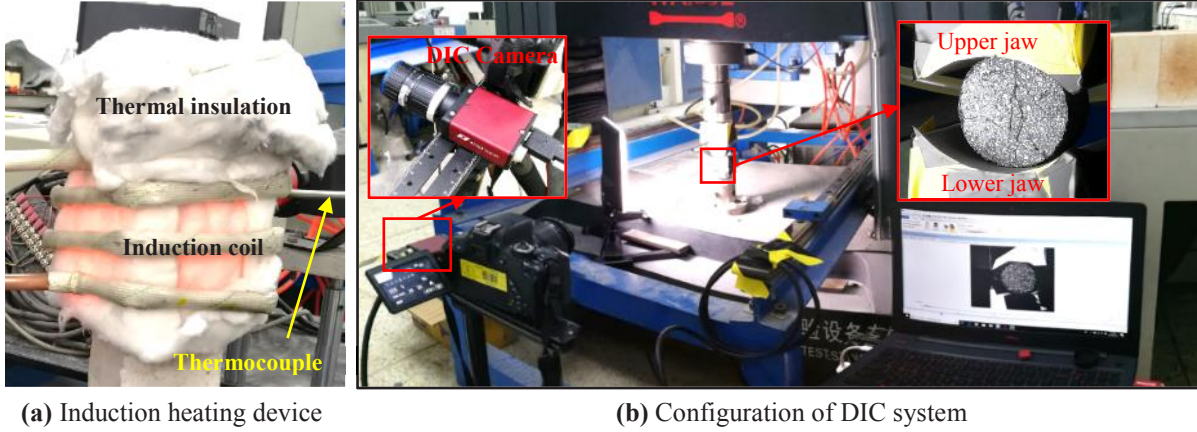
Figure 4-1 Experimental set-up for Brazilian test with DIC monitoring

Ten pictures of the undeformed sample are captured before loading. They are used as reference states for computing the motion of each image point in different states after deformation. Square reference subsets centered at the considered points are chosen and tracked in the deformed images according to the selected correlation function. By optimizing the correlation coefficient, the location of a subset in the deformed image is found and the displacement components of this subset center can be determined (Pan et al. 2009; Xia and Yao 2015). The correlation coefficient used in this study is given by:

$$C=1-\frac{\sum_{\underline{X}\in D}(f(\underline{X})-\overline{f}_D)\cdot(g(\phi(\underline{x}))-\overline{g}_D)}{\sqrt{\sum_{\underline{X}\in D}(f(\underline{X})-\overline{f}_D)^2}\cdot\sqrt{\sum_{\underline{X}\in D}(g(\phi(\underline{x}))-\overline{g}_D)^2}} \qquad (4-2)$$

where ϕ is local strain variation of the material, f specifies the gray levels of the reference states ($\underline{X}$), g represents the grey levels of the deformed states ($\underline{x}$), $\overline{f}_D$ and $\overline{g}_D$ are the averages of gray level values on subset D.

A subset size of 31×31 pixels is used to track the corresponding displacement field in the deformed image. The distance between the center points of two consecutive subsets, i.e. step size, is $m = 6$ pixels. Based on the correlation coefficient given above, the full-field displacements as well as the

vertical and horizontal displacement components of the subset center points can be determined. In order to calculate the strains of a point, a square window containing $(2m +1) \times (2m + 1)$ discrete points (i.e. strain calculation window) around it should be selected (Pan et al. 2009). In this study, the strain window size used for strain calculation out from full-field displacement is set to 13×13 pixels. The size of the strain window suppresses the noise of the displacement field and avoids an unreasonable linear approximation of deformation within the strain calculation window.

Figure 4-2 Some Brazilian discs with white spots sprayed on the thin black opaque layer

4.1.2 Macro damage before loading

Specimen heated up to 400 °C are still intact from the macroscopic perspective, no obvious cracks can be directly observed. Figure 4-3 presents the macrocrack patterns induced by heat treatment up to 800 °C before loading. For samples heated up to 800 °C with heating rates of 200 °C/min and 300 °C/min, the thermal induced macrocracks are visible to the naked eyes (Figure 4-3a-g). The three Brazilian discs heated-up to 800 °C with 200 °C/min show different damage features. Only sample 14 (Figure 4-3b) shows a fracture across the sample in diameter direction, while only a few small cracks can be observed on samples 13 (Figure 4-3a) and 15 (Figure 4-3c). Compared with 200 °C/min, the higher heating rate of 300 °C/min results in more developed macrocracks (see Figure 4-3e, f, and g).

Thermal stresses are mainly controlled by the constituents of the rocks, the thermal expansion anisotropy within the minerals, and the thermal gradients (Yong and Wang 1980; Heap et al. 2013).

Since constituents, thermal expansion anisotropy and applied cooling rates of Eibenstock granite samples are quite similar, the thermal stress differences among different granite samples are mainly induced by the thermal gradients during the heating phase. Therefore, we can conclude that high speed heating leads to a strong thermal gradient, which in turn causes significant local damage to the Brazilian discs. However, for the samples heated-up according to ISO 834 to the target temperatures, no obvious macrocracks can be observed by naked eyes (see Figure 4-3h, i). This difference can be attributed to two reasons. One is that the heating rate of ISO 834 reduced greatly in the range between 400 and 800 °C, thus microcracks did not form macrocracks due to lower heating rate. Another fact is that there is no dwelling time at target temperature for the ISO 834 heating scenario.

(a) 200°C/min, 800°C	(b) 200°C/min, 800°C	(c) 200°C/min, 800°C
(e) 300°C/min, 800°C	(f) 300°C/min, 800°C	(g) 300°C/min, 800°C
(h) ISO834, 800°C	(i) ISO834, 800°C	(j) ISO834, 800°C
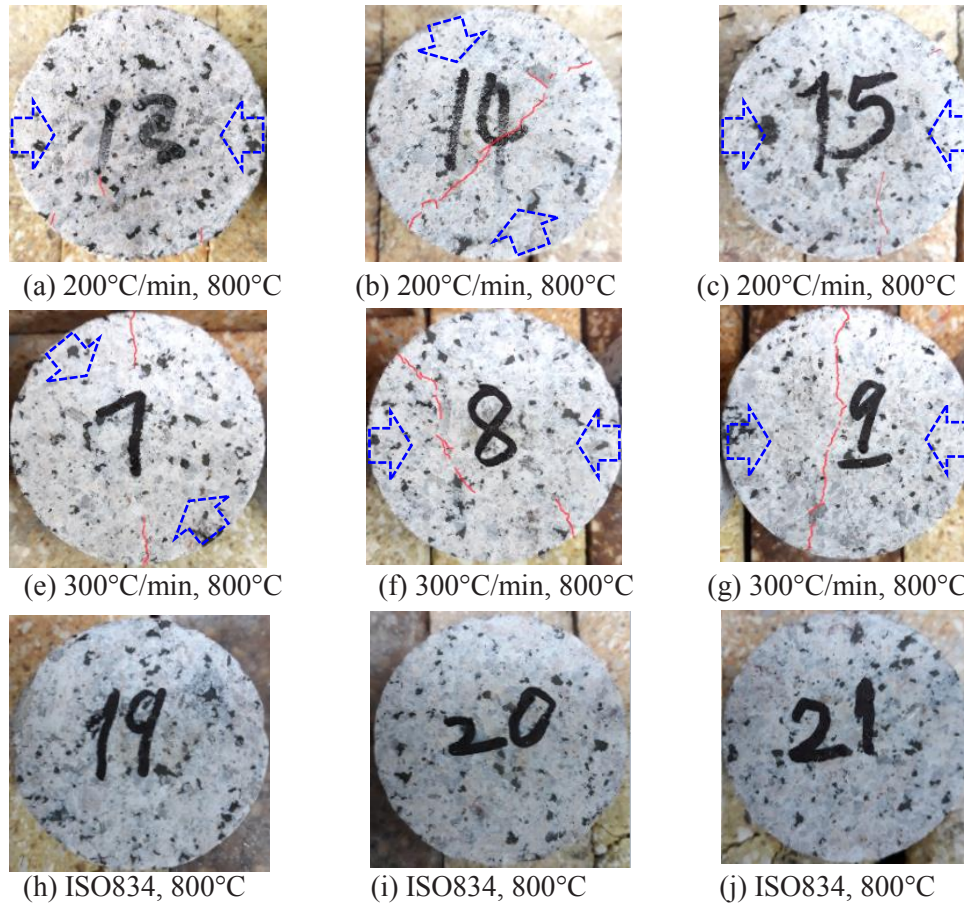
Figure 4-3 Macrocracks (red lines) induced by thermal stress on Brazilian discs before mechanical loading. The blue dashed arrows indicate the loading direction in the subsequent conducted Brazilian tests

4.1.3 Tensile strength

For specimens with macrocracks, parallelism of cracks and loading directions (see the dashed blue arrows in Figure 4-3) are avoided in the subsequent loading tests by choice of appropriate sample orientation. Although the loading direction in respect to thermal induced cracks can influence the stress-displacement behavior of Brazilian samples to some extent, the test results shown in Figure 4-4 document that the influence is small and does not affect the obtained conclusions. It is clear that the heat treatment has an obvious influence on the tensile behavior. Brazilian discs at 25 °C and heated-up before to 400 °C fail immediately after reaching the peak stress, showing clear brittle characteristics. When temperature rises to 800 °C, gradual loss of strength with ongoing deformation (soft decline in stress-displacement curve) becomes the dominant behavior. This means, when granites are exposed to very high temperatures (e.g. 800 °C), intensive damage by microcracking leads to a change in the behavior (and internal structure of the material): peak load is reduced and sudden, brittle failure is replaced by more ductile behavior characterized by gradual stress reduction with ongoing deformation.
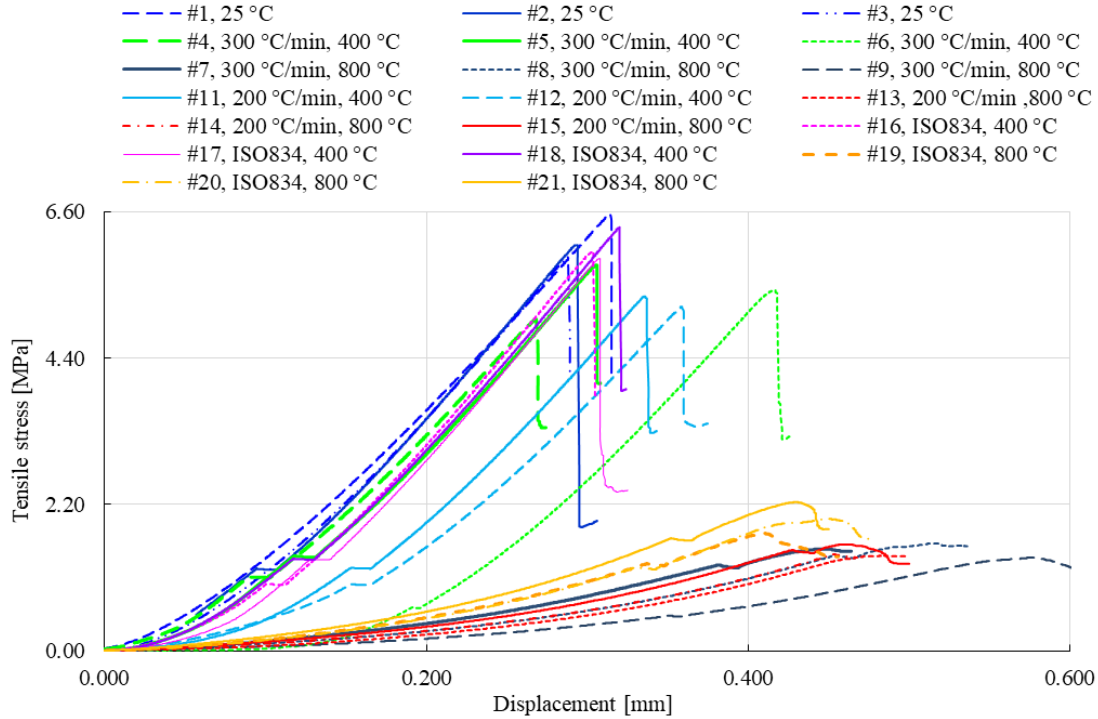
Figure 4-4 Tensile stress vs. displacement (Brazilian tests) of granite specimens exposed to various heating scenarios

Figure 4-5 shows tensile strength and peak axial displacement for different target temperatures considering various heating rates. The curves with same heating rate of 200 °C/min (Figure 4-5a), 300 °C/min (Figure 4-5b), and ISO 834 (Figure 4-5c) indicate that the tensile strength decreases with increasing temperature. Compared with specimens at room temperature, the average tensile strength of samples which experienced 400 °C is slightly reduced from 6.2 MPa to 5.62 MPa (Figure 4-5d). A significant strength decrease of about 4 MPa happens when samples experienced 800 °C, which can be attributed to the *α*-*β* quartz phase transition that occurs at roughly 573 °C, leading to extended microcracks in the specimen (Nasseri et al. 2009; Yin et al. 2015).

(a) 200 °C/min

(b) 300 °C/min

(c) ISO 834

(d) Average value
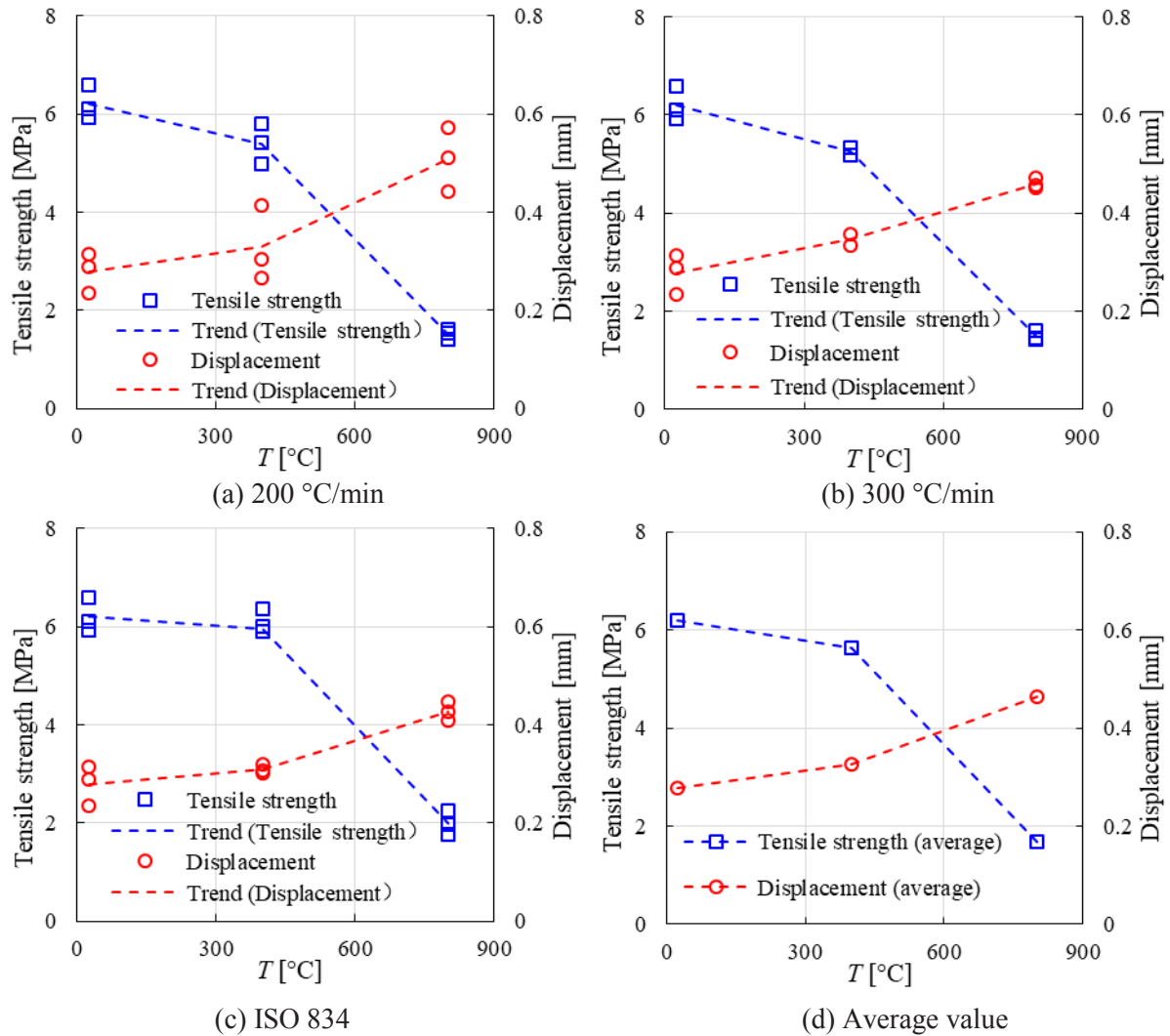
Figure 4-5 Tensile strength and peak axial displacement of samples sustaining different target temperatures considering various heating rates

The development of axial displacement at failure shows an opposite trend, i.e. the axial displacement is increasing with rising temperature. The average displacement of specimens shows the largest increase of 0.14 mm from 400 °C to 800 °C, indicating the influence of temperature on granite deformation.

Figure 4-6 documents tensile strength and peak axial displacement of samples for different heating rates considering various target temperatures. For samples heated up to 400 °C (Figure 4-6a), the average tensile strengths for 200 °C/min and 300 °C/min are very similar: 5.3 MPa and 5.4 MPa, respectively. The average tensile strength after heating up to 400 °C using ISO 834 heating rate is only 0.6 MPa higher than that for 300 °C/min. This trend is quite similar for 800 °C (Figure 4-6b): the tensile strength differences for different heating rates are less than 0.5 MPa. The influence of heating rates on axial displacement is also very small. The biggest variation of displacement caused by different heating rates happened for the 800 °C specimens with a difference of only 0.07 mm between the considered target temperatures (see Figure 4-6b). Compared with the influence of target temperature, the heating rate has only a small impact on tensile strength and axial displacement. However, according to the observed results, it is also clear that the stress gradient in the samples caused by the temperature gradient inside the sample during heat treatments is one reason for crack initiation.

(a) Target temperature: 400 °C   (b) Target temperature: 800 °C
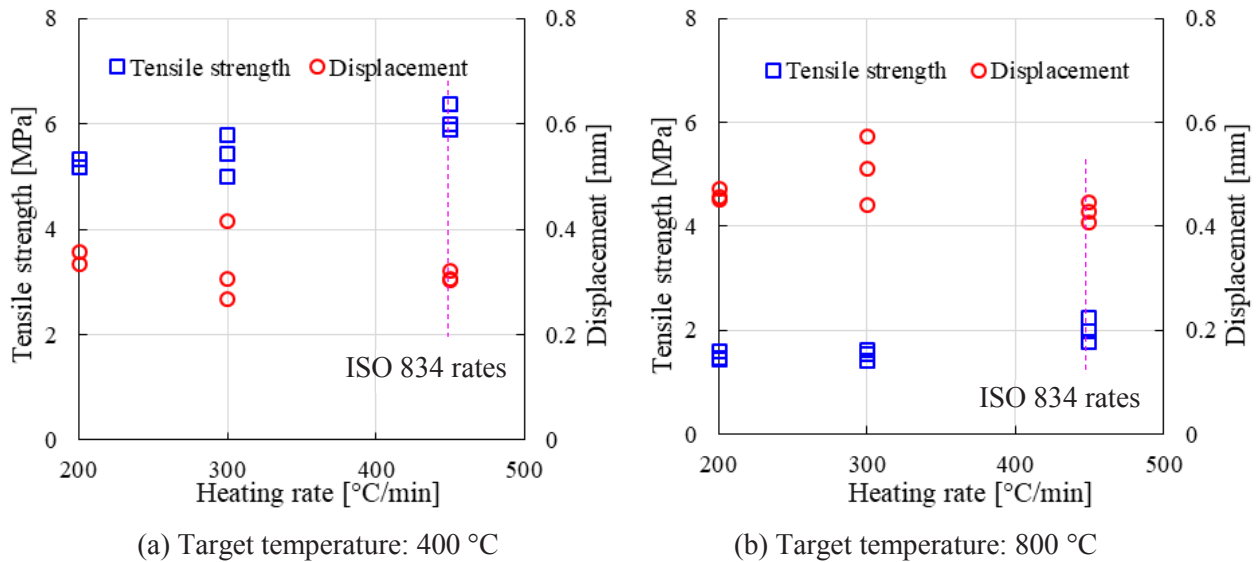
Figure 4-6 Tensile strength and peak axial displacement for different heating rates considering various target temperatures

4.1.4 DIC analysis of the tensile failure process

After recording the digital images of the specimen surface during loading, DIC computes the motion of each image point by comparing the digital images of the specimen before and after deformation. Since the influence of heating rate on tensile strength and displacement is relatively small and can be neglected compared to the impact of temperature, three samples with identical heating rate of 300 °C/min and different target temperatures (i.e. sample 3 at 25 °C, sample 5 at 400 °C and sample 7 at 800 °C) are adopted in this section for detailed illustration.

Figure 4-7 shows the full-field horizontal displacements of the three samples at failure during the Brazilian tensile test, where the failure moment refers to the next moment after reaching the maximum force. The black points represent the macrocracks formed up to this moment. For samples 3 and 5, wider and longer crack face openings are observed at failure, while only a few macrocracks appear in sample 7. This means macrocracks of samples 3 and 5 initiate along the diametrical direction instantaneously and split the sample into two halves, indicating a brittle characteristic of these two samples. The small number of cracks at failure observed in sample 7 (see Figure 4-7c) indicate ductile characteristics. The cracks are formed gradually until a loss of strength is observed. Compared with the ductility of the 800 °C sample, a granite after 400 °C treatment still remains brittle. This is related to the microcrack density which is much higher in the 800 °C samples. This also explains the stress-displacement curves shown in Figure 4-4.

(a) Sample 3, 25 °C   (b) Sample 5, 300 °C/min, 400 °C   (c) Sample 7, 300 °C/min, 800 °C
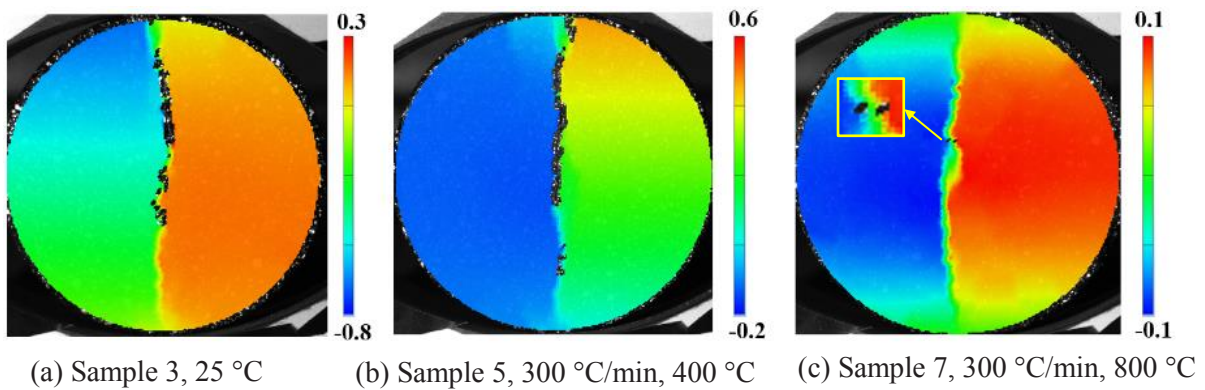
Figure 4-7 Full-field horizontal displacements [mm] of samples at failure (DIC) which experienced different heating scenarios

The displacements in vertical and horizontal directions at the mid-point of the central axis observed from start of loading up to immediately before failure and the instantaneous increase at failure are

documented in Figure 4-8. The vertical displacement stands for the deformation along the loading direction, while the horizontal displacement refers to the expansion of the specimen under load. For sample 7, the displacements after failure are also plotted. Samples 3 and 5 show significant increase of horizontal displacements due to sudden crack formation at failure moment (see Figure 4-8). This goes along with appreciable openings of tensile cracks and indication of sudden failure, i.e. brittle behavior. In contrast, the deformation magnitude of sample 7 is much larger from start of loading to immediately before failure compared to the other samples. Moreover, the deformation increment of sample 7 during failure is very small, indicating an obvious ductile behavior. Due to stable crack propagation the displacements just increase slightly after failure. The paths of central displacements again confirm that the granite samples at 25 °C and after 400 °C treatment still remain brittle, while the higher temperature of 800 °C leads to less brittle behavior.
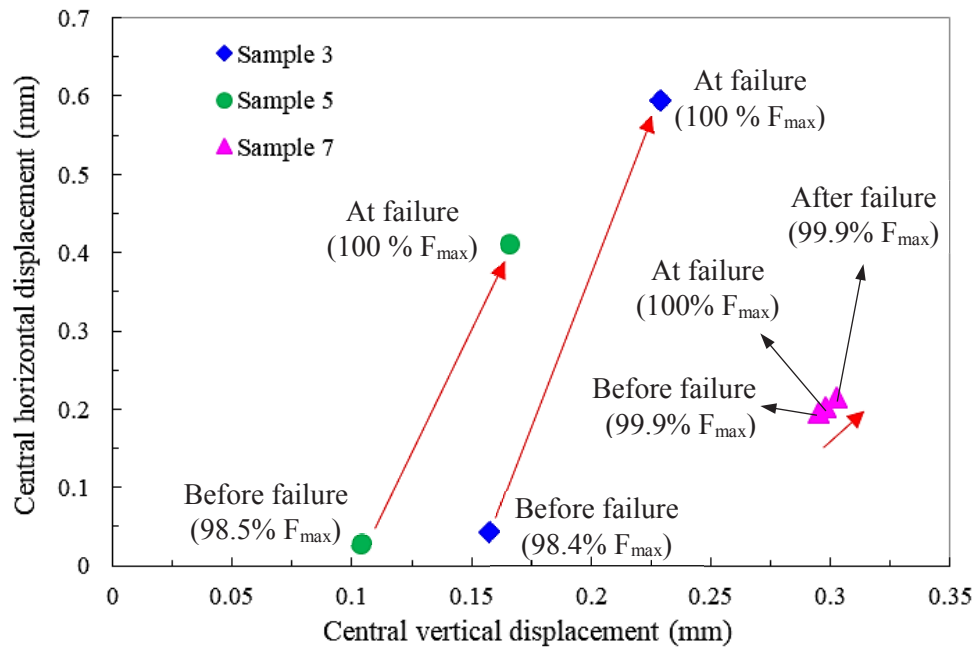
Figure 4-8 Horizontal vs. vertical displacements of centroid of samples just before and at failure

Figure 4-9 shows the DIC strains in horizontal direction for Brazilian discs at room temperature after heat treatment. The grey color represents strain larger than the upper limit of the color bar. The black points represent macrocracks formed at the moment captured. Strain change can be observed with DIC analysis before macrocracking at failure. For sample 3 without heating, a visible strain increment happens at 43 % F_{max}. The 400 °C sample shows that obvious strain occurs earlier at 39 % F_{max}. For the 800 °C sample, it has occurred at only 10 % F_{max}. The increased strain

represents the initiation of microcracks, which extend along the loading direction and then gradually merge and coalesce with increasing load. The main cracks crossing the discs have almost formed upon reaching the peak load at 100 % F_{max}. For brittle samples, the failure happens at the moment right after the peak load and the main crack forms within an extremely short time.

(a) Sample 3, 25 °C

(b) Sample 5, 300 °C/min, 400 °C

(c) Sample 7, 300 °C/min, 800 °C
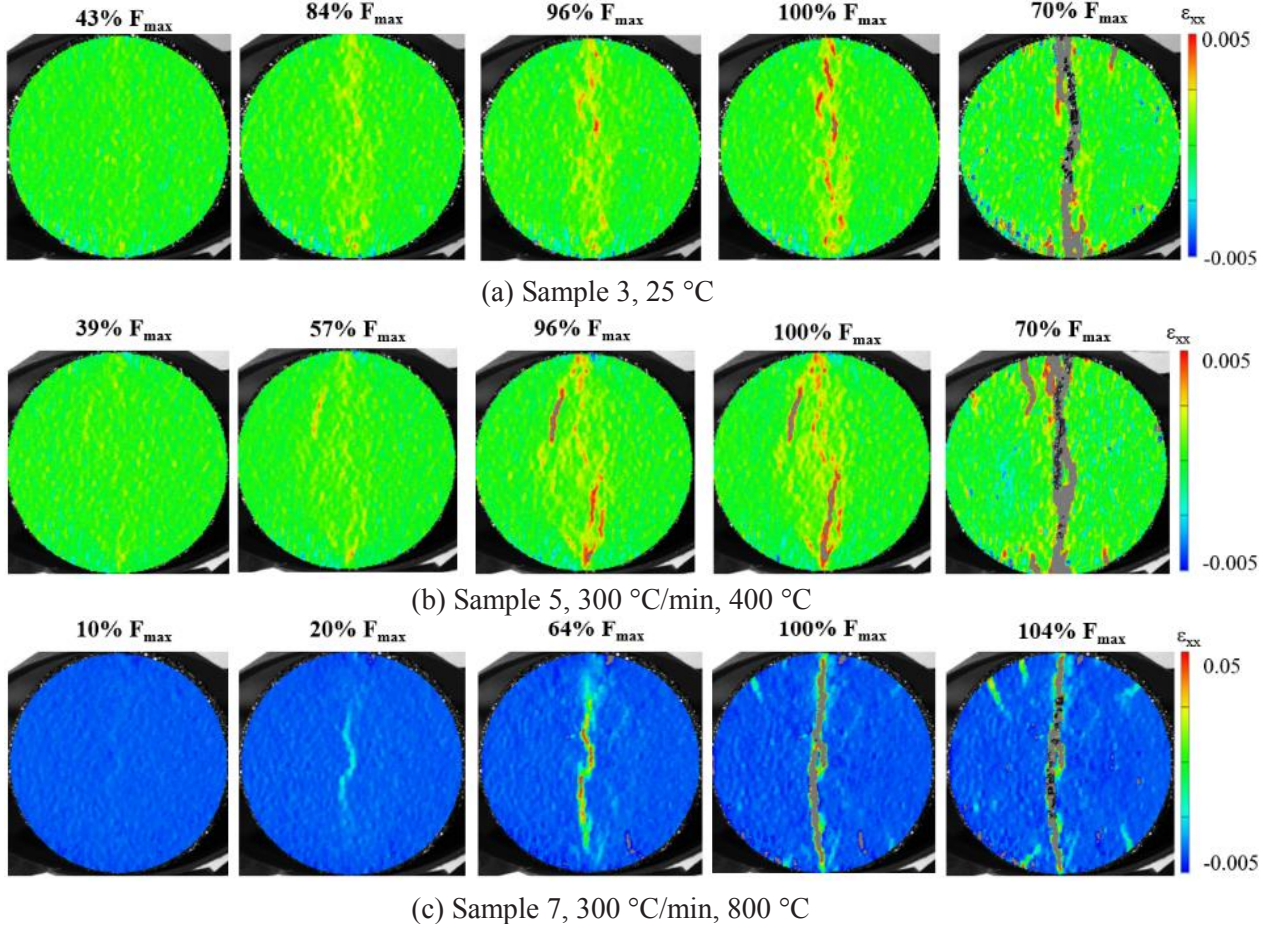
Figure 4-9 Horizontal strain ε_{xx} distribution (DIC) for specimens at different loading stages after experiencing different heating scenarios (Positive strain means expansion. Negative strain variations come from both, shrinkage and data errors. Negative values are very small compared with positive ones, and they are mainly used for image enhancement instead of representing the material deformation)

For all the samples, a clear tensile stress field can be inferred according to the strain distributions perpendicular to the loading direction. For the brittle samples 3 and 5 the stress field before failure leads to local strain concentrations which indicate further microcracks, rather than just a single main crack. The macrocrack of these samples initiates from the central part of the disc at peak load, and then instantaneously develops across the disc after reaching the peak load. Sample 7 shows a distinct difference: the main crack initiates from the center and propagates along the loading

direction gradually (not immediately) until failure. After the tensile failure, the loading can show a slight increase due to the resistance of the failed disc (see Figure 4-4 and Figure 4-9c). This sample also needs much larger strain to rupture than the brittle samples shown in Figure 4-9a and b, this is also why the color scaling in Figure 4-9c is different. Although the accuracy of determining crack initiation and failure moment is limited due to the picture acquisition frequency, the DIC analysis can help to locate and describe the crack development vividly.

4.1.5 Failure modes of samples after exposed to different heat treatments

Table 4-2 documents the failure modes (Brazilian test) of granite samples after different heat treatments. For granite without any heating, the specimens are separated into two roughly identical halves (see samples 1-3 in Table 4-2). This is because the initial cracks extend along the loading direction before other macrocracks initiate. Diametric microcracks connect, merge and finally form a macroscopic crack during the fracturing process, which causes the specimen to split into two parts.

When being heated before up to 400 °C with rates of 200 °C/min and 300 °C/min, the failure modes are similar to that of room temperature (see sample 4-6 and 10-12 in Table 4-2). However, the samples heated up before to 400 °C according to ISO 834 fire curve show a slight difference in terms of crack pattern (see sample 16-18 in Table 4-2). Both, a primary crack and some other sub-parallel cracks occur around the center of the sample along the loading direction. The reason might be that the continuous variation of heating rates according to ISO 834 heating scenario leads to different microcrack pattern. This difference in micro structures triggers different macroscopic failure modes. Significant changes can be observed in samples heated-up to 800 °C. Compared with samples at room temperature and 400 °C heating scenarios, more fractures and fragments can be observed in the 800 °C samples (e.g. sample 7-9 and sample 19-21 in Table 4-2). Beside the main crack parallel to the loading direction several sub-parallel secondary cracks as well as inclined shear-zones are observed in the specimens. Heating rate has an obvious influence on the failure mode for samples exposed to a temperature of 800 °C. The samples heated with 300 °C/min (sample 7-9 in Table 4-2) show more fractures along the loading direction than those heated with 200 °C/min (sample 13-15 in Table 4-2). The samples heated to 800 °C according to ISO 834 curve are damaged with the highest degree of fragmentation (sample 19-21 in Table 4-2). This indicates

that heating rate variations during the heating process can lead to different microcrack patterns, at least to some extent. This in turn influences the failure mode at the macroscopic scale.

Table 4-2 Failure modes of granite samples after exposure to high temperatures

(a) 25 °C	(b) 25 °C	(c) 25 °C	(d) 300 °C/min, 400 °C
(e) 300 °C/min, 400 °C	(f) 300 °C/min, 400 °C	(g) 300 °C/min, 800 °C	(h) 300 °C/min, 800 °C
(i) 300 °C/min, 800 °C	(j) 200 °C/min, 400 °C	(k) 200 °C/min, 400 °C	(l) 200 °C/min, 400 °C
(m) 200 °C/min, 800 °C	(n) 200 °C/min, 800 °C	(o) 200 °C/min, 800 °C	(p) ISO 834, 400 °C
(q) ISO 834, 400 °C	(r) ISO 834, 400 °C	(s) ISO 834, 800 °C	(t) ISO 834, 800 °C
(u) ISO 834, 800 °C			

4.2 Temperature-dependent properties of Eibenstock granite

4.2.1 Sample preparation and test methods

Mechanical and physical properties of EG were determined at room temperature (25 °C) after slow heating process with a heating rate of 5 °C/min.

According to the ISRM recommendations, cylindrical samples (50 mm diameter and 110 mm length) were prepared for determination UCS, Young's modulus, density and porosity. Brazilian discs with a nominal diameter of 50 mm and a thickness of 25 mm are used to determine the indirect tensile strength of granite which experienced different elevated temperatures. In addition to the specimens investigated at room temperature, cylindrical granite specimens were heated-up to 400 °C, 600 °C, 800 °C and 1000 °C with a heating rate of 5 °C/min. The specimens are kept at target temperatures for 36 hours to guarantee homogeneous temperature distribution and deformation equilibrium. Subsequently, specimens are cooled down to room temperature at a rate of 1 °C/min. The heating scheme applied for the Brazilian tests is the same as for the cylindrical specimens. Uniaxial tests were performed at room temperature after heat treatment and cooling down to room temperature. The specimens were uniaxial compressed with a rate of 0.1 mm/min. The Brazilian discs were compressed with 0.05 mm/min to obtain the tensile strength of the granite specimen experienced elevated temperatures according to Eq. (4-1).

The temperature-dependent bulk density ρ is measured by determination of volume V (i.e. diameter D and length L) and mass M of the cylindrical specimens at room temperature after the temperature treatment according to Eq. 4-3:

$$\rho = \frac{M}{V} = \frac{4M}{\pi D^2 L} \qquad (4\text{-}3)$$

To investigate the evolution of the failure process induced by the heating treatments, P-wave velocity and open porosity of the fresh and thermal damaged granite samples were measured. For P-wave velocity measurement two piezo-electric sensors are used as source and receiver, respectively. The sensors are centrally located at the top and bottom end surface of the sample. P-wave velocity is calculated by dividing distance by travel time of the primary ultrasonic impulse.

The open porosity Φ_0 is determined using the procedure defined by DIN EN 1936 (2007), according to Eq. 4-4:

$$\Phi_0 = (m_s - m_d)/(m_s - m_h) \times 100 \tag{4-4}$$

where m_s is the water-saturated mass, m_h is the mass suspended in water, and m_d is the oven-dry mass.

4.2.2 Density

Table 4-3 documents dimension and mass variations of granite samples. Based on the data, Figure 4-10a shows the density development with rising temperature. The average density of EG at room temperature is 2.60 g/cm^3. The density decreases slightly to 2.58 g/cm^3 at 400 °C, and to 2.54 g/cm^3 at 600 °C. An obvious decrease happens at 1000 °C where the density drops to 2.20 g/cm^3 due to the significant increase in specimen volume (see Figure 4-10b). Compared with the volume change, the mass change is very small (see Figure 4-10b) and can mainly be attributed to the loss of chemically bonded water.

Table 4-3 Dimension and mass of granite which experienced different temperatures

T [°C]	Data at 25 °C				Data after experienced target temperature			
	Diameter [mm]	Height [mm]	Volume [cm^3]	Mass [g]	Diameter [mm]	Height [mm]	Volume [cm^3]	Mass [g]
	49.63	109.81	212.43	553.11	49.67	109.92	212.99	550.11
400	49.68	109.69	212.63	553.60	49.73	109.77	213.21	550.38
	49.67	109.46	212.09	552.60	49.71	109.54	212.59	549.59
	49.67	109.04	211.28	550.78	49.95	109.69	214.95	545.98
600	49.68	108.75	210.80	549.35	49.95	109.39	214.36	544.57
	49.69	109.67	212.67	553.73	49.96	110.37	216.36	548.77
	49.65	109.62	212.24	552.26	52.38	115.53	248.95	546.77
1000	49.69	109.94	213.20	555.32	52.2	115.91	248.06	545.66
	49.65	109.84	212.67	552.72	52.21	115.64	247.57	545.65

(a) Density (b) Normalized volume and mass
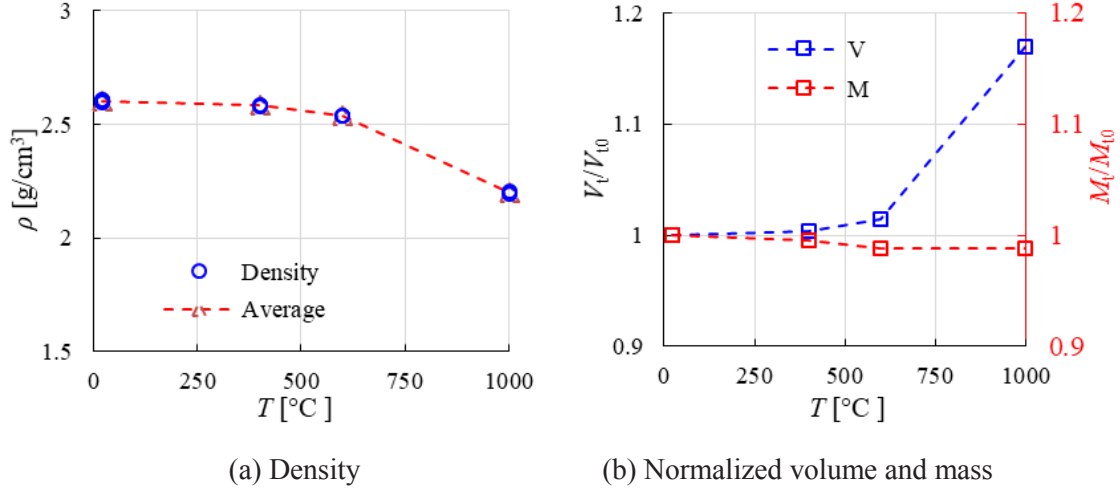
Figure 4-10 Volume and mass variations of samples experienced different temperatures. V_t and M_t are volume and mass after heating, while V_{t0} and M_{t0} correspond to room temperature before heating

4.2.3 P-wave velocity and open porosity

The evolution of P-wave velocity (V_p) for samples at different temperatures is shown in Figure 4-11. It can be seen that the P-wave velocity decreases with temperature rising, especially for 600 °C the velocity shows the most significant reduction. From room temperature to 400 °C, the velocity reduces from 4263 m/s to 2914 m/s; then it drops to 1355 m/s at 600 °C and continuously decreases to only 526 m/s at 1000 °C. The open porosity is also plotted in Figure 4-11. Up to 600 °C, the open porosity shows an opposite trend with P-wave velocity. However, the porosity increase is most significant in the temperature range between 600 °C to 1000 °C, while the P-wave velocity reduction is not so pronounced in this temperature range (see Figure 4-11). The P-wave velocity is affected by the total material damage, while the open porosity can only reflect the network of connected cracks. Therefore, we can deduce that while below 600 °C primarily new, but isolated cracks develop, these cracks connect at temperatures above 600 °C and generation of new cracks is decelerating.

4.2.4 UCS and peak axial strain

The uniaxial compression test results are plotted in Figure 4-12 and documented in Table 4-4. Axial peak stress σ_c and corresponding strain ε_c as function of temperature are shown in Figure 4-12b.

UCS experiences a slight increase up to about 400 °C and then decreases gradually up to 1000 °C, while the peak axial strain shows a continuous increase. The stress-strain curves show gradual nonlinear behavior from 400 °C to 1000 °C before reaching peak stress. The samples at 800 °C and 1000 °C display obviously ductile behavior, which is characterized by gradual loss of strength with ongoing deformation in the post-peak-phase (strain softening) while brittle failure leads to violent rupture for samples experienced temperatures up to about 600 °C.
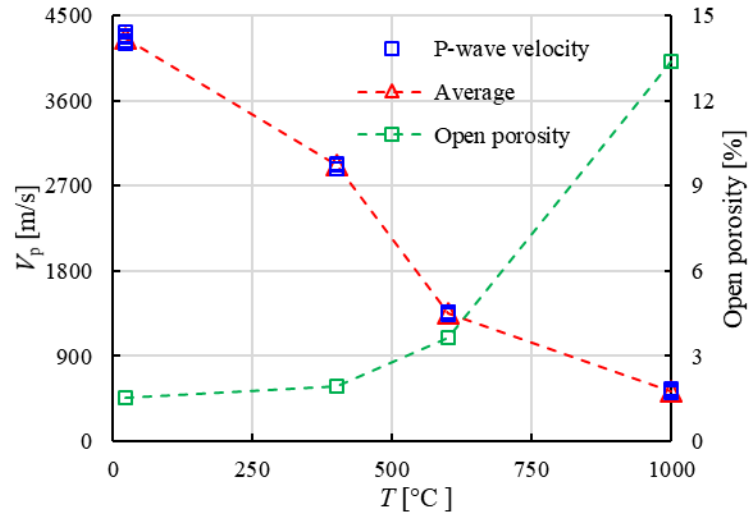
Figure 4-11 Temperature-dependent P-wave velocity and open porosity
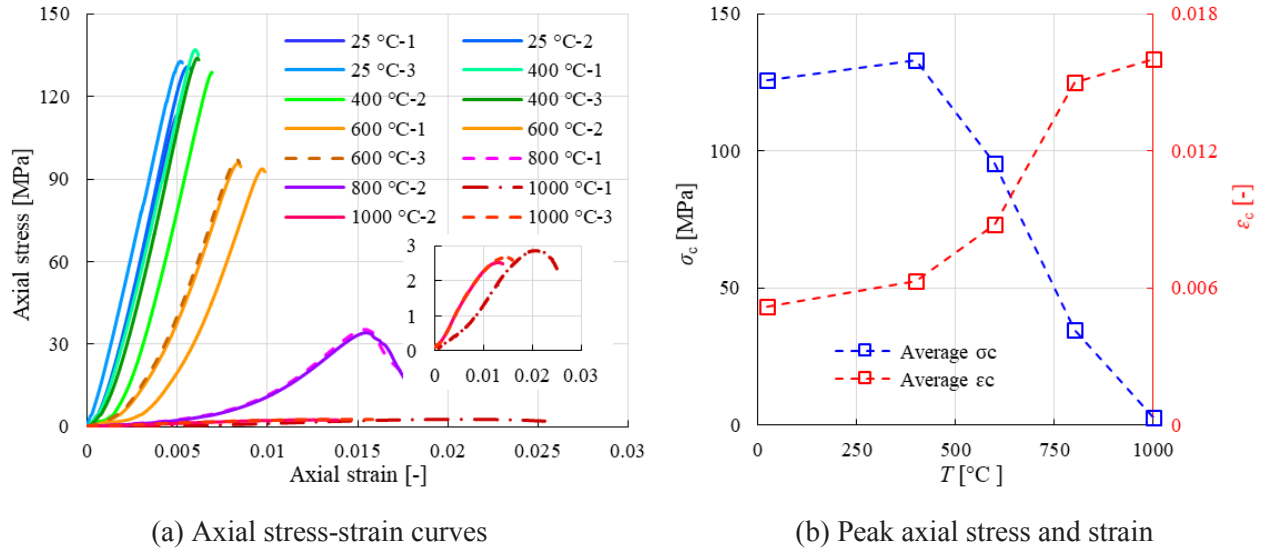
(a) Axial stress-strain curves

(b) Peak axial stress and strain

Figure 4-12 Uniaxial compression test results of granite after heat treatment

51

Table 4-4 Uniaxial compression test results of granites experienced different temperatures

T [°C]	σ_c [MPa]	Average σ_c [MPa]	ε_c [-]	Average ε_c [-]
	113.37		0.0050	
25	130.83	125.66	0.0056	0.0052
	132.78		0.0052	
	137.05		0.0060	
400	128.78	133.26	0.0069	0.0063
	133.96		0.0061	
	93.69		0.0097	
600	95.74	95.47	0.0084	0.0088
	96.98		0.0083	
	35.33		0.0154	
800	34.20	34.76	0.0154	0.015
	2.86		0.0201	
1000	2.53	2.68	0.0125	0.016
	2.66		0.0143	

4.2.5 Elastic modulus

The stiffness of the granite can be represented by the threshold Young's modulus E_c, which is defined by $E_c = \sigma_c/\varepsilon_c$ (see Table 4-5). The often used tangent Young's modulus E_t, which is measured at a stress level equal to 50% of UCS (ISRM 1979), is also calculated. Figure 4-13 shows E_c and E_t of granite after heat treatments. Although the general trend of both, E_c and E_t is decreasing with increasing temperature, there are differences in magnitude. E_t increases slightly at 400 °C before it decreases to a much lower level at 1000 °C, while E_c shows a continuous decrease. The maximum difference between E_c and E_t reaches 6.6 GPa at 400 °C.

4.2.6 Tensile strength

Brazilian test results are documented in Table 4-6 and Figure 4-14. It shows a decrease at elevated temperatures with a reduction of nearly 25% at 400 °C compared with samples not heated. Tensile capacity of the granite nearly vanishes after a temperature treatment up to 1000 °C.

Table 4-5 Calculated Young's modulus of granite at different temperatures

T [°C]	E_c [GPa]	E_t [GPa]
25	23.96	27.38
400	21.16	27.73
600	10.93	17.39
800	2.26	4.50
1000	0.18	0.34

Table 4-6 Brazilian test results of granite experienced different temperatures

T [°C]	σ_t [MPa]	Average [MPa]
	7.19	
25	7.27	7.77
	8.85	
	5.36	
400	5.24	5.81
	6.84	
	3.82	
600	2.81	3.27
	3.20	
	0.27	
1000	0.075	0.19
	0.23	

Figure 4-13 Elastic modules of granite after heat treatment
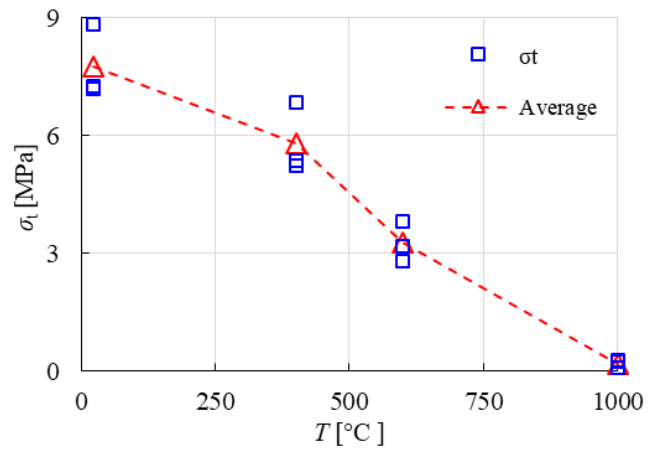
Figure 4-14 Tensile strength of granite after heat treatment

5 Pre-study: numerical modelling of thermal induced cracking of granite

The continuum based Finite Difference code FLAC^{3D} is used in this study. The thermal option of FLAC^{3D} incorporates conduction models for thermal analysis. The mechanical models combined with the isotropic conduction model allow the simulation of thermal induced strains and stresses (i.e. thermo-mechanical coupling). Several versions of the well-known Mohr-Coulomb constitutive model with tension cut-off were extended by the established thermo-mechanical parameter relations described in section 2.2 to investigate the potential of realistic simulation of thermal induced damage. A new constitutive law for thermal cracking of granite is developed based on the general property variations, which aims to build a model suitable for most granites. The obtained new constitutive law is validated on uniaxial compression tests on granite samples after being exposed to high temperatures up to 800 °C. The proposed numerical model is able to duplicate the thermal induced cracking which results in reduced peak strength, pronounced softening and transition from brittle to ductile behavior. Comparison with lab tests in respect to thermal induced fracture pattern and stress-strain relations shows remarkable agreement.

5.1 Influence of property distributions and constitutive law

5.1.1 Model description

The basic expression based on the energy balance has the following form:

$$-q_{i,i} + q_v = \rho C_v \frac{\partial T}{\partial t} \tag{5-1}$$

where q_i [W/m^2] is the heat-flux vector, q_v [W/m^3] is the volumetric heat-source intensity, C_v [J/kg°C] is the specific heat at constant volume, and ρ [kg/m^3] is the mass density. The thermal conduction in the model is governed by Fourier's law, which equals to the product of thermal conductivity k [W/m°C] and the temperature gradient, $-\nabla T$ [°C/m]. The heat transfer law has the form:

$$q_i = -k\nabla T \tag{5-2}$$

Solution of thermal-stress problems requires reformulation of the incremental stress-strain relations, which is accomplished by subtracting the portion due to temperature change from the total strain increment. Thermal stress and strain changes are given by the following expressions:

$$\Delta\sigma_{ij} = 3\delta_{ij}K\alpha_t\Delta T \tag{5-3}$$

$$\Delta\varepsilon_{ij} = \delta_{ij}\alpha_t\Delta T \tag{5-4}$$

where α_t [1/°C] is the coefficient of thermal expansion, ΔT is the temperature increment, K is the bulk modulus [Pa] and δ_{ij} is the Kronecker delta.

Previous thermo-mechanical models are homogeneous, which means the physical and thermo-mechanical properties of each element in the model have the same value. This might be an efficient way for large scale applications, but for considerations at a smaller scale (e.g. at the grain size level) the heterogeneity of physical and thermo-mechanical properties may become important. To reflect such an inhomogeneity, the Weibull statistical distribution is applied for the thermo-mechanical parameters. The cumulative distribution function (CDF) and probability density function (PDF) are given by the three-parameter Weibull distribution (Weibull 1951; Liu et al. 2004):

$$F(x) = 1 - \exp\left[-\left(\frac{x - x_u}{x_0}\right)^m\right] \tag{5-5}$$

$$f(x) = \frac{dF}{dx} = \frac{m}{x_0}\left(\frac{x - x_u}{x_0}\right)^{m-1}\exp\left[-\left(\frac{x - x_u}{x_0}\right)^m\right] \tag{5-6}$$

where x ($x \geq 0$) is the Weibull distributed random variable, x_u is the threshold value of x or location parameter, m is the shape parameter (also called homogeneity index) describing the scatter of x, and x_0 is the scale parameter which is related to the mathematical expectation. Frequently, x_u can be set to zero (Vales and Rezakhanlou 1999; Liu et al. 2004), yielding the two-parameter Weibull distribution. CDF, PDF, mean $E(x)$, and variance $Var(x)$ are given by:

$$F(x) = 1 - \exp\left[-\left(\frac{x}{x_0}\right)^m\right] \tag{5-7}$$

$$f(x) = \frac{m}{x_0}\left(\frac{x}{x_0}\right)^{m-1}\exp\left[-\left(\frac{x}{x_0}\right)^m\right] \tag{5-8}$$

$$E(x) = \int_0^\infty xf(x)dx = x_0\Gamma(1+\frac{1}{m})$$ (5-9)

$$Var(x) = E(x^2) - (E(x))^2 = x_0^2\left[\Gamma(1+\frac{2}{m}) - \Gamma^2(1+\frac{1}{m})\right]$$ (5-10)

where Γ is the Gamma function.

The Weibull random variable x, which is essential to be used for property distributions, cannot be calculated directly from the equations above. This can be solved with the inverse function of the two-parameter Weibull distribution. $F(x)$ describes the probability of a random variable taking a value less than or equal to x. It has the property of $0 \leq F(x) \leq 1$, which can be presented by random numbers u within the interval $[0,1]$ (i.e. $F(x) = u$). u can be created through a universal random number generator. Subsequently we can obtain the Weibull distributed random variable: $x = F^{-1}(u)$. If the basic property of the sample is P_0, the specific property of the numerical element i is P_i, and the corresponding Weibull random variable is x_i, then we obtain the randomly distributed property $P_i = P_0 \times x_i$. The expressions of x and x_0 can thus be expressed as:

$$x = x_0[-\ln(1-u)]^{1/m}$$ (5-11)

$$x_0 = \frac{E(x)}{\Gamma(1+1/m)}$$ (5-12)

The shape parameter m describes the variation of the element property, it plays an important role for the thermo-mechanical behavior. Many studies have been conducted on estimating the Weibull parameters for better representing the reliability of materials. To estimate the Weibull parameters, many methods like the least-square (LS) method, the maximum likelihood (ML) method, and method of moments (Davies 2001; Deng and Jiang 2017) have been used. Each method has one or more shortcomings like invalid assumptions, lack of physical meaning, difficulty of use or accuracy relies on a large number of data (Davies 2001). The Weibull distribution with estimated parameters can be used to characterize the scatter in strength and enables us to know the probability of failure for a certain load. All these methods are based on macroscale properties of the sample to obtain the Weibull parameters, and they are not suitable for property distributions at the element scale. Tan (2013) has pointed out that statistical parameters for element properties of the sample should be determined by investigations at the mineral scale. This is extremely complicated in lab tests, and

previous researchers generally implemented statistical distributions of properties without considering the different mineral proportions in a quantitative way.

Liu et al. (2004) suggests that the scale parameter x_0 can be treated as mean value of a property as it is approximately the mean value of the Weibull distribution $E(x)$. In this study, we set the mean of Weibull random variables $E(x) = 1$, assuming that the mean value of the property of all elements is expected to be the macro property of specimen P_0. Then the scale parameter will become:

$$x_0 = \frac{1}{\Gamma(1+1/m)} \qquad (5\text{-}13)$$

$$Var(x) = \left[\frac{1}{\Gamma(1+1/m)}\right]^2 \left[\Gamma(1+\frac{2}{m}) - \Gamma^2(1+\frac{1}{m})\right] \qquad (5\text{-}14)$$

According to the above equation, the shape parameter m can greatly influence the variance of random variables, especially when m is less than 4 (see Figure 5-1a). The scatter characteristics of the rocks is indicated by different m. Figure 5-1b shows the PDFs of the Weibull distributions with $E(x) = 1$. The possibility of generating small divergence will increase with the increase of the shape parameter m.

(a) Weibull variance vs. shape parameter　　　(b) Probability density
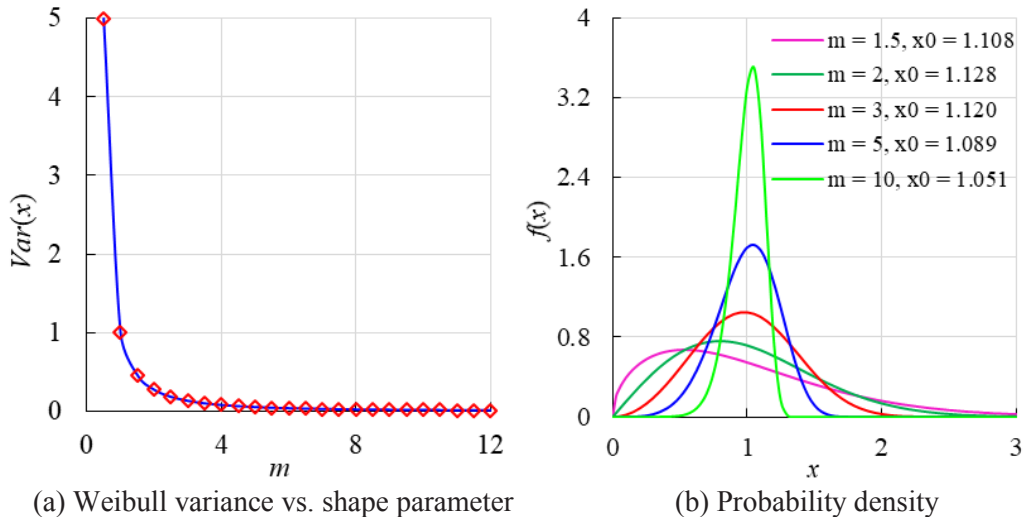
Figure 5-1 Weibull distributions

A cylindrical granite specimen with 50 mm in diameter and 100 mm in length was modelled as shown in Figure 5-2a. Because sample geometry and boundary conditions are completely

symmetric, only one quarter was simulated, taken into account that this is not absolutely correct in case that random distribution of parameters is assumed. The outer boundary temperature was fixed to the desired value. Displacements at the two perpendicular symmetry planes and the bottom were fixed in normal direction (Figure 5-2b). For this preliminary study, a relatively coarse mesh with 1152 zones was used. Table 5-1 shows the initial thermo-mechanical granite properties at room temperature. All the parameters in numerical models were temperature-independent in this section. All the models were heated for 5 s with a temperature of 150 °C at the outer boundary (Wang and Konietzky 2019).
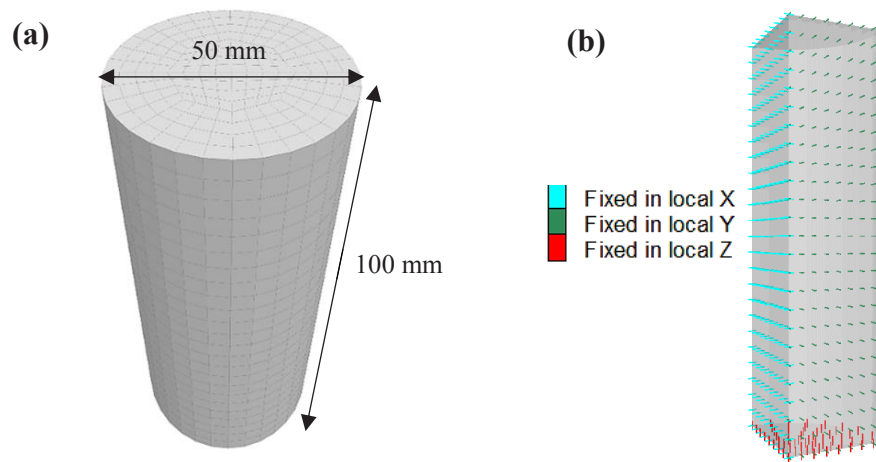
Figure 5-2 Schematic diagram of the granite model

Table 5-1 Model parameters

Parameters	Initial Values
Coefficient of linear thermal expansion α_t [1/°C]	8×10^{-6}
Specific heat C_v [J/kg°C]	820
Thermal conductivity k [W/m°C]	2.6
Young's Modulus E [GPa]	37.35
Poisson's ratio v	0.127
Tensile Strength σ_t [MPa]	13
Cohesion c [MPa]	23
Friction angle φ [°]	50
Dilation angle ψ [°]	10
Density ρ [kg/m³]	2645

Besides the classical Mohr-Coulomb model with tension cut-off, the Strain-Softening model is also used. The advantage of this law is that cohesion, friction, dilation and tensile strength can soften

or harden after the onset of plastic yield. The softening table relating tension limit to plastic tensile strain and tables relating shear parameters (cohesion, friction angle, and dilation angle) to plastic shear strains are the same as in section 5.2.3, where these parameters are back-calculated from lab test results. In summary, four approaches (Table 5-2) were applied. In Weibull models, the shape parameter m characterizes the brittleness (high values for m lead to more brittle behavior and vice versa). Tan (2013) tested different shape parameters ($m = 5$ to 40) to simulate heterogeneous granite samples and found that it is extremely complicated to determine an accurate shape parameter. In these models, we set the shape parameter $m = 10$ and the scale parameter $x_0 = 1.05$.

Table 5-2 Model approaches

Model	Constitutive law	Property distribution
1	Mohr-Coulomb	Homogeneous
2	Mohr-Coulomb	Weibull distribution
3	Strain-Softening	Homogenous
4	Strain-Softening	Weibull distribution

5.1.2 Temperature distribution

Homogeneous and heterogeneous model show slightly different temperature distribution patterns (Figure 5-3). Figure 5-3c shows that the biggest temperature difference between these two models is 0.86 °C. Figure 5-4 shows distributions of density, thermal conductivity and specific heat in the model. These heterogeneous properties can influence the heat convention, and consequently lead to changes in temperature gradient.

5.1.3 Thermal induced damage

Figure 5-5 shows that only tensile failure occurs in the homogeneous model, while inside the heterogeneous model in addition also some shear failures can be observed. Another difference is that the outer surface of the homogenous model is undamaged except for the top and bottom. Lab tests and numerical simulations have shown that thermal induced cracks are usually isolated and spread over the whole sample (Zhao 2016; Yang et al. 2017). In general, the failure pattern of the heterogeneous model is more realistic. It reproduces the general trend superimposed by some local fluctuations.

Figure 5-6 shows the plasticity states of Mohr-Coulomb and Strain-Softening model with heterogeneous property distributions (i.e. Model 2 and Model 4 respectively). The failure pattern of Strain-Softening model (Figure 5-6b) is similar to that of the Mohr-Coulomb model, but tends to produce more isolated cracks compared with the more connected failure zones shown in Figure 5-6a. Also, compared with the Mohr–Coulomb model, in general the strain-softening model can reflect the strength reduction and the post-failure behavior of the sample in a more realistic way.

(a) Homogeneous   (b) Heterogeneous   (c) Temperature distribution along scanlines
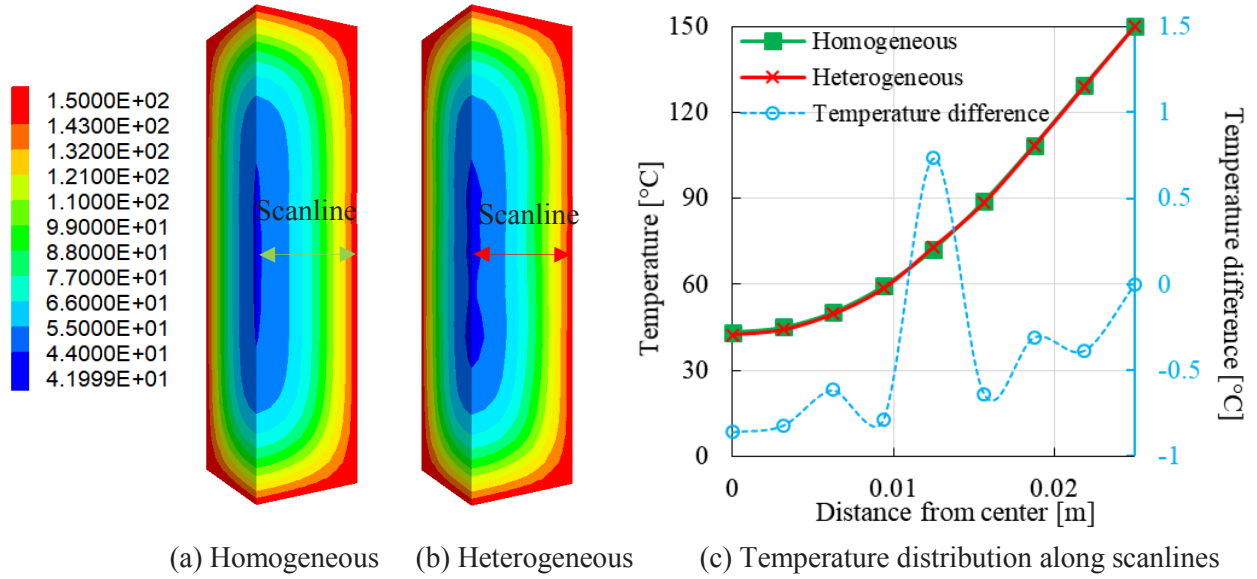
Figure 5-3 Temperature distributions [°C] of different models heated for 50 s with 150 °C at outer boundary

(a) Density [kg/m³]   (b) Thermal conductivity [W/m°C]   (c) Specific heat [J/kg°C]
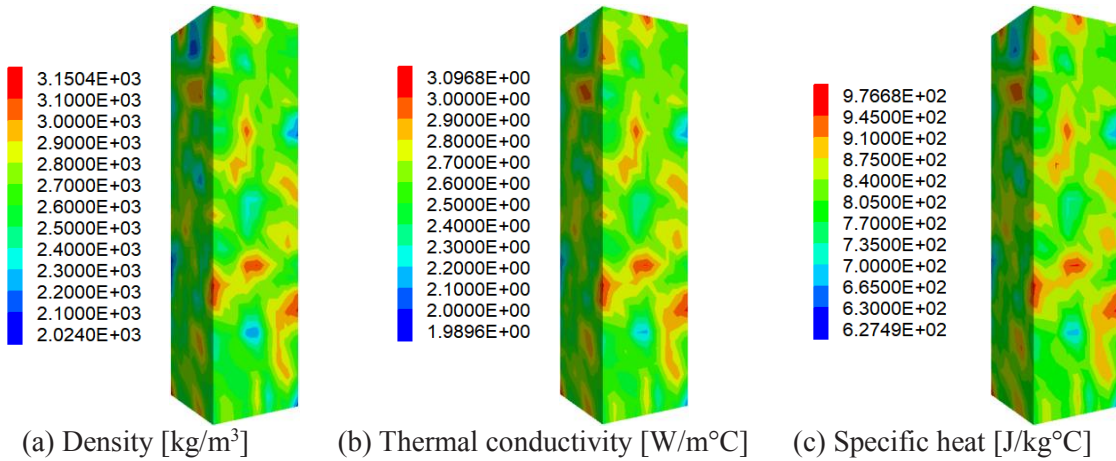
Figure 5-4 Property distributions of the sample heated for 50 s with 150 °C at outer boundary

61

(a) Homogeneous   (b) Heterogeneous
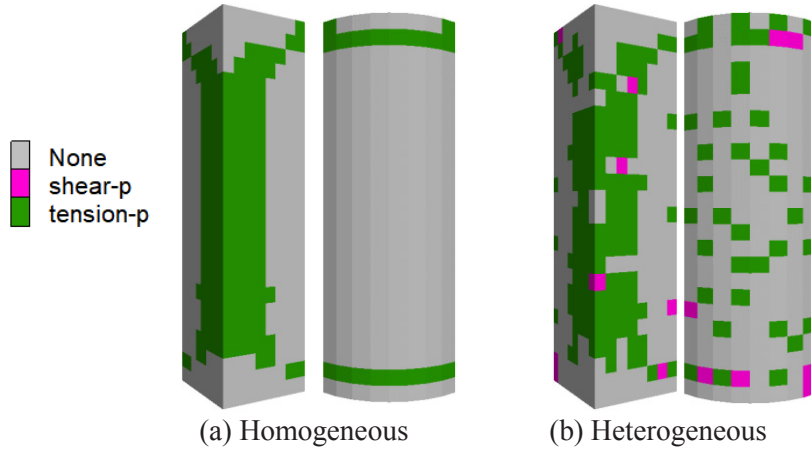
Figure 5-5 Failure states for model 1 and 2 heated for 50 s with 150 °C at outer boundary

(a) Mohr-Coulomb   (b) Strain-Softening
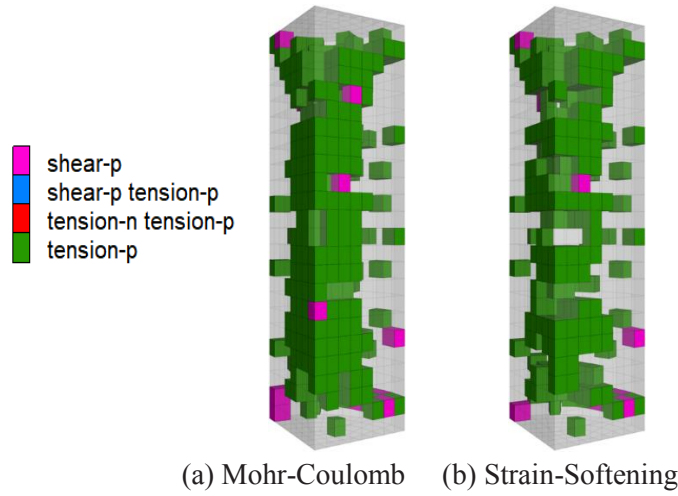
Figure 5-6 Plasticity states of different models heated for 50 s with 150 °C at outer boundary

5.2 Influence of temperature-dependent properties

5.2.1 Model description

The geometrical model for studying the influence of temperature-dependent properties (i.e. sensitivity analysis) is the same as shown in Figure 5-2. Table 5-3 shows the parameters used in the model. All the models use the same set of softening tables mentioned in section 5.2.3. In these models, Weibull functions with the shape parameter $m = 10$ and the scale parameter $x_0 = 1.05$ are used for property distributions. The simulations assume temperature-dependent variations of mechanical and thermal properties via the corresponding trend curves given in section 2.2. For each boundary condition, a reference model was built where all the 8 parameters are temperature-

independent. Except for the parameters to be investigated, all other input parameters are the same as in the reference model. The results are shown in form of difference values related to the reference model.

The standard fire time-temperature curve given in ISO 834 is used for fire resistance test, and the temperature development is described by the following equation:

$$T = T_0 + 345 log\left(8t + 1\right) \tag{5-15}$$

where T_0 is room temperature, T is the fire temperature in °C, and t is time in minutes. According to the equation, the average heating rate is 35 °C/min to reach 800 °C starting from 25 °C. Two boundary conditions were considered: (i) fixed boundary temperature of 800 °C for 50 s and (ii) constant heating rate of 35 °C/min at the outer boundary until 800 °C has been reached.

Table 5-3 Parameters for sensitivity study (see also Table 2-1)

Parameters	Temperature-dependent values
Coefficient of linear thermal expansion α_t [1/°C]	$\alpha_t (T) = 8 \times 10^{-6} \times f_{\alpha t / \alpha t0}$
Specific heat C_v [J/kg°C]	$C_v (T) = 820 \times f_{Cv / Cv0}$
Thermal conductivity k [W/m°C]	$k (T) = 2.6 \times f_{k / k0}$
Young's modulus E [GPa]	$E (T) = 37.35 \times f_{E / E0}$
Poisson's ratio v	$v (T) = 0.127 \times f_{v / v0}$
Tensile strength σ_t [MPa]	$\sigma_t (T) = 13 \times f_{\sigma t / \sigma t0}$
Cohesive strength c]MPa]	$c (T) = 20 \times f_{ct / c0}$
Friction angle φ [°]	$\varphi (T) = 50 \times f_{\varphi t / \varphi 0}$
Dilation angle ψ [°]	10 (constant)
Density ρ [kg/m³]	2645 (constant)

5.2.2 Thermo-mechanical behavior with temperature-dependent parameters

5.2.2.1 Temperature distribution

Figure 5-7 shows the temperature variations along the scanline (see Figure 5-3) for a model heated for 50 s with a constant boundary temperature of 800 °C. All the values were processed by subtracting the data of the reference model. We can see that specific heat and thermal conductivity have obvious effects on temperature distribution. Whereas, thermal conductivity plays a more

important role than specific heat, causing the largest difference of 91.9 °C temperature decrease. Figure 5-8 shows the simulation results for the model heated up to 800 °C with a heating rate of 35 °C/min. Specific heat shows a more obvious influence under these conditions, but thermal conductivity still contributes most to the temperature variations. In the central area of the sample, the temperature-dependent properties lead to a temperature difference up to 91.2 °C.
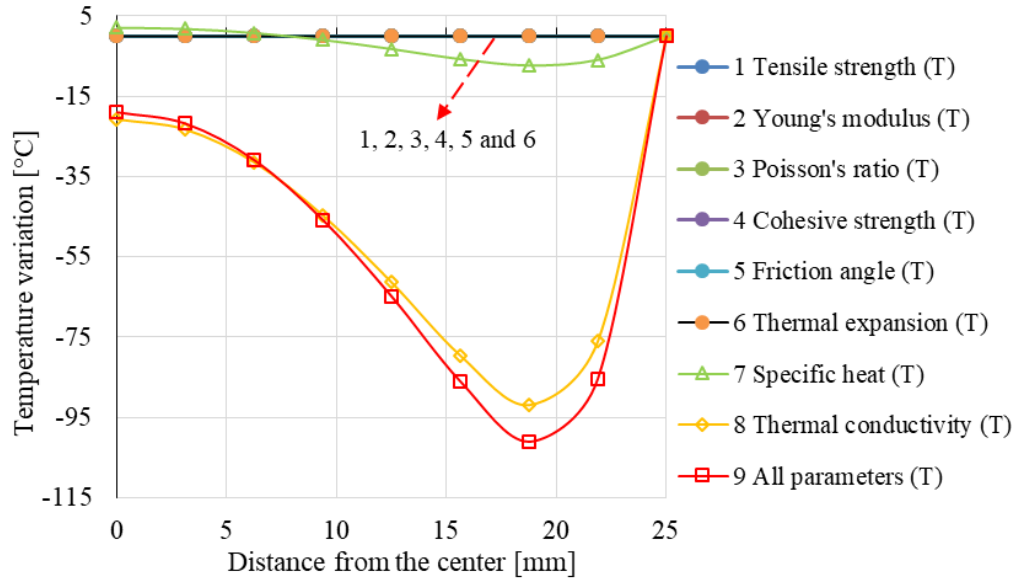
Figure 5-7 Temperature variations along the scanline for model with a constant boundary temperature of 800 °C exposed for 50 s considering different parameters.
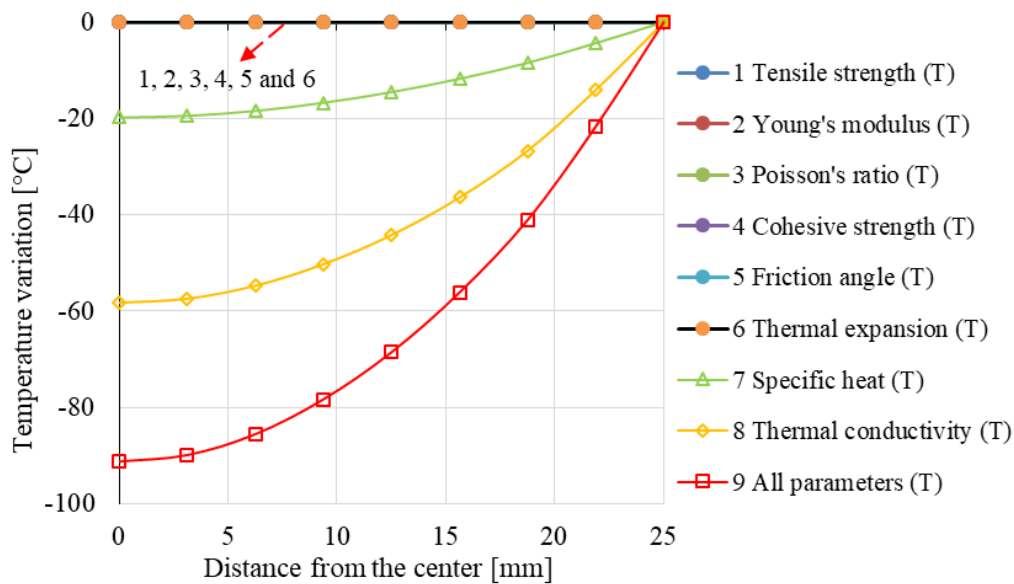
Figure 5-8 Temperature variations along the scanline for model with a heating rate of 35 °C/min reaching 800°C at the outer boundary considering different parameters

5.2.2.2 Thermal induced stresses

Figure 5-9 and Figure 5-10 show variations of principal stresses induced by temperature-dependent parameters under constant boundary temperature. Both, maximum and minimum principal stresses are strongly influenced by thermal expansion coefficient, thermal conductivity, Young's modulus, and tensile strength. All temperature-dependent parameters lead to a significant increase in the value of $\Delta\sigma = \sigma_1 - \sigma_3$ at the distance of 10.9 mm, and such kind of localized stresses will subsequently result in more isolated failures across the sample. Compared with the model of constant boundary temperature, thermal stresses in proximity to the outer boundary are sensitive to property variations for a heating rate of 35 °C/min (Figure 5-11 and Figure 5-12). This is because the heating rate results in a continuous temperature increase (i.e. thermal gradient) near the boundary, thus causing variations in thermal stresses. Another noticeable phenomenon is that cohesive strength becomes more important in the model with a constant heating rate. In both scenarios, the influence of friction angle, specific heat, and Poisson's ratio on stress changes is relatively small. Especially the impact of friction angle can be ignored compared with other parameters. Nevertheless, thermal expansion coefficient, thermal conductivity, tensile strength, and Young's modulus always have significant influence on thermal stress evolution.
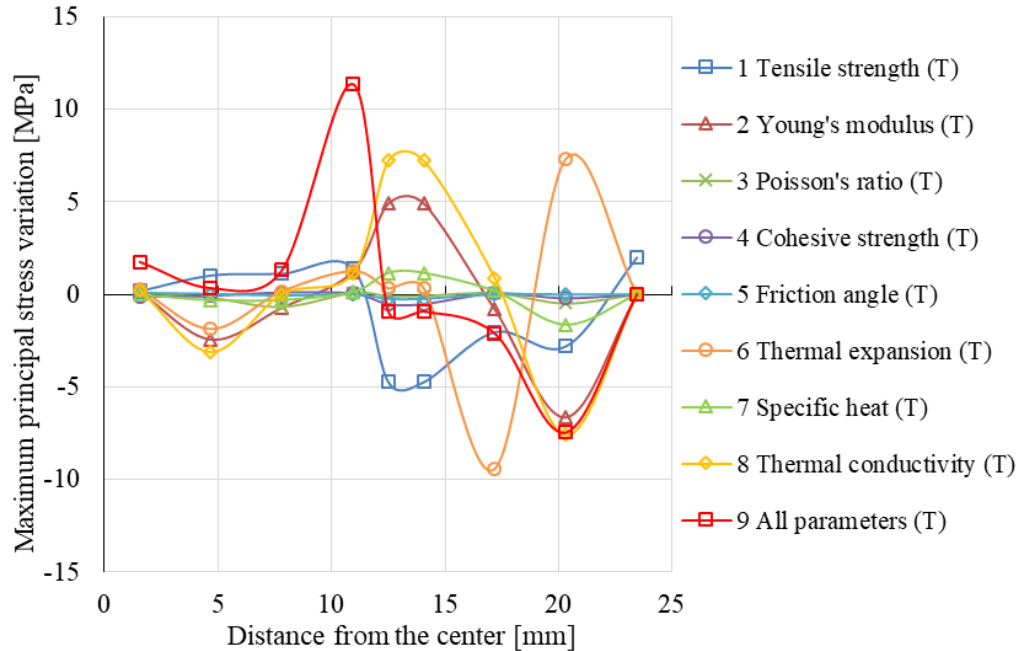
Figure 5-9 Maximum principal stress σ_1 variations along scanline for model with a constant boundary temperature of 800 °C considering different parameters

65
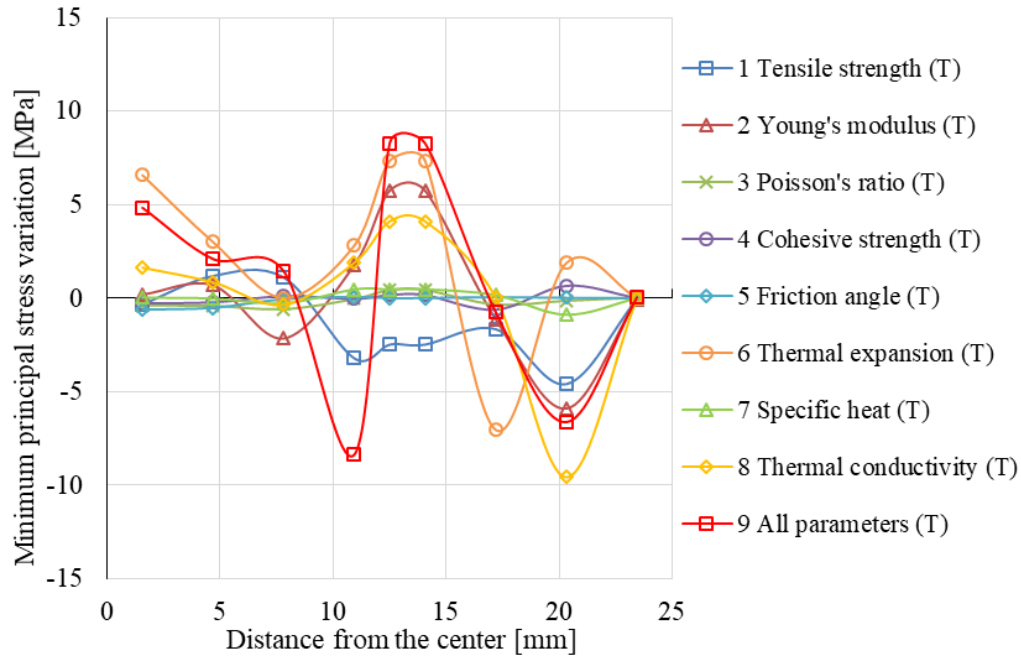
Figure 5-10 Minimum principal stress σ_3 variations along scanline for model with a constant boundary temperature of 800 °C considering different parameters
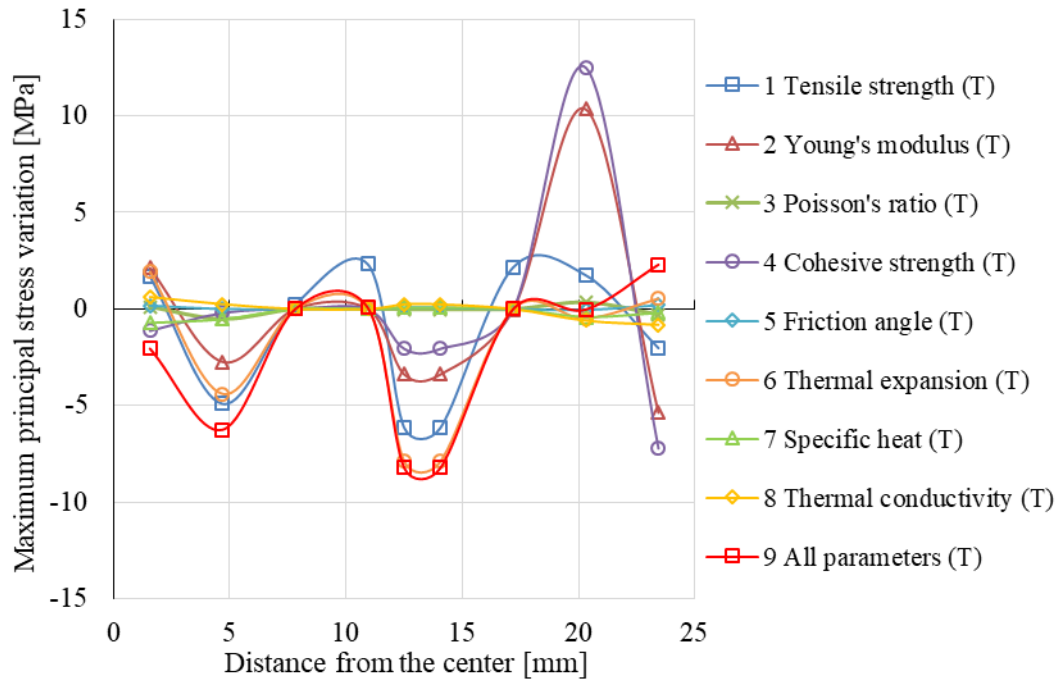
Figure 5-11 Maximum principal stress σ_1 variations along scanline for model with a heating rate of 35 °C/min considering different parameters
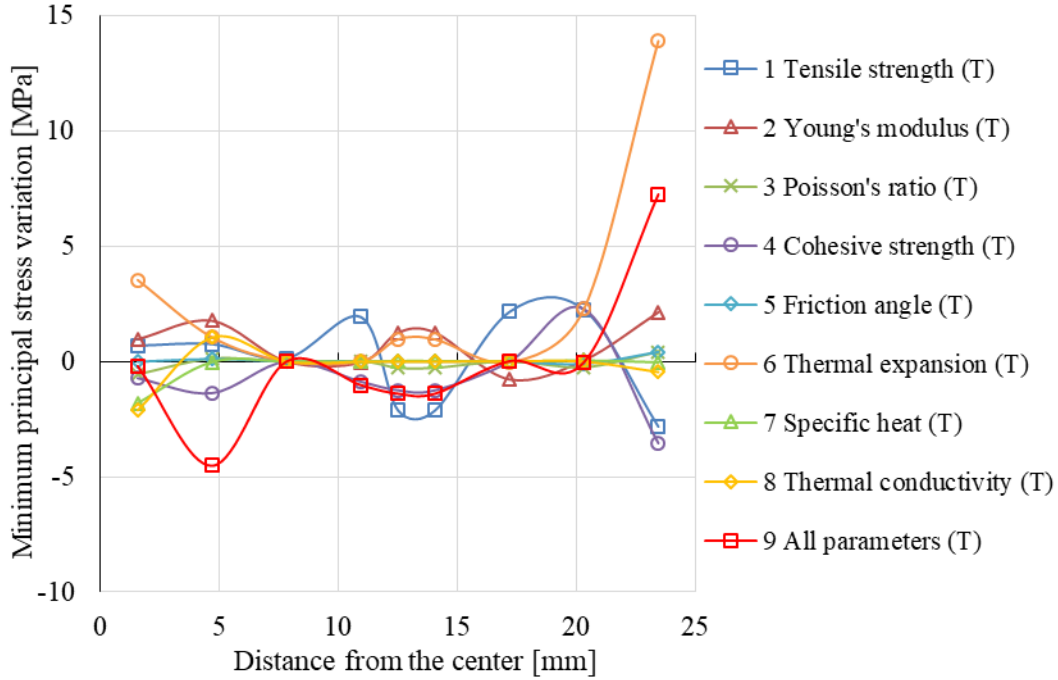
Figure 5-12 Minimum principal stress σ_3 variations along scanline for model with a heating rate of 35 °C/min considering different parameters

5.2.2.3 Thermal induced deformations

Total displacements, i.e. displacement magnitudes of grid points, are greatly influenced by thermal expansion coefficient, Young's modulus, and thermal conductivity under constant boundary temperature scenario (Figure 5-13). Obviously, thermal expansion coefficient contributes most, while thermal conductivity leads to a slightly opposite behavior. The reason is that thermal expansion coefficient increases strongly with increasing temperature, while thermal conductivity has an opposite trend which results in a decrease of temperature increment. Consequently, the displacement is reduced according to Eq. (5-4).

The variations of properties under constant boundary temperature also induce the expansion and contraction of granite as shown in Figure 5-14. The minimum stress variation (Figure 5-10) has shown that when all parameters are temperature-dependent, there is a big increase in compressive stress at a distance of 10.9 mm. This is why the volumetric strain increment of the grain becomes negative (i.e. contraction). As expected, largest grain expansion takes place at the boundary.
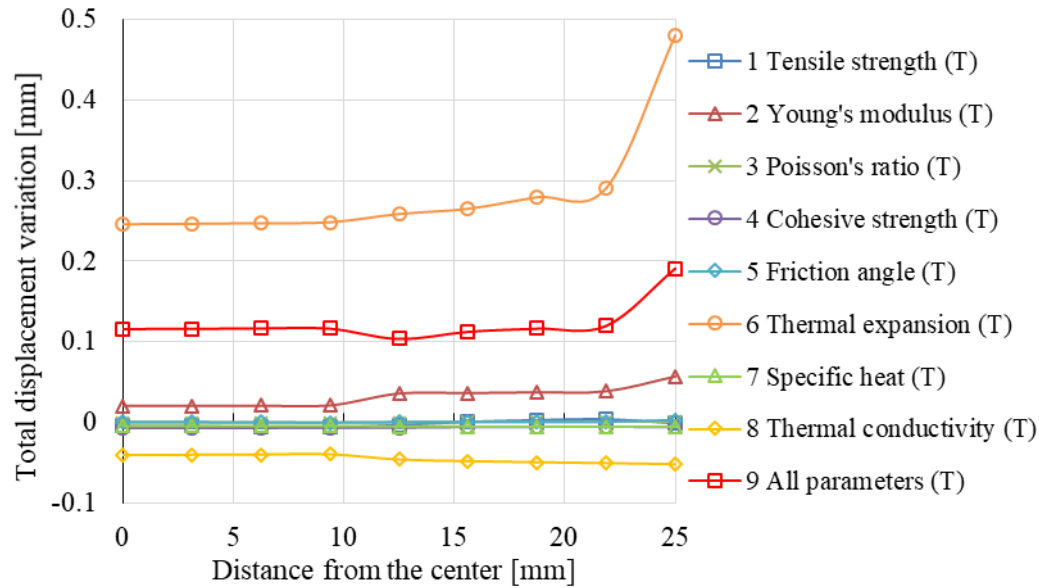
Figure 5-13 Total displacement variations along scanline for model with a constant boundary temperature of 800 °C considering different parameters
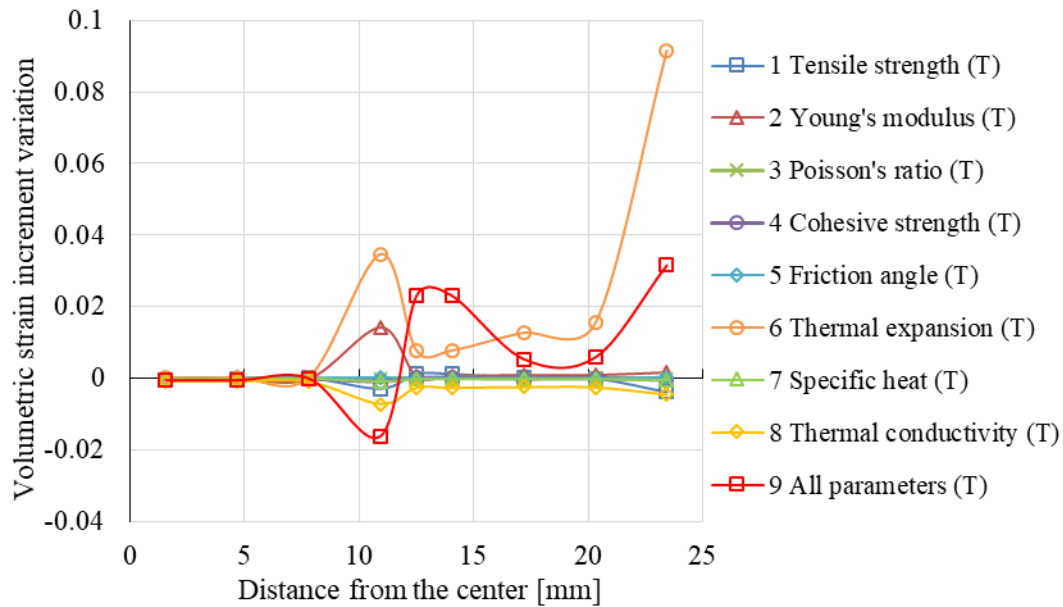
Figure 5-14 Volumetric strain increments along scanline for model with a constant boundary temperature of 800 °C considering different parameters

In the second scenario with a heating rate of 35 °C/min (Figure 5-15), the linear thermal expansion coefficient dominates the displacement again. Other temperature-dependent parameters have only insignificant influence. Figure 5-16 shows the volumetric strain variations for a heating rate of 35 °C/min. Again, thermal expansion coefficient determines the dilatation of the granite.
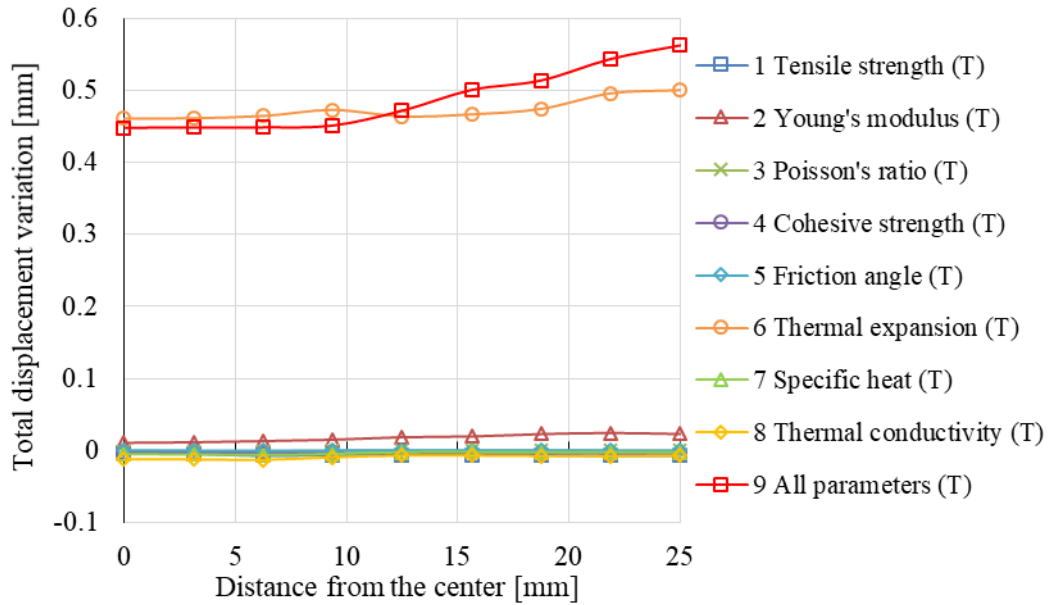
Figure 5-15 Total displacements along scanline for model with a heating rate of 35 °C/min considering different parameters
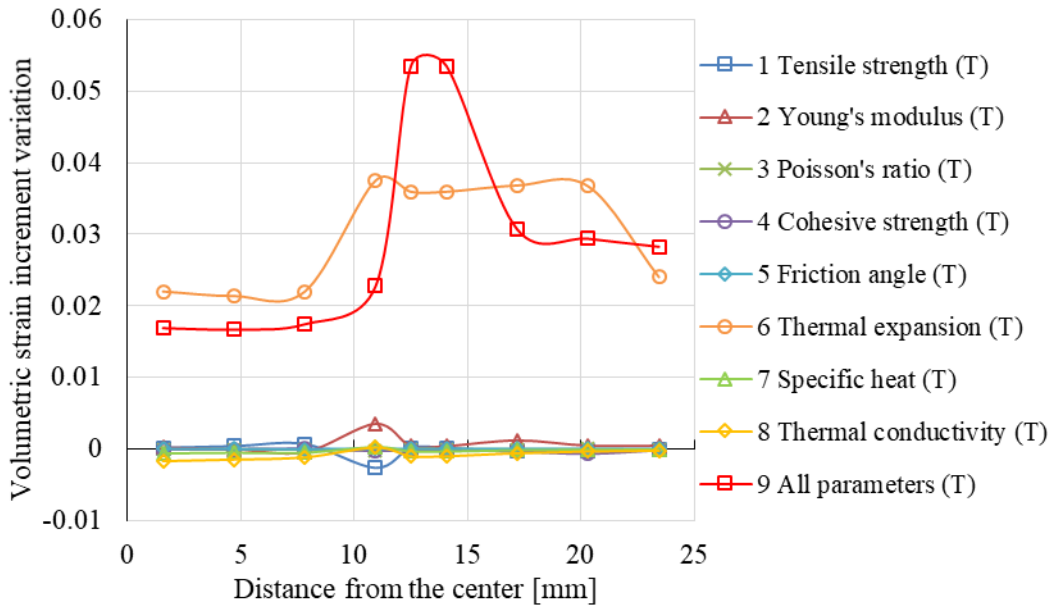
Figure 5-16 Volumetric strain increments along scanline for model with a heating rate of 35 °C/min considering different parameters

5.2.3 Validation of the modelling strategy

5.2.3.1 Model description

Based on an evaluation of the modelling strategy described above, the basic idea of the proposed constitutive model is illustrated in Figure 5-17. A quarter of a three-dimensional model with finer mesh of 6500 elements was set up with a radius of 25 mm and a height of 100 mm. All parameters are assigned according to a Weibull distribution with the shape parameter $m = 15$ and the scale parameter $x_0 = 1.036$. The geometrical boundary is fixed as shown in Figure 5-2. The model was heated with a rate of 5 °C/min and then kept at target temperatures for 30 minutes to achieve nearly homogeneous final temperature distribution.
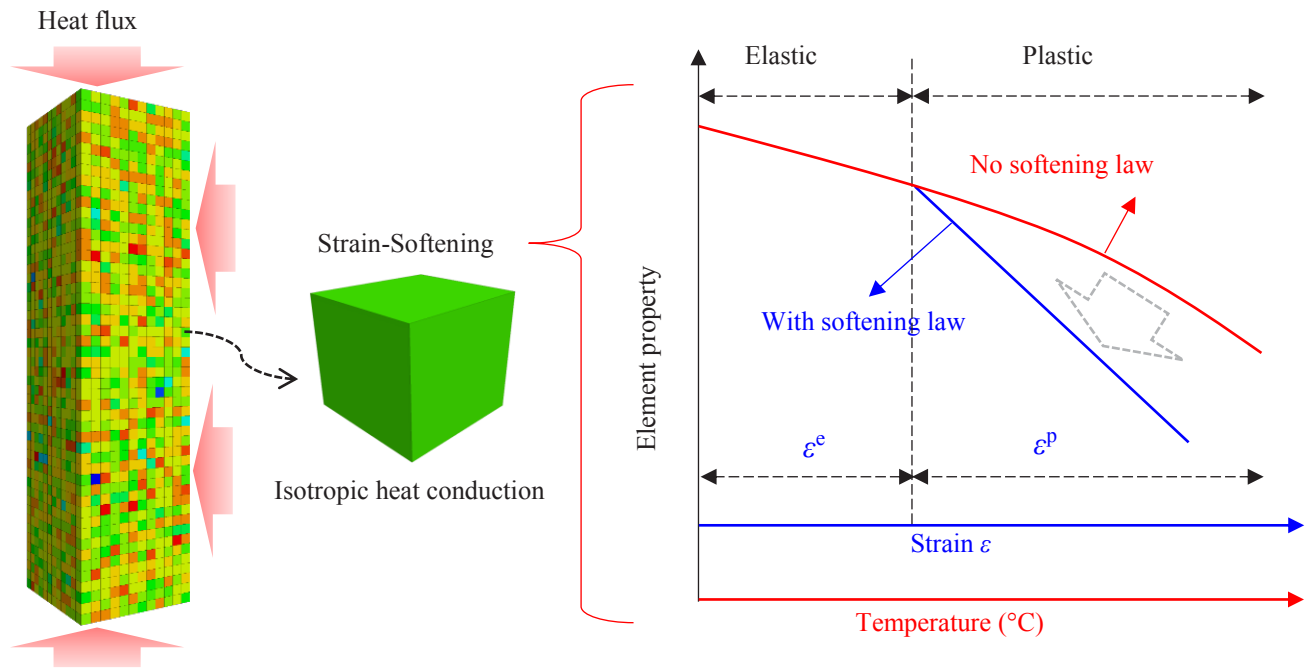
Figure 5-17 Sketch of the established model for thermo-mechanical simulation. ε^e is the elastic strain, ε^p is the plastic strain

Figure 5-18 shows the axial stress-strain curves for uniaxial loaded granite specimens after thermal treatments. It is conspicuous that the behavior changes dramatically beyond 600 °C. Below 600 °C a smooth transition from brittle to slightly ductile behavior can be observed. Zuo et al. (2017) suggested that 250 °C could be considered as a threshold for the brittle ductile transition for some granites. The noticeable nonlinearity and yielding phase before peak load indicates the loss of

brittle characteristic of granite. To characterize the stiffness of the sample, a threshold modulus E_c obtained from dividing peak axial stress σ_c by the peak axial strain ε_c is defined. The input Young's modulus E_{input}, which governs the elastic behavior before yielding can be back-analyzed based on E_c.
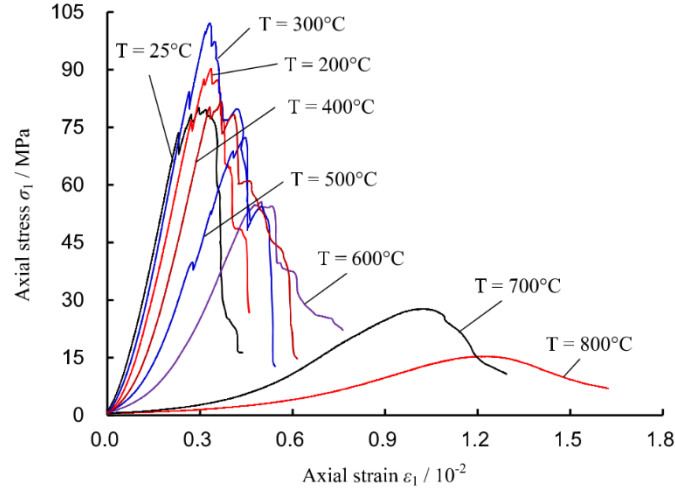
Figure 5-18 Axial stress-strain curves for uniaxial loaded granite specimens after thermal treatments (Yang et al. 2017)

Table 5-4 shows the input parameters used in the model. They are implemented as temperature-dependent properties in form of fitting equations for certain temperature ranges (e.g. 25 - 200 °C, 200 – 300 °C etc.). Friction angle φ is set to 50° and is temperature-independent. Cohesive strength c and softening parameters (i.e. tables for cohesion, dilation, friction and tension) are back-calculated from lab test results. Figure 5-19 shows the softening parameters used in this model. If tensile crack width (corresponds to plastic tension strain) is large enough, the tensile strength of the element is approaching zero (Figure 5-19a). Considering that friction angle has negligible influence on the thermo-mechanical behavior, as the sensitivity analysis revealed, and assuming that dilation angle will approach zero after shear failure, they follow softening laws without temperature dependency (Figure 5-19b). It has been discovered that cohesive strength has obvious impact on thermal stress distribution (Wang and Konietzky 2019), and is therefore back-analyzed carefully for different temperatures (Figure 5-19c). Although these back-calculated softening parameters fit this lab test very well (nearly perfect), future analyses of more lab tests are necessary to obtain general softening laws.

Table 5-4 Back-analyzed parameters used for numerical modelling (Wang and Konietzky 2019)

Sample [°C]	v_s	ρ [kg/m^3]	E_c [GPa]	E_{input} [GPa]	c [MPa]
25	0.127	2643	26.96	29.5	15.88
200	0.098	2633	26.84	31	18.10
300	0.109	2632	30.83	36	20.20
400	0.095	2628	22.155	29	16.40
500	0.041	2608	16.21	21	15.00
600	0.038	2565	11.12	14	10.85
700	0.244	2449	2.73	3.56	5.80
800	0.367	2358	1.27	1.70	3.70

(a) Tension   (b) Friction and dilation angle   (c) Cohesion
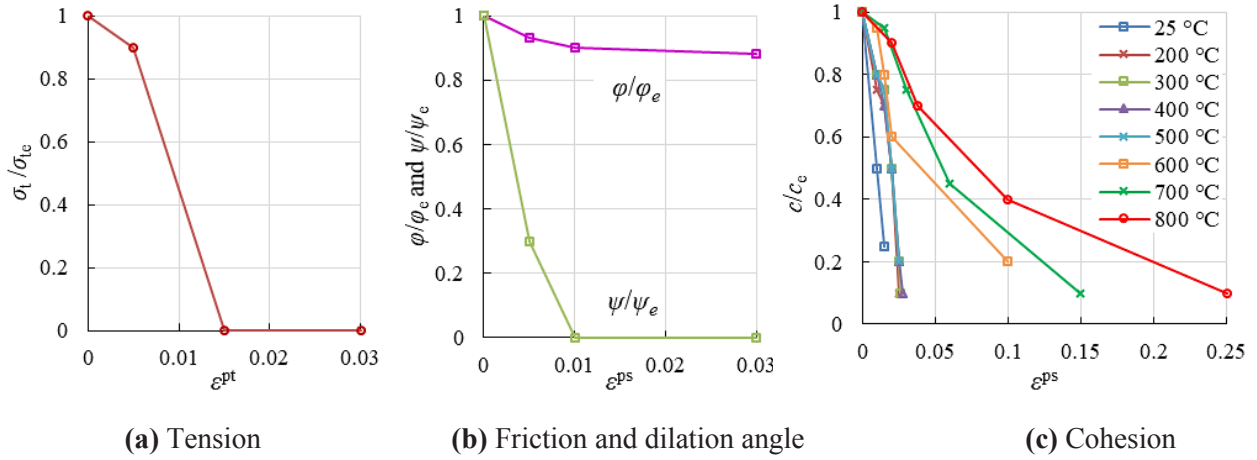
Figure 5-19 Variation of softening parameters with plastic strain. ε^{pt} is the plastic tension strain, ε^{ps} is the plastic shear strain, and subscript 'e' means the property at plastic strain $\varepsilon^p = 0$

Because of the extreme long run-times of the models, one quarter of the cylinder is used for model validation under the assumption of symmetry conditions. This holds for the homogeneous model, but is – in a strict sense - not correct for the inhomogeneous models. Therefore, coarse models of one-quarter (2250 elements) and a complete cylinder (9000 elements) with same element size and parameters were set-up. Figure 5-20 shows boundary conditions and tensile strength distributions as an example. To provide an insight into the complete cylinder model one quarter was hidden just for illustration (see Figure 5-20b). They are heated from 25 °C to 300 °C from the outer boundary (see Figure 5-17) with a rate of 5 °C/min. The temperature distributions of the two samples are quite similar (see Figure 5-21). Figure 5-22 shows the plasticity states of the models for 200 °C and 300 °C. The crack initiation starts at about 200 °C in the one-quarter and the cylinder sample. Also the failure evolution of these two models at higher temperatures are quite similar. The stress-strain behaviors of the two models are also compared (see Figure 5-23).

(a) Quarter   (b) Cylinder
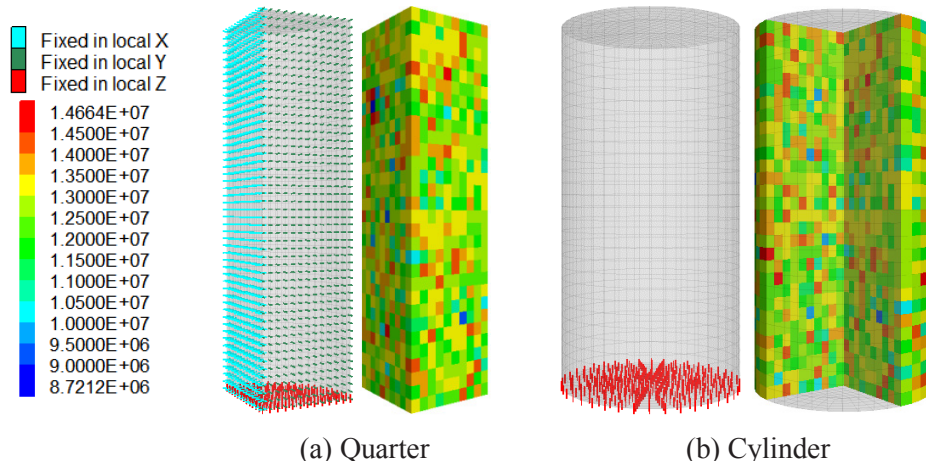
Figure 5-20 Boundary condition and tensile strength [Pa] distribution of one-quarter and complete cylinder model.

(a) Quarter   (b) Cylinder
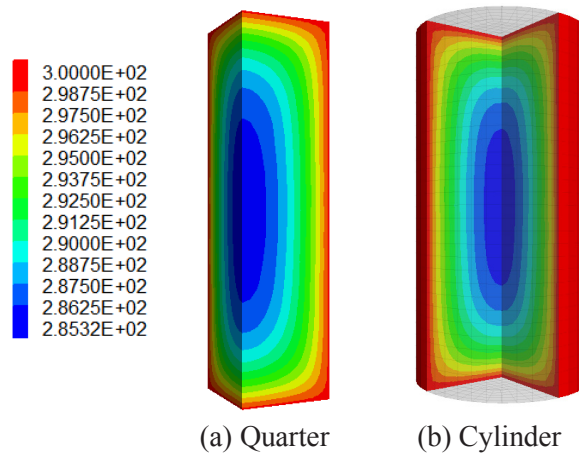
Figure 5-21 Temperature distribution of one-quarter and complete cylinder model at 300 °C

(a)200 °C   (b) 300 °C   (c) 200 °C   (d) 300 °C
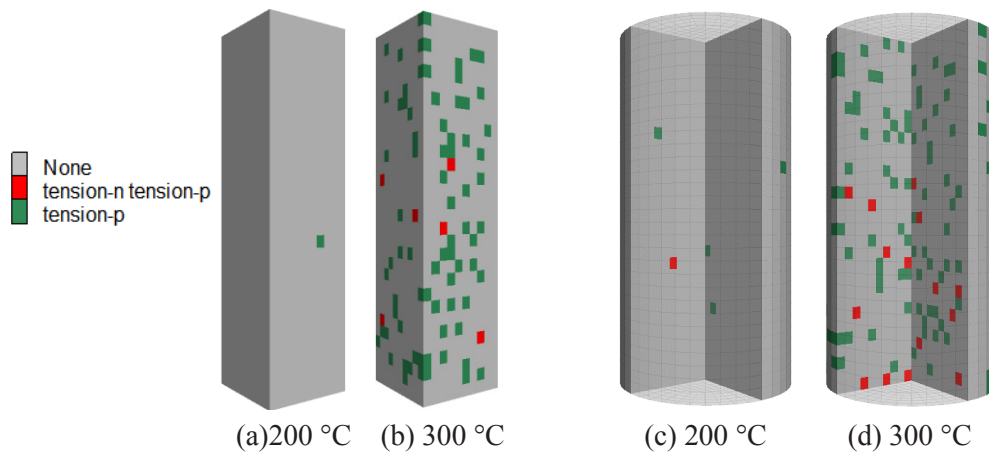
Figure 5-22 Thermal induced damages of one-quarter and complete cylinder model
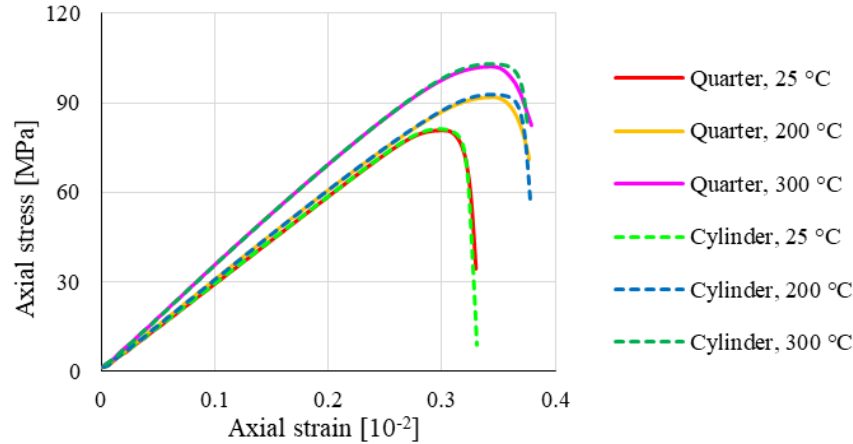
Figure 5-23 Stress-strain curves of one-quarter and complete cylinder model

The difference in mechanical behavior considering different temperatures is very small. However, the run-time for the cylinder model is about 8 times longer than that for the one-quarter model. With finer meshes, the difference increases significantly. Therefore, test calculations have shown that the deviation in terms of stress-strain behavior, temperature evolution and damage pattern between the full cylindrical inhomogeneous model and the corresponding one-quarter model are very small. Based on this finding, the simulations for model verification can be performed with one-quarter models.

The simulation of granite after heat treatments is based on the assumptions that in slow heating-cooling cycles: (1) thermal cracking and strength reduction only occurs during the heating process, and that there is no more property change once the temperature of the sample becomes uniform; (2) the influence of thermal gradient during the naturally cooling process up to room temperature can be neglected. These assumptions are based on lab test findings: Wang et al. (1989) counted acoustic emissions while a westerly granite sample was heated to a maximum temperature of 300 °C under confining pressures up to 55 MPa. No significant acoustic emissions were observed during cooling. Griffiths et al. (2018) performed heating and cooling cycles of Westerly Granite up to a maximum temperature of 450 °C at ambient pressure. By using acoustic emission monitoring and ultrasonic velocity measurements, they found that thermal microcracking during cooling is much less significant than during heating. Lin (2002) measured the permanent strain of Inada granite subjected to slow and homogeneous temperature change under atmospheric pressure.

He found almost no microcracking during cooling. The generation of new microcracks and the widening of the pre-existing ones are solely associated with the process of heating.

5.2.3.2 Thermal damage characteristics

Optical microscopic observations showed that 200 °C has not caused any visible thermal induced microcracks (Figure 5-24a) in this type of granite. Many boundary and transgranular cracks became visible when sample was heated up to 400 °C, but most grains still remain intact (Figure 5-24b). At 600 °C, microcracks have propagated across most grains with an obvious increase in crack quantity and width (Figure 5-24c).

Figure 5-25 shows plasticity states in numerical models for different temperatures. Failed elements can be interpreted as thermal induced microcracks. Just as the optical observations show, nearly no failures occur at 200 °C (Figure 5-25a). At 400 °C (Figure 5-25b), more zones fail in tension, but still many zones remain undamaged. However, the majority of zones experience tensile failure at 600 °C (Figure 5-25c), indicating a large number of tensile microcracks. The evolution of plasticity states in the numerical model can well reflect the microcrack generation in granite at elevated temperatures.
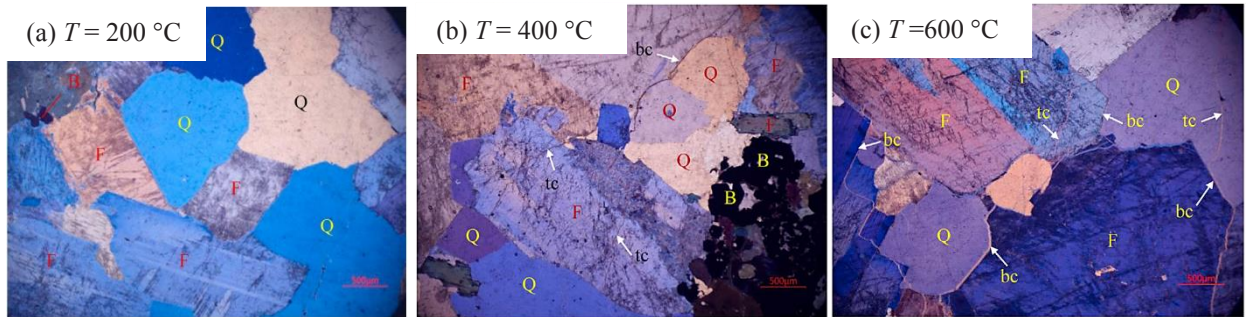
Figure 5-24 Optical microscopic observations of granite specimens at different temperatures: "bc" means "boundary crack", and "tc" means "transgranular crack" (Yang et al. 2017)

It should be noticed that at 600 °C, microcracks cannot be captured by X-ray CT technique with a minimum resolution of 30 μm (Figure 5-26). Only a few macrocracks wider than 30 μm can be observed at 700 °C, while the number of macrocracks shows an abrupt rise at 800 °C. The X-ray

CT scanning results also illustrate the inhomogeneous behavior of thermal induced cracks, which are isolated from each other and widespread over the whole sample.

(a) 200 °C   (b) 400 °C   (c) 600 °C
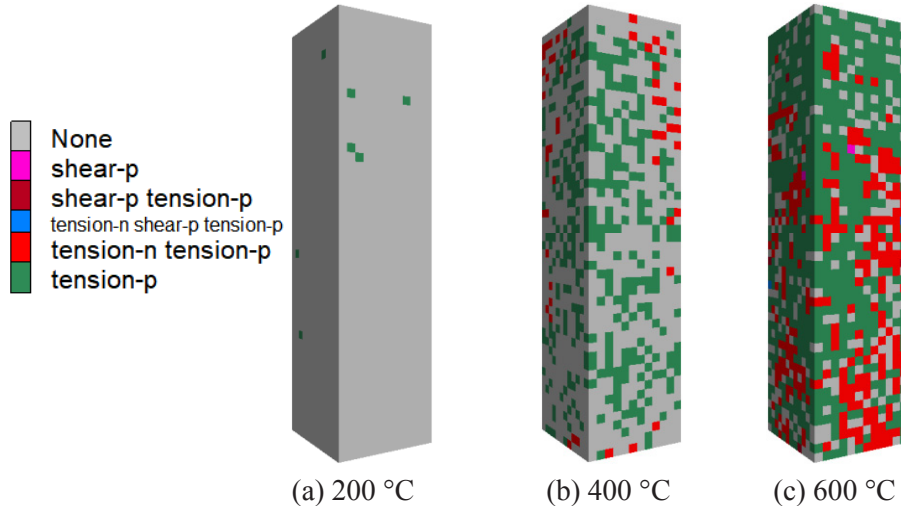
Figure 5-25 Plasticity states of the sample at different temperatures
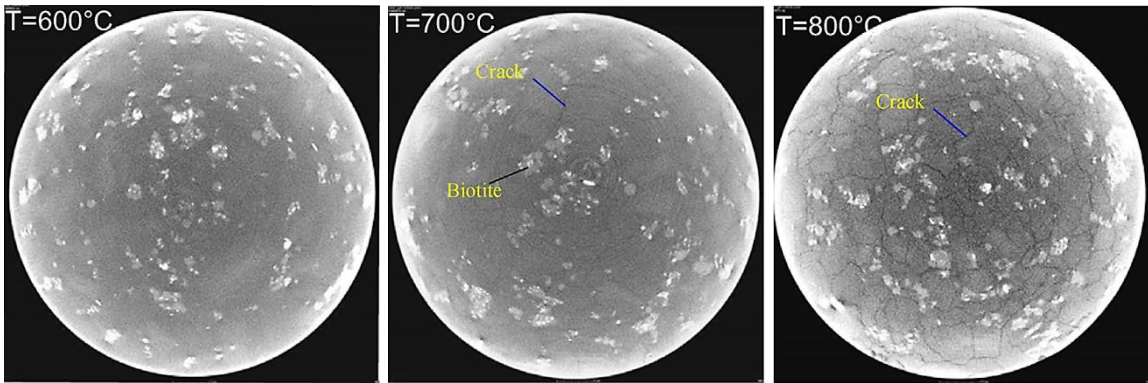
Figure 5-26 Horizontal cross-sections at a height of 35 mm of uniaxial loaded granite specimens after heat treatment (Yang et al. 2017)

In a simplified manner, it is assumed that the strain of thermally induced cracks of granite equals the tensile plastic strain in the numerical model. The length of model elements is between 1.10×10^{-3} and 2.6×10^{-3} m. The smallest width of the macrocracks is 30 μm. Then it can be deduced that the minimum plastic strain for macrocrack generation is about 1.15×10^{-2} to 2.73×10^{-2}. Figure 5-27 shows the plastic tensile strain at 700 °C for horizontal cross-sections at different height. The calculated plastic strains at 700 °C are mainly in order of 10^{-3}, only a few elements have plastic tensile strain larger than 10^{-2}. When heated to 800 °C (Figure 5-28), the macrocrack density is significantly increased as also shown in the lab test (Figure 5-26).

(a) Z = 10 mm	(b) Z = 35 mm	(c) Z = 60mm
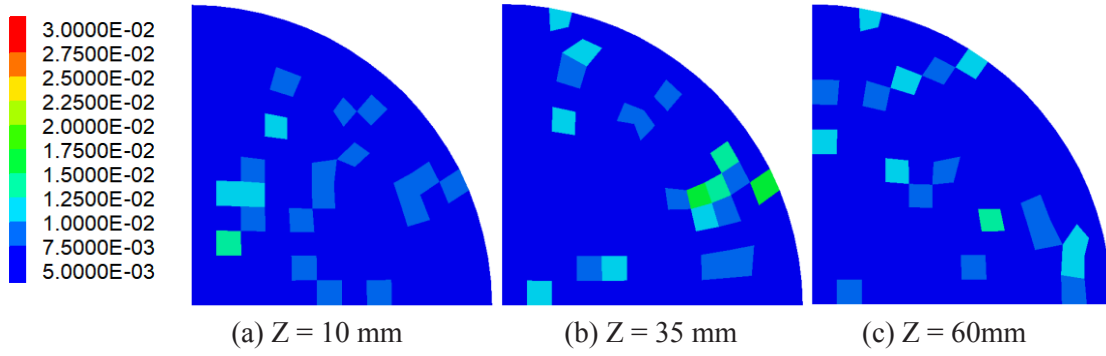
Figure 5-27 Plastic tensile strain at 700 °C for horizontal cutting planes of different height

(a) Z = 10 mm	(b) Z = 35 mm	(c) Z = 60 mm
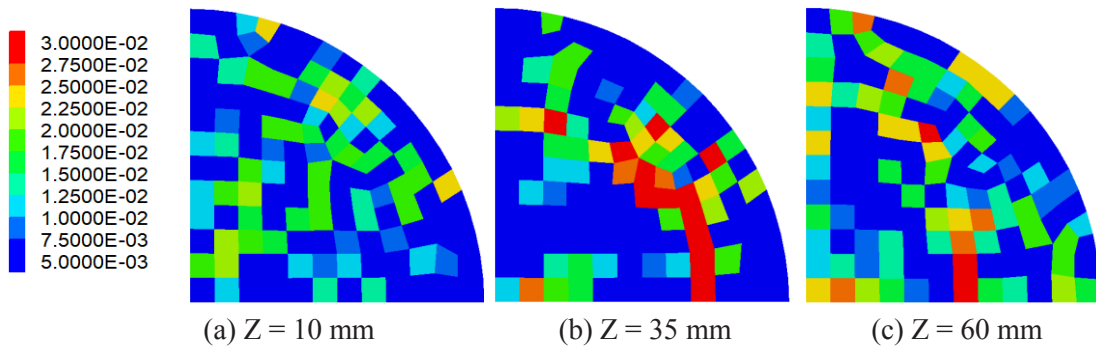
Figure 5-28 Plastic tensile strain at 800 °C for horizontal cutting planes of different height

Figure 5-29 shows the plastic tensile strains in vertical cross sections. From the strain distribution, we can infer that macrocracks with width greater than 30 μm can hardly be observed at temperatures up to about 600 °C (Figure 5-29a). But a large number of isolated macrocracks are formed at temperatures between 700 °C to 800 °C (Figure 5-29b, c). This is in a remarkable consistency with lab observations (see Figure 5-26), although strain contours are only an indirect way to investigate real cracks.

Figure 5-30a shows a CT image of an vertical cross section along the central part of the granite sample, and Figure 5-30b shows elements with plastic tensile strain larger than 1.15×10^{-2} (corresponds to crack width larger than 30 μm) at 800 °C. Figure 5-30c documents that also thermal cracks are quite distinct and covering the whole sample similar to the lab observations.

(a) 600 °C   (b) 700 °C   (c) 800 °C
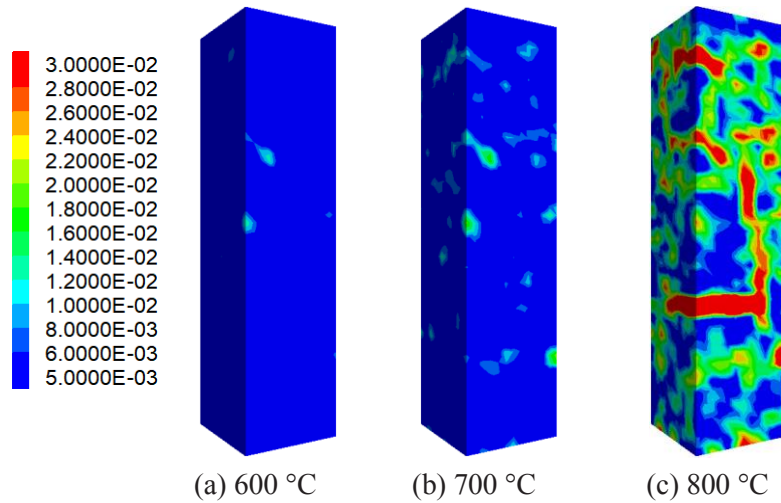
Figure 5-29 Plastic tensile strain observed at vertical cutting planes at different temperatures

(a)   (b)   (c)
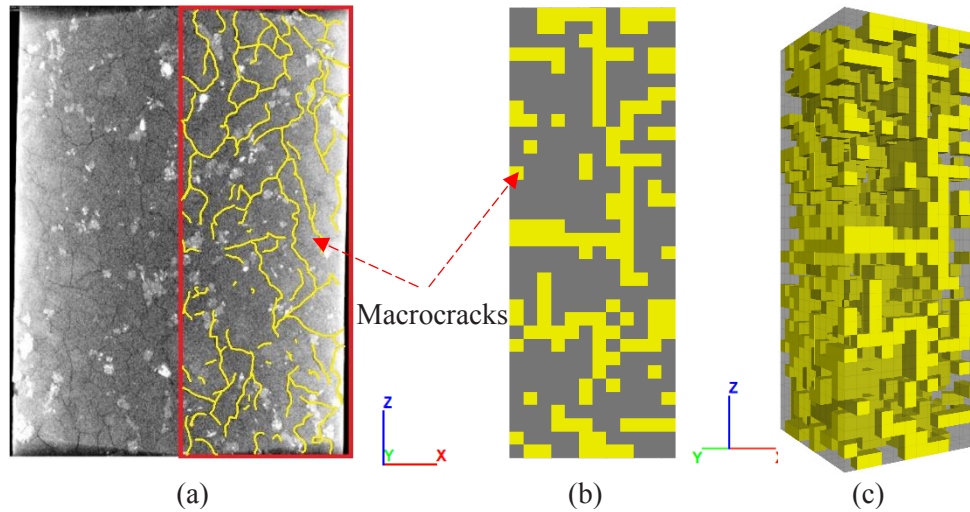
Figure 5-30 Macrocracks of granite at 800 °C: (a) vertical cross-section along centre of sample (Yang et al. 2017); (b) simulated macrocracks along vertical cross section; (c) simulated 3D macrocrack pattern

5.2.3.3 Mechanical test after heat treatment

After heat treatment, the thermo-mechanical coupling is deactivated and simulation is continued by pure mechanical uniaxial compression test at room temperature. Figure 5-31 shows the vertical stress-strain relations for samples heated up to different temperatures. The brittle characteristic of granite is obvious for temperatures up to about 300 °C, but above this temperature ductility becomes more and more predominant. These curves reproduce quite well the lab test results shown in Figure 5-18.

Table 5-5 documents the peak values of axial stress σ_{cs} and the corresponding strain ε_{cs} obtained from the simulations. The relative error of stress and strain (δ_σ and δ_ε) between lab test and numerical simulation are also documented. As Figure 5-32 shows, peak axial stress and strain have a great consistency with the lab test results. This verifies again the accuracy and physical plausibility of the developed numerical model used in this study.
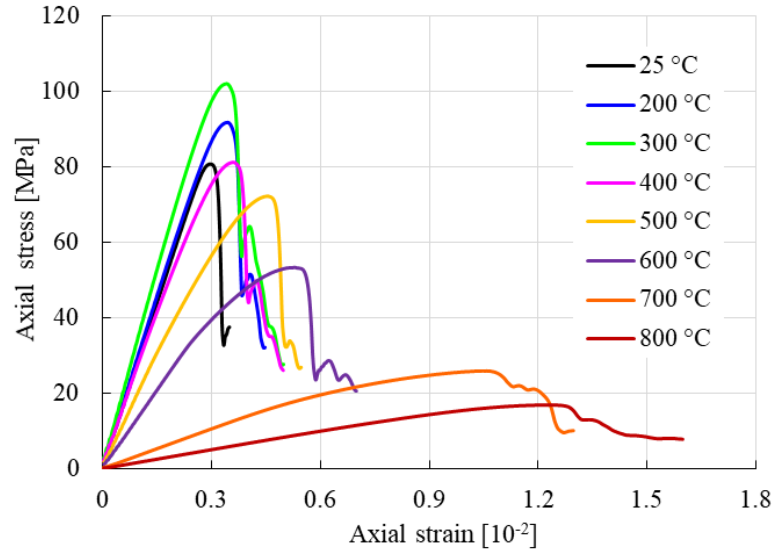
Figure 5-31 Simulated stress-strain relations for uniaxial compression tests on samples exposed to different temperatures before (compare with Fig. 5-18)

Table 5-5 Simulation results of peak axial stress and strain

Specimen [°C]	σ_{cs} [MPa]	δ_σ [%]	ε_{cs} [10^{-2}]	δ_ε [%]
25	80.73	0.84	0.297	0
200	91.74	1.72	0.343	2.08
300	102.02	-0.02	0.342	3.32
400	81.19	-0.66	0.361	-2.17
500	72.23	-0.07	0.455	2.02
600	53.33	-4.07	0.527	5.4
700	25.89	-6.53	1.057	4.04
800	16.84	9.71	1.214	0.33

(a) Peak axial stress (b) Peak axial strain
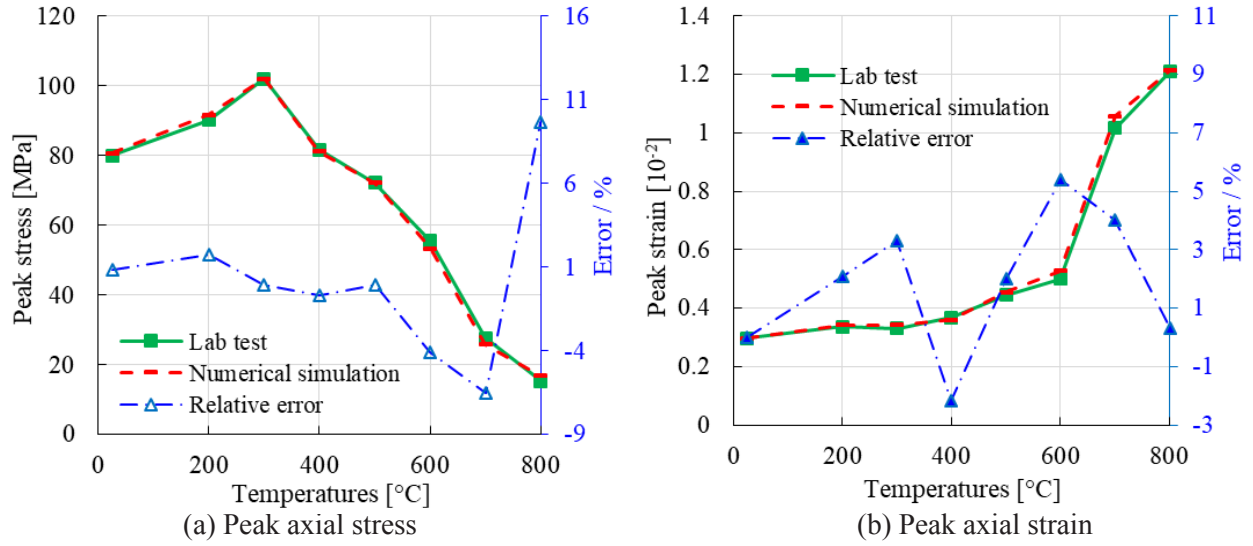
Figure 5-32 Comparison of simulation and lab test results

Simulation results indicate, that a modelling strategy using a modified Mohr-Coulomb model with strain softening and tension cut-off in combination with stochastic parameter distribution and temperature dependent adjustment of parameters (tensile strength, Young's modulus, cohesive strength, thermal conductivity, Poisson's ratio, thermal expansion coefficient, specific heat) allows to simulate thermal induced damage in a realistic manner. The comparison of damage and fracture patterns as well as stress-strain relations between lab data and numerical simulations based on the new proposed procedure show a remarkable agreement, which can be considered as a first validation of the proposed modelling strategy.

6 Methodology for heterogeneity characterization of rocks

Although the statistical distribution method (e.g. Weibull distribution) can be used to reproduce the heterogeneous nature of granite, it lacks the factual mineral composition of the rocks. Another approach, the mineral based method, has some obvious drawbacks such as: (i) it heavily depends on detailed micro-observations and digital image processing (DIP); (ii) reconstruction of three-dimensional bodies of heterogeneous materials is restricted; (iii) only one specific configuration is duplicated; (iv) models at the grain size level are restricted in size due to the restricted computational power. A new method to characterize the heterogeneity of rocks is needed to improve the accuracy and rationality of such simulations.

A new methodology combining Weibull functions and the real mineral composition of granite is proposed, which overcomes the shortcomings of using existing methods for the heterogeneity characterization of rocks at the grain size level. The proposed Weibull-mineral based model can simulate thermal cracking of rocks in a more realistic way compared with previous methods such as the mineral-based model. This study also reveals the importance of thermo-mechanical property distributions at the grain size level for the overall thermo-mechanical behaviors at larger scale. Supported by lab tests, the proposed numerical model can well reproduce the lab results of thermal induced micro- and macro-cracks, as well as the stress–strain behavior and the final failure pattern of granite after heat treatments.

6.1 Heterogeneity of granite

The general percentage of quartz, feldspar, and mica in granite is approximately 25%, 60%, and 15%, respectively. The percentage of main minerals in granites are usually quite stable at high temperatures as shown in Figure 6-1, at least for the main component of feldspar and quartz. This means that we can build a numerical model without considering the chemical reactions and mineral changes at elevated temperatures.

A brief literature review was conducted in order to collect mineral properties (see Table 6-1). The mineral properties show some significant variations, and some properties like reliable tensile strength are lacking. Because thermal expansion coefficients of minerals are usually documented

as volumetric or linear expansion values for different directions, we used one-third of the volumetric coefficient as linear expansion coefficient for isotropic thermal models according to the general relationship of $\beta_t = 3\alpha_t$ (Ramana and Sarma 1980; Huotari and Kukkonen 2004). Siegesmund and Snethlage (2013) believe that quartz and mica have high expansion coefficients and feldspar has a low expansion coefficient. They also stated that the linear thermal expansion coefficient for quartz lies between $9 \times 10^{-6}/°C$ and $14 \times 10^{-6}/°C$, and the average coefficient of mica is around $8.7 \times 10^{-6}/°C$ to $17.8 \times 10^{-6}/°C$ (Mckinstry 1965; Siegesmund and Snethlage 2013). However, many other researchers suggest that the coefficient of mica (including biotite) is the smallest with a value of $3 \times 10^{-6}/°C$ (Yu et al. 2012; Zhao 2016; Yang et al. 2018), and the value $24.3 \times 10^{-6}/°C$ for quartz (Fei 1995) is supposed to be the volumetric coefficient which is three times the linear one. Based on these references, we set the linear thermal coefficients of different minerals as shown in Table 6-1, and the mean value of $5.69 \times 10^{-6}/°C$ falls within the range of $5 \pm 1.6 \times 10^{-6}/°C$ for the linear thermal expansion coefficient of granite investigated by Huotari and Kukkonen (2004). The compressive strengths deduced from the hardness indices of Quartz, Feldspar and Mica are 200, 180, and 120 MPa (Tham et al. 2001), respectively. The ratio of compressive strength to tensile strength for granite is about 15 according to simulation and experimental results (Yu et al. 2012; Zhou et al. 2017). Therefore, the tensile strength of each mineral can be deduced approximately as shown in Table 6-1.
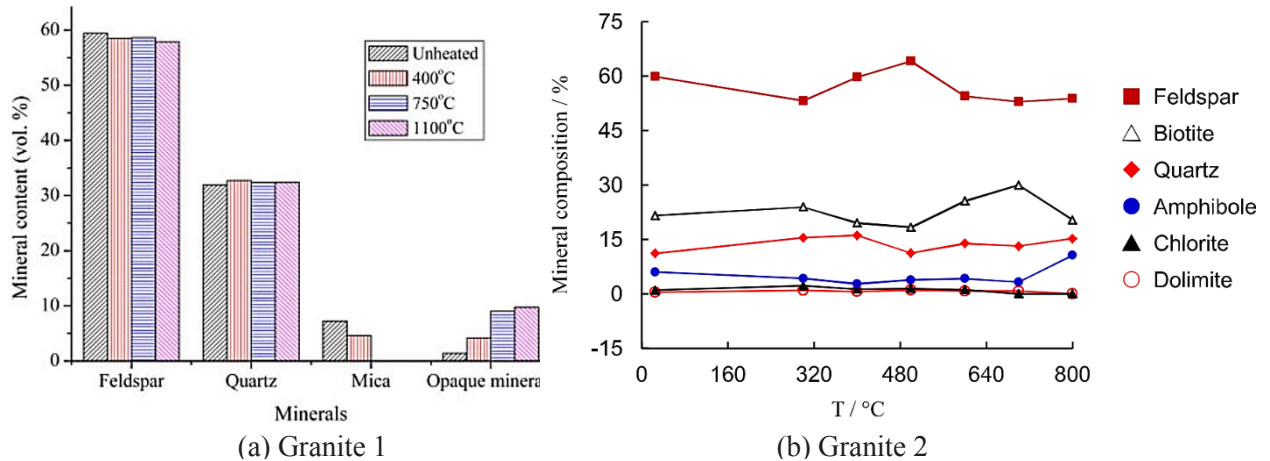
Figure 6-1 Mineral composition of different granites at different temperatures. (a) Granite 1 (Saiang and Miskovsky 2011); (b) Granite 2 (Yang et al. 2017)

The scatter characteristics of the mineral properties can be described by the variance σ_x^2. The mean μ_x and the variance σ_x^2 of discrete random variable x can be calculated by:

$$\mu_x = \sum_{i=1}^{n} p_i \cdot x_i \tag{6-1}$$

$$\sigma_x^2 = \sum_{i=1}^{n} p_i \left(x_i - \mu_x \right)^2 \tag{6-2}$$

where p_i is the probability of discrete random variable x_i.

Table 6-1 Mineral properties and corresponding Weibull parameters

Mineral	α_t $(10^{-6}/°C)$	C_v (J/kg°C)	k (W/m°C)	E (GPa)	φ (°)	c (MPa)	v	σ_t (MPa)	ρ (kg/m³)	Pct. %
Quartz	8	700 [g]	7.69 [e]	81 [f]	60 [c]	50 [d]	0.16 [f]	13	2650 [g]	25
Feldspar	5.4[a]	630 [g]	2.31 [e]	52 [f]	50 [c]	40 [d]	0.19 [f]	12	2570 [g]	60
Mica	3[b]	520 [g]	2.15 [e]	25 [f]	30 [c]	25 [d]	0.22 [f]	8	3120 [g]	15
μ_x	5.69	631	3.63	55.2	49.5	40.25	0.187	11.65	2673	
$E(x)=\mu_x^{norm}$	1	1	1	1	1	1	1	1	1	
$Var(x)=\sigma_x^2$	0.076	0.0076	0.417	0.101	0.035	0.036	0.010	0.019	0.005	
m	4.1	14	1.6	3.5	6.3	6.1	12.1	8.8	17.4	
x_0	1.101	1.038	1.115	1.111	1.075	1.077	1.043	1.057	1.031	

[a] (Robertson 1988), [b] (Yang et al. 2018), [c] (Tham et al. 2001), [d] (Chen et al. 2004), [e] (Clauser and Huenges 1995), [f] (Wei 2015), [g] (Yu et al. 2012)

In Table 6-1, μ_x^{norm} is the mean value of the normalized mineral properties obtained by dividing the mineral property by the mathematical expectation, and it equals $E(x)$ of the Weibull variables. Then the corresponding variance σ_x^2 is obtained for each normalized parameter according to Eq. (6-2) (see Table 6-1). Results show that the variances of different properties are obviously distinct from each other, which makes it inappropriate to use one homogeneity index m to represent all of these variations. To obtain the Weibull parameters based on the mineral composition, we set $Var(x)$ of the Weibull distribution equal to σ_x^2 of the granite minerals. Then we obtain the corresponding Weibull parameters according to Eq. (5-13) and (5-14) (see Table 6-1). The statistical distribution based on mineral composition is physically significant, and the reconstruction of granite samples can represent the heterogeneity of mineral distributions in a quantitative manner.

6.2 Model set-up for different approaches

A cylindrical sample (Figure 6-2) with a diameter of 50 mm and a length of 100 mm is created in FLAC³D. 26,000 elements were generated and the average edge length of the elements is 1.96 mm.

Five history points (see Figure 6-2b and c) are added to monitor the longitudinal and lateral deformation of the sample during the thermo-mechanical loading. During heating, the sample bottom (i.e. the XY plane) is fixed in vertical direction and a heat flux is applied to all surfaces. During the uniaxial compression test (Figure 6-2b), at bottom and top of the sample a low velocity $(1 \times 10^{-8}$ m/s) is applied in the vertical direction. For uniaxial tension tests, a lower velocity $(1 \times 10^{-9}$ m/s) is applied at the two ends of the cylinder (see Figure 6-2c). In both cases quasi-static conditions are guaranteed.

(a) Cylindrical sample   (b) Uniaxial compression   (c) Uniaxial tension
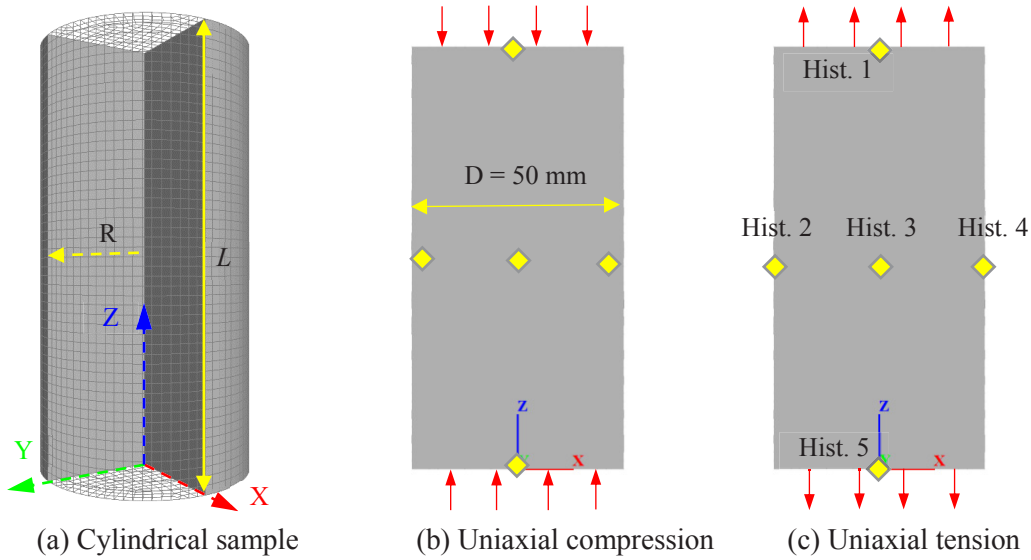
Figure 6-2 Numerical model set-up for granite samples

Three models (see Table 6-2) are created: reference Model A is homogeneous without heterogeneous property distributions. The second approach (see Figure 6-3a) is the Weibull-mineral based model (Model B) using statistical distribution parameters given in Table 6-1. The mean values μ_x are used as macro property P_0 for assigning different properties to the elements. The third approach (Figure 6-3b, c) is based on the general mineral composition (i.e. 25 % quartz, 60 % feldspar, and 15 % mica) according to Table 6-1, and the property of each mineral is assigned separately (Model C). A big advantage of Model B is, that the randomly distributed properties can represent the mineral composition more realistic since natural granites do not consist only of three minerals. For instance, a few elements with very small tensile strengths (e.g. 3.3 MPa in Figure 6-3a) could represent grains with pre-existing flaws, fluid inclusion, or trace minerals etc.

Table 6-2 Models with different property distributions

Approach	Model	Input properties
Homogeneous	A	Mean values from Table 6-1
Weibull-mineral based	B	Weibull parameters and mean values (Table 6-1)
Mineral-based	C	Mineral properties from Table 6-1

(a) Model B   (b) Model C   (c) Model C
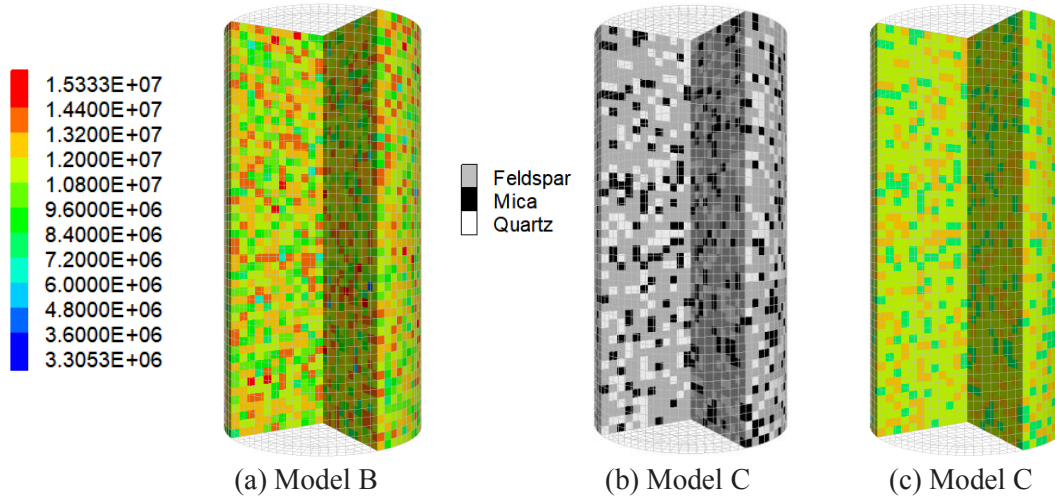
Figure 6-3 Property and mineral distribution of different models: (a) Tensile strength [Pa] distribution of Weibull-mineral-based Model B, (b) Mineral components of mineral-based Model C, (c) Tensile strength [Pa] distribution of mineral-based Model C

The general temperature-dependent properties are discussed in great detail in chapter 2.2, and the deduced fitting equations are summarized in Table 2-1. The temperature-dependent property of element i is denoted as $P_i(T)$, while $P_{0i} = P_0 \cdot x_i$ represents the element property at room temperature. The new constitutive law (see Figure 5-17) based on a Mohr-Coulomb model with strain softening and tension cut-off in combination with statistical parameter distribution and temperature dependent adjustment of parameters is used. After the onset of plastic yielding, the strain-softening law assumes both, brittle softening (due to reduction in cohesion and tension) and gradual softening (due to a reduction in friction angle). The piecewise-linear softening relations (see Figure 6-4) in these models with general property values are set based on the previous work (Figure 5-19). Since the shear softening laws at different temperatures are very similar below 200 °C, they are treated as temperature independent in these preliminary models which are heated up to 180 °C (see Figure 6-9).

(a) Tension

(b) Cohesion and friction angle
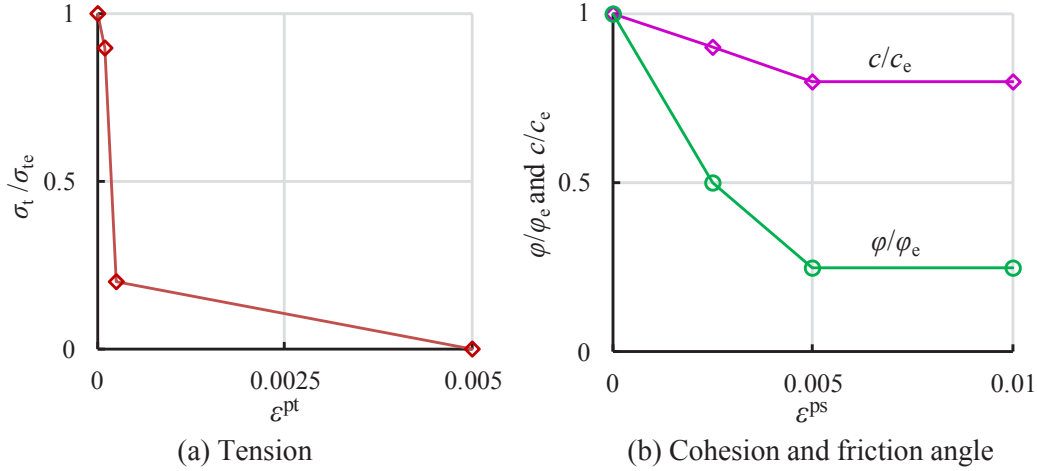
Figure 6-4 Variation of softening parameters with plastic strain. ε^{pt} is the plastic tensile strain, ε^{ps} is the plastic shear strain, and subscript 'e' means the property at plastic strain $\varepsilon^{p} = 0$

6.3 Thermo-mechanical properties and cracking behavior of different approaches

6.3.1 Uniaxial compression tests

Figure 6-5 shows the stress-strain relationships of different models during uniaxial compression tests. The homogeneous Model A has the greatest compressive strength of 217 MPa, which is 34 % higher than the Weibull-mineral based Model B (162 MPa) and 36 % higher than the mineral-based Model C (160 MPa). This is in consistence with previous studies (Cao et al. 2004; Liu et al. 2004; Tan 2013) which show that the dispersion degree of property distribution can influence the rock strength, and a higher dispersion (i.e. a smaller homogeneity index m) results in a lower strength. The simulated compressive strengths of Model B and C are very similar and the difference between them is only 1.3%. This trend is also observed for elastic modulus calculated from the linear part of the stress-strain curve. The homogeneous Young's modulus E_A of 55.1 GPa is almost the same as the input model parameter (55.2 GPa), while E_B (Weibull-mineral based Model B) and E_C (Mineral-based Model C) are slightly lower (7.6 % and 6.4 %, respectively) than the input value but again very close to each other (see Figure 6-5a).

Figure 6-5b shows the development of Poisson's ratio until reaching a constant value at the elastic stage. The Poisson's ratio of Model A (v_A) is the same as the input value of 0.187. The Weibull-

86

mineral based value v_B is only 1.1 % lower. The biggest deviation of the Poisson's ratio occurs in Model C but is only 4.8 % smaller than the result of the homogeneous model.

(a) Uniaxial stress-strain curve

(b) Development of Poisson's ratio
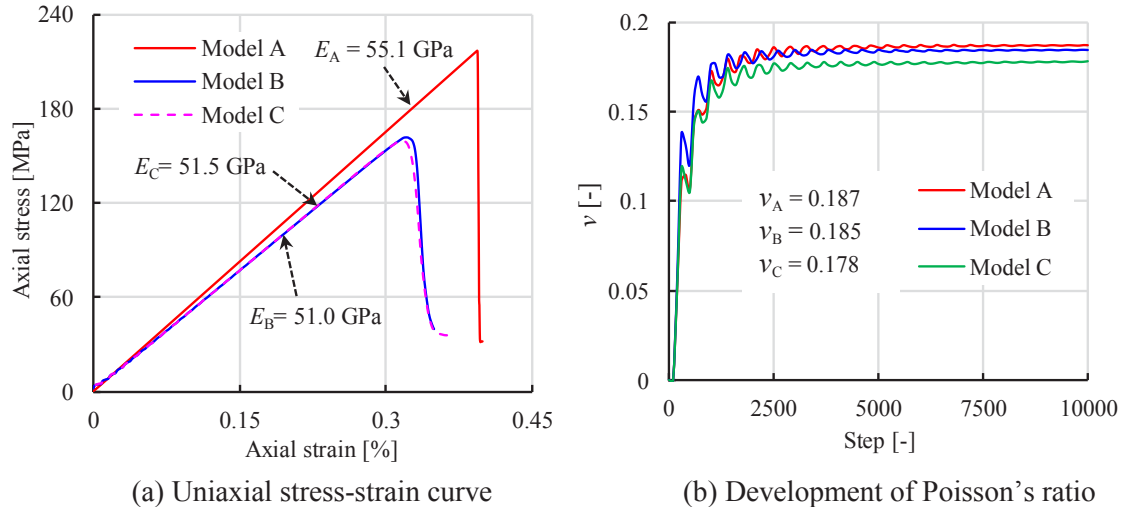
Figure 6-5 Uniaxial compression test results of different models

In order to detect the influencing factors for the strength reduction of the heterogeneous models, 7 groups of models based on Model B are designed (see Table 6-3). Only the parameters to be analyzed are changed into homogeneous, while other parameters are the same as in the heterogeneous model (Model B).

Table 6-3 Strength parameters for model analysis

Model	φ [°]	c [MPa]	E [GPa]	v [-]
B1	49.5	-	-	-
B2	-	40.25	-	-
B3	49.5	40.25	-	-
B4	-	-	55.2	-
B5	49.5	40.25	55.2	-
B6	-	-	-	0.187
B7	49.5	40.25	55.2	0.187

As expected, results of Model B1, B2 and B3 show that cohesion and friction angle have some influence on the macroscopic compressive strength (see Figure 6-6). The homogeneous Young's modulus shows a great influence on the stress-strain relationships, and leads to a significant reduction of the macro strength of the sample (B4). The peak strength of 206.8 MPa for Model B5 indicates that all the three parameters (cohesion, friction angle, and Young's modulus) together

have a dominant effect on the uniaxial strength of the heterogeneous sample. Model B6 has almost the same strength as the homogenous model, indicating that Poisson's ratio has only a minor influence. Considering the fact that only Poisson's ratio of the heterogeneous model equals the input value (lab test result), all the other parameters including cohesion, friction angle, and Young's modulus need to be back-calculated for the heterogeneous model.
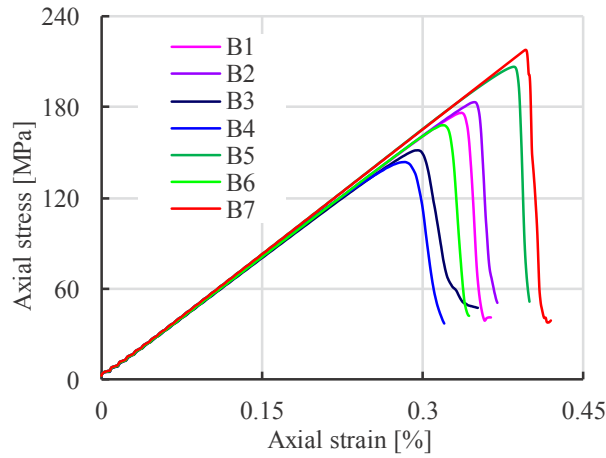
Figure 6-6 Uniaxial compression results of different models

6.3.2 Direct tensile tests

Tensile strength also shows an obvious reduction caused by heterogeneity (see Figure 6-7). The tensile strength of Model A (homogeneous) is 11.61 MPa, which is nearly the same as the input tensile strength of 11.65 MPa. The tensile strength of Model C (9.38 MPa) is 19.5 % lower than the input parameter, while the strength of Model B (9.01 MPa) is 22.7% lower. To investigate the influencing factors on the strength reduction, a set of models with various minimum tensile strengths (tensile strengths of micas) are designed (Table 6-4). Because the tensile behavior of Model B and C are very similar, only the Weibull-mineral based models are built exemplary on the basis of Model B. All the other parameters are the same as for the reference model (Model B). The simulation results are documented in Figure 6-7b and Table 6-4.

The value of the mineral tensile strength (σ_t^{mica} in this case) can significantly influence the homogeneity index m, especially when $\sigma_t^{mica} > 9$ MPa (i.e. closer to the value of quartz and feldspar) (see Figure 6-7b). When $\sigma_t^{mica} < 7$ MPa, the simulated tensile strength and m show a simultaneous growth, indicating the influence of m on the macroscopic tensile strength. However, this influence

is almost negligible afterwards, and the rapid increase of m does not contribute to the increase of final strength. Another noticeable phenomenon is that the difference δ between the input value and the output value (simulation result) vary only slightly between 2 and 3 MPa for the whole range (see Table 6-4). Considering that the maximum variation of the mean value is only 1.2 MPa while m grows nearly 9 times from 4.2 to 36.5, we can infer that it is the mean value of the mineral strengths and not the m that dominants the macroscopic tensile strength of the sample. This finding is helpful for the investigation of appropriate tensile strength for heterogeneous models, especially when the homogeneity index m of a granite has been determined based on the mineral composition.

(a) Stress-strain relationships   (b) Influence of mica on macroscopic strength
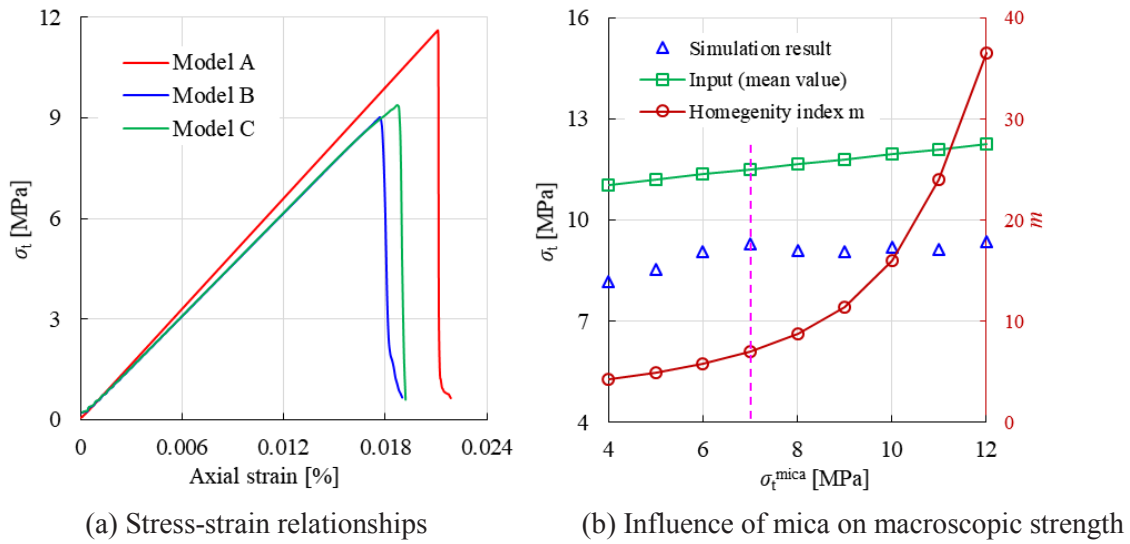
Figure 6-7 Stress-strain relationship in uniaxial tension test

Table 6-4 Weibull parameters for different mineral tensile strength

Model	σ_t^{mica} [MPa]	σ_t^{input} [MPa]	$Var(\sigma_t)$	$m_{\sigma t}$	$x_{\sigma t}$	$\sigma_t^{simulation}$ [MPa]	δ
B8	4	11.05	0.0733	4.2	1.100	8.17	2.88
B9	5	11.20	0.0555	4.9	1.090	8.53	2.67
B10	6	11.35	0.0406	5.8	1.080	9.07	2.28
B11	7	11.50	0.0284	7.0	1.069	9.29	2.21
B12	8	11.65	0.0186	8.8	1.057	9.09	2.56
B13	9	11.80	0.0112	11.4	1.046	9.07	2.73
B14	10	11.95	0.0059	16.0	1.034	9.20	2.75
B15	11	12.10	0.0027	24.0	1.023	9.12	2.98
B16	12	12.25	0.0012	36.5	1.015	9.35	2.90

6.3.3 Thermal expansion

The coefficient of volumetric thermal expansion β_t is:

$$\beta_t = \frac{1}{V} \frac{\Delta V}{\Delta T} \qquad (6\text{-}3)$$

where V = initial volume of sample, ΔV = change in volume of sample, ΔT = temperature change.

The average volume of the cylinder at different temperatures is calculated by $V = \pi R^2 L$ (see Figure 6-2a). To obtain the thermal expansion coefficients of the sample at room temperature, the model is heated from 25 °C to 26 °C with a slow heating rate of 2 °C/min until the sample is reaching a uniform temperature of 26 °C. Table 6-5 shows the simulation results of thermal expansion coefficient. The simulated coefficient is 5.68×10^{-6}/°C for Model A, which is almost the same as the input value (5.69×10^{-6}/°C), while the value for the mineral-based model is 5.8 % higher. With a linear thermal expansion of 6.19×10^{-6}/°C, Model B shows the largest deviation (about 8.8 % higher). For simplicity, the lab test results of thermal expansion coefficient can be used directly for the heterogeneous models.

Table 6-5 Simulated thermal expansion coefficient of different models

Models	V [m³]	ΔV [m³]	β_t [10^{-6}/°C]	α_t [10^{-6}/°C]
Model A	1.96×10^{-4}	3.35×10^{-9}	17.05	5.68
Model B	1.96×10^{-4}	3.65×10^{-9}	18.57	6.19
Model C	1.96×10^{-4}	3.54×10^{-9}	18.03	6.01

6.3.4 Thermal induced cracking

A homogeneous model is not suitable to simulate thermal cracking at the grain size level, therefore only results of the heterogeneous models are documented in this section. Since all the parameters adopted in these models are originated from literature without calibration, the results of thermal cracking here are only used for illustration and comparison. In order to have a deeper insight into the influence of mineral properties on thermal cracking behavior, Model D modified from the mineral-based model (Model C) is added. The feature of Model D is that the property value of each mineral (quartz, feldspar, and mica) varies according to Weibull variables limited in a range of 0.85 to 1.15. The homogeneity index $m = 8$ of Model D is the average value of all the properties in Table

6-1, and the corresponding x_0 is 1.06. The mineral composition of Model D is the same as for Model C but the element properties vary on the basis of the mineral values in Table 6-1. For example, the tensile strengths of quartz, feldspar, and mica are 13 ± 1.95 MPa, 12 ± 1.8 MPa, and 8 ± 1.2 MPa (see Figure 6-8), respectively.

| 1.4950E+07 |
| 1.4250E+07 |
| 1.3500E+07 |
| 1.2750E+07 |
| 1.2000E+07 |
| 1.1250E+07 |
| 1.0500E+07 |
| 9.7500E+06 |
| 9.0000E+06 |
| 8.2500E+06 |
| 7.5000E+06 |
| 6.8000E+06 |

(a) Quartz   (b) Feldspar   (c) Mica
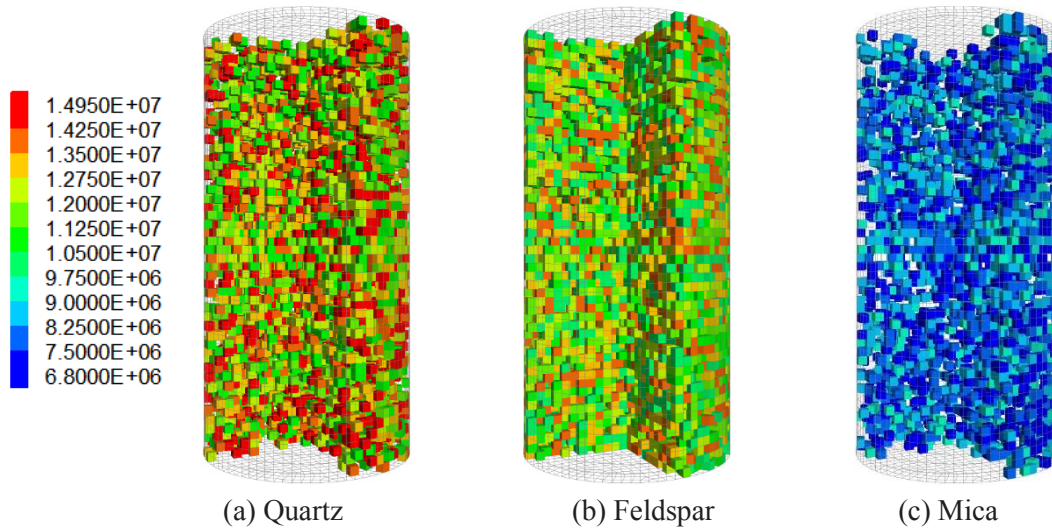
Figure 6-8 Tensile strength [Pa] distribution of different minerals in Model D

The initiation of thermal cracks in Model B begins at 85 °C (see Figure 6-9). The mineral-based model (Model C) shows first thermal cracks about 5 °C in advance. Although the failure characteristics show some general similarities, the yielding elements are different in terms of numbers and development. In Model B, the number of cracks increase gradually with rising temperature. This characteristic of thermal crack development is consistent with lab test observations (Bauer and Johnson 1979; Lin 2002) in a qualitative way. Model C shows a stepwise growth in crack numbers. In Model C and D the majority of failures at the beginning stage (about 75 to 100 °C) are originated from mica minerals with smaller tensile strengths (see Figure 6-9c, d, e, and f). Because all the micas have the same property in Model C, most of them tend to yield simultaneously once the accumulated stress exceeds the tensile limit. Therefore, the stepwise development of cracks is attributed to the property gaps between different minerals. Although Model D has the same mineral distribution as Model C, no obvious stepwise trend occurs in the crack development since the mineral properties in Model D are assigned according to the continuous probability distribution. On the other hand, the element properties in Model B are relatively smooth according to statistical equations. As a result, the thermal stresses will not exceed

the strength of many elements at the same time, leading to a gradual increase in thermal cracking. Although Model C is very similar to Model B in terms of the mechanical behavior, it is not capable of representing the thermo-mechanical behavior in a proper manner.
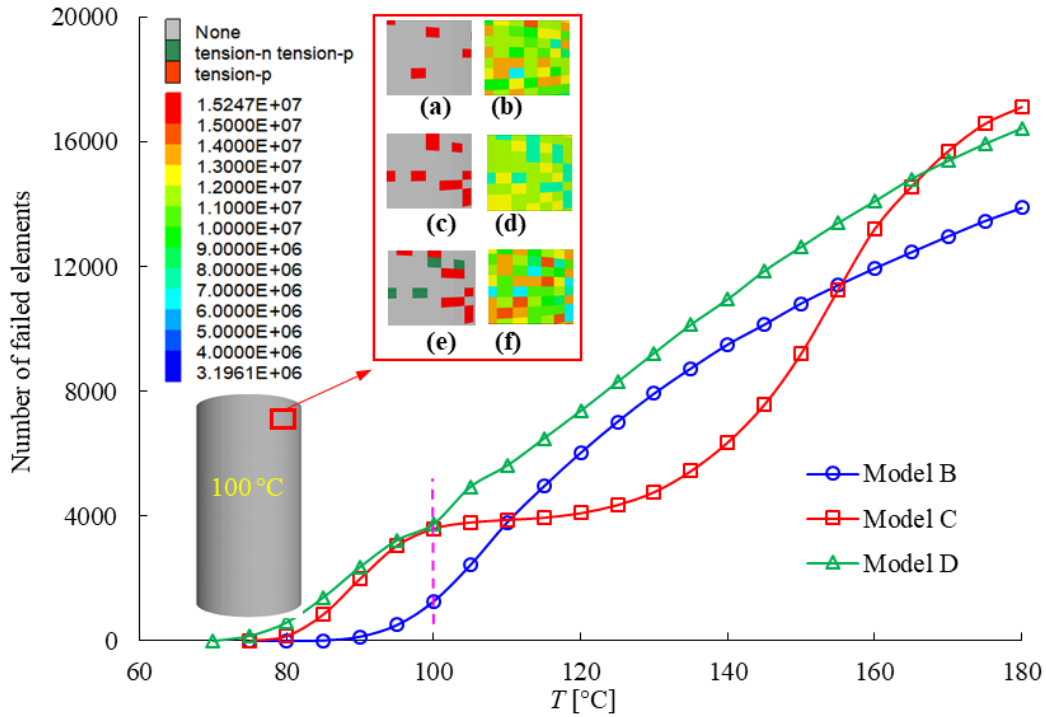
Figure 6-9 Number of cracks at different temperatures. (a) Plasticity states of Model B. (b) Tensile strength [Pa] distribution of Model B. (c) Plasticity state of Model C. (d) Tensile strength [Pa] distribution of Model C. (e) Plasticity states of Model D. (f) Tensile strength [Pa] distribution of Model D

6.4 Validation of the proposed method for property distribution

6.4.1 Determination of numerical parameters based on lab testing

The Laurentian granite consists of about 60 % feldspar, 33 % quartz, and 3–5 % biotite (Yin et al. 2015). The proposed inhomogeneous continuum models are composed of 60 % feldspar, 33 % quartz, and 7 % mica. All the necessary parameters for the numerical model are calculated and documented in Table 6-6. The parameter values of minerals are the same as documented in Table 6-1, while the statistical distribution parameters calculated on the basis of the mineral proportion are different.

The equation used to determine the Brazilian tensile strength (BTS) is given by Eq. (4-1). The equation is obtained assuming that the sample is isotropic and only tensile failure is produced. Since most rocks fail in both, tensile and shear mode, the results obtained by this equation are not always equal to the actual tensile strength (Dinh 2011; Kwok and Duan 2015). Besides the strain-softening disc (Figure 6-10b), another model with elastic lower and upper parts (Figure 6-10c), which can prevent the generation of shear failures, is also designed for comparison.

Table 6-6 Parameters for Weibull-mineral model

Mineral	α_t (10^{-6}/°C)	C_p (J/kg°C)	k (W/m°C)	E (GPa)	φ (°)	c (MPa)	v	σ_t (MPa)	ρ (kg/m³)
u_x	6.1	645.4	4.1	59.7	51.9	42.3	0.18	12.1	2634.9
m	4.7	16.9	1.7	4.1	8.2	7.6	12.8	12.2	24.0
x_0	1.09	1.03	1.12	1.10	1.06	1.06	1.04	1.04	1.02
P_0 input	2.90	645.4	2.5	98.5	51.9	55	0.21	16	2630

For Laurentian granite an indirect tensile strength of 12.8 MPa was obtained by Brazilian tests with flat platens (Yin et al. 2015). The corresponding model is shown in Figure 6-10a. The flat platens have a dimension of 40 × 20 ×10 mm, and they are elastic with a bulk and shear modulus of 160 GPa and 80 GPa, respectively. The Laurentian granite disc has a nominal diameter of 40 mm and a thickness of 18 mm. 8880 elements were used for the corresponding numerical model.

The sample deforms as the load increases, therefore, an automatic contact between the sample and the loading platens must be designed. Interfaces which represent physical discontinuities are created to join the two sub-grids of the loading apparatus and the specimen. The interface stiffness (expressed in stress-per-distance units) was calculated according to (Itasca 2019):

$$\max\left[\frac{(K+\frac{4}{3}G)}{\Delta z_{min}}\right] \tag{6-4}$$

where K and G are the bulk and shear moduli, respectively; Δz_{min} is the smallest width of an adjoining zone in the normal direction. For heterogeneous disc models, K and G of each element are generally in the order of 1×10^{10} Pa, while Δz_{min} is in the order of 1×10^{-3} m. For simplicity, the stiffness of the interface was calculated to be in the order of 1×10^{13} Pa/m according to Eq. (6-4). Both normal stiffness (k_n) and shear stiffness (k_s) were set to this value.
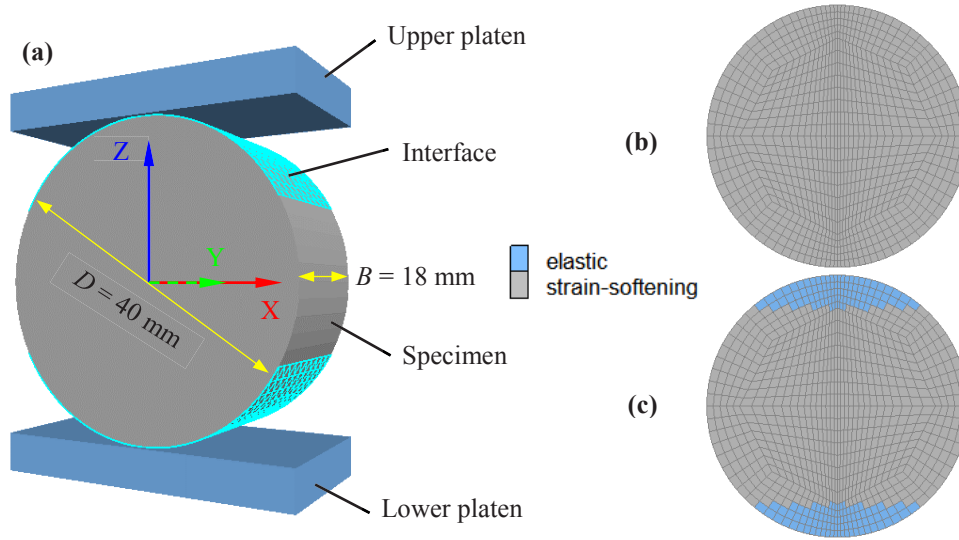
Figure 6-10 Numerical model set-up for Brazilian test

The simulation results of homogeneous samples with an input tensile strength of 12.8 MPa are shown in Figure 6-11. For the strain-softening disc (Figure 6-11a), both shear and tensile failure occur, while the elastic-strain-softening model (Figure 6-11b) only shows tensile failure. The simulated tensile strength according to Figure 6-11a is 12.1 MPa, which is lower than the input value of 12.8 MPa of the sample shown in Figure 6-11b. This proves that the shear failure at the load entry areas can really influence the tensile strength. Considering the fact that the heterogeneous distribution of mineral properties could result in a strength reduction (see section 6.3), the input values of tensile strength for heterogeneous models should be back-calculated based on lab test results.

According to lab tests Young's modulus, UCS, and Poisson's ratio of Laurentian granite are 92 GPa, 259 MPa, and 0.21 (Yin et al. 2015), respectively. According to chapter 6.3.1, the shear input parameters should be higher than the lab results in the heterogeneous models. Because the friction angle φ is usually temperature-independent and has negligible effect on the thermo-mechanical behavior (Wang and Konietzky 2019), the input value φ_0 is set to u_x^φ as documented in Table 6-6. Subsequently the input Young's modulus E_0 and cohesive strength c_0 at room temperature can be back-calculated as documented in Table 6-6. The uniaxial compression result of the calibrated model at room temperature (25 °C) is shown in Figure 6-12a. Both, UCS and Young's modulus are nearly the same as those obtained from lab tests. Figure 6-12b shows the

Brazilian test result of the heterogeneous model with calibrated parameters (see Table 6-6), which is in a good coincidence with the lab test value.
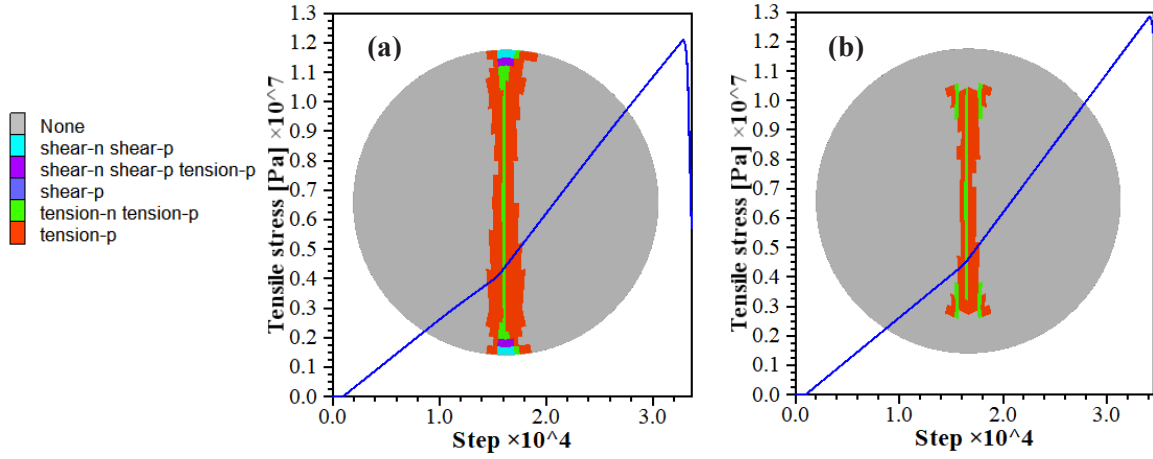
Figure 6-11 Brazilian tests of homogeneous (a) and inhomogeneous (b) model

(a) Uniaxial compression test   (b) Brazilian test
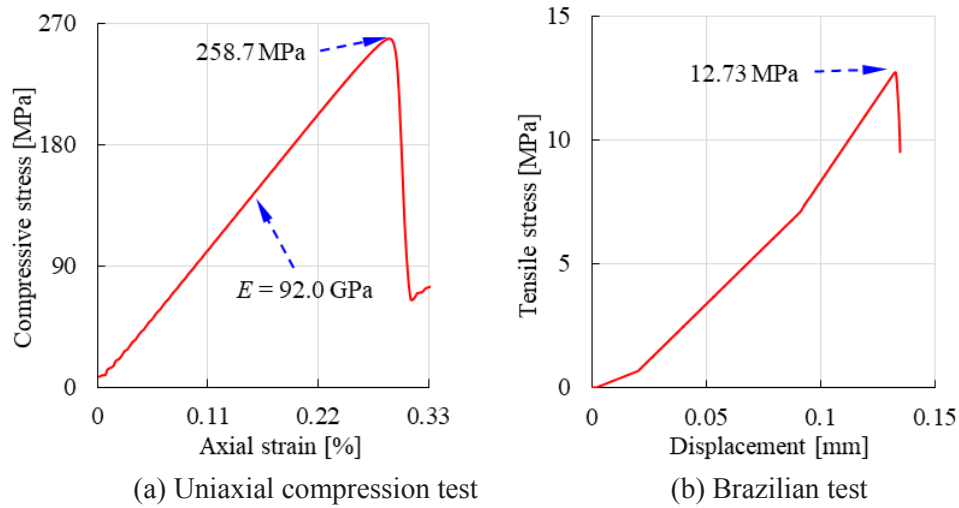
Figure 6-12 Mechanical test results of calibrated inhomogeneous model at room temperature

6.4.2 Temperature-dependent parameters

The volumetric thermal expansion coefficient β_t at 100 °C, 250 °C, 450 °C, 600 °C and 850 °C were determined in the laboratory (Yin et al. 2015). After the first increase at 573 °C, the thermal expansion of Laurentian granite experienced a second increase at 850 °C. This is in consistence with the findings from Hartlieb et al. (2016). Based on the lab data and the equations given in the

previous work (Wang and Konietzky 2019), the temperature-dependent linear thermal expansion coefficient is deduced as shown in Figure 6-13a. Thermal conductivity of dry granite at room temperature usually varies from 2 W/m°C to 3 W/m°C (Dwivedi et al. 2008; Zhao et al. 2018), and we set k_0 = 2.5 W/m°C in this model. The tensile strength obtained from lab tests at different temperatures are converted into normalized form (see Figure 6-13c), so that we can assign the element properties based on the deduced tensile strength (see Table 6-6).

(a) Linear thermal expansion coefficient   (b) Density   (c) Normalized tensile strength
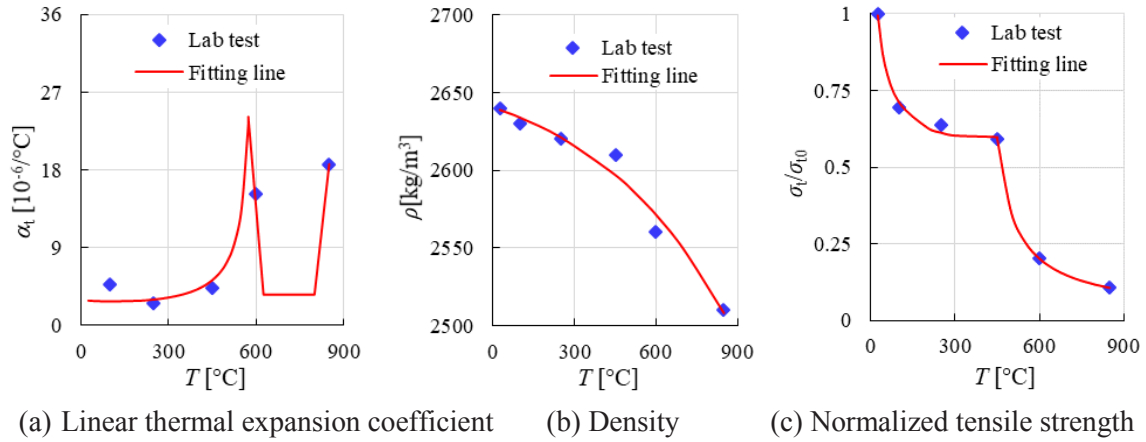
Figure 6-13 Lab test parameters and corresponding fitting lines

In the simulations, the thermal treatment was conducted with a heating rate of 2 °C/min until the target temperatures of 100 °C, 250 °C, 450 °C, 600 °C, and 850 °C are reached. As soon as the temperature reached the target values at the outer boundary, the temperature is maintained until reaching a uniform temperature inside the whole sample. Except for the relations in Figure 6-13, all the other temperature-dependent parameters follow the general equations given in section 2.2. Friction angle and dilation angle are set to be heterogeneous and temperature-independent. They follow the same softening law as shown in Figure 6-4, while the cohesion softening relations are taken from Figure 5-19. Heated granite becomes more ductile and the tensile deformation at failure varies with temperature. Experimental evidences indicate that strain softening is not a material property of rocks treated as continua, but rather the heterogeneity and brittleness caused by progressively distributed damage, such as dispersed microcracks, deterioration of material and loss of interparticle contacts (Li et al. 2017; Vignjevic et al. 2018). Since temperature can induce damage to the sample, the softening relations of granite strengths should be temperature dependent.

The softening relations for tensile strength of Laurentian granite at elevated temperatures are back-calculated from the lab test results and plotted in Figure 6-14.
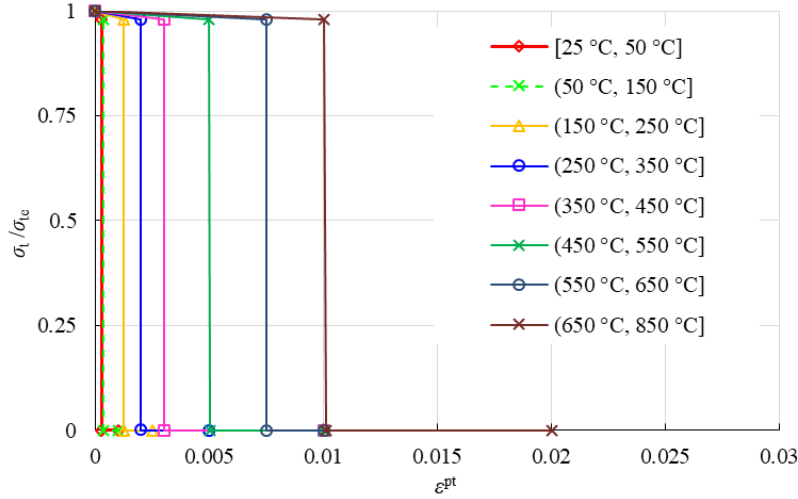
Figure 6-14 Variation of softening parameters with plastic tensile strain ε^{pt} [mm/mm]. The subscript 'e' means the property at $\varepsilon^{pt} = 0$

6.4.3 Thermal induced cracking

Lin (2002) measured the permanent strain of thermal expansion, compressional wave velocity, and density of microcracks of Inada granite, implying the cumulative amount of newly generated microcracks and the opening of pre-existing microcracks appeared distinctly at a temperature between 100 °C and 125 °C and increased almost exponentially in the range from 200 °C to 573 °C. Vázquez et al. (2015) concluded that 130 °C is a threshold for microcrack development, while 400 °C is the lowest temperature to produce damage visible under the microscope. By using AE monitoring and SEM, Chen et al. (2017a) found that 300 °C and 573 °C are two temperature thresholds for thermal cracking based on the emergence of a large number of AE hits around 300 °C and remarkable drop of b-value according to the Gutenberg-Richter-Relation at around 573 °C. What the authors did not mention is that, actually AE hits started already between 100°C to 200 °C and we can also see some new microcracks in the SEM image at 200 °C. This means microcracks start to occur between 100 – 200 °C, but become more obvious at about 300 °C. Zuo et al. (2017) conducted three-point bending tests on Beishan granite with thermal treatment and SEM observation, and numerous thermal microcracks were observed on the surface of granite pre-treated at the temperature of 125 – 200 °C. When pre-treatment temperature is higher than 300 °C, deep

and long cracks appeared. Optical microscopic observations of Yang et al. (2017) showed that no obvious microcracks were observed at 200 °C, but microcracks have propagated across most grains with an obvious increase in crack quantity and width at about 600 °C. Zhao et al. (2018) presented SEM images of Beishan granite after thermal treatment. Compared with the result at 105 °C some microstructural alterations can be observed at 200 °C. They also found that the maximum widths of observed microcracks in the specimens treated with 300 °C and 400 °C are generally < 2 μm, while increasing significantly at 550 °C (4 μm) and 650 °C (8 μm). Zhao (2016) used a particle-based method to simulate the process of thermal induced micro- and macrocracks in granite. They found that during the heating process sparsely distributed microcracks occurred after the temperature has reached 200 °C, with number of microcracks continuously increasing when temperature is rising from 200 to 400 °C. Therefore, we can conclude that generally thermal microcracks of granite begin to occur between 100°C to 200 °C, and then develop continuously at higher temperatures.

The results of the ultrasonic P-wave velocity test (Yin et al. 2015) are consistent with the general trend of thermal crack development mentioned above. For Laurentian granite, P-wave velocity is not sensitive up to 100 °C, but decreases continuously beyond 100 °C (see Figure 6-15). This trend can be explained by the increase in the number and width of the thermal induced microcracks. The simulation results substantiate this interpretation of lab test results. The number of failed elements, which can be interpreted as microcracks, show a reverse tendency compared to the evolution of P-wave velocity (see Figure 6-15). The quantity of induced cracks experiences the largest increase from 100 °C to 250 °C, but the P-wave velocity does not show the greatest decrease in this temperature range. This is because the reduction of P-wave velocity is influenced by both, crack number and width. Although a great amount of cracks is induced at lower temperatures (e.g. 250 °C), the plastic tensile strain, which is proportional to the thermal induced crack width, is still very small (see Figure 6-16). The sharpest P-wave velocity decrease occurs between 450 °C to 600 °C where α-β quartz transition happens at 573 °C. In this temperature range, quantity (see Figure 6-16a) and width (see Figure 6-16b) of thermal cracks increase strongly because of the rise of the thermal expansion coefficient at 573 °C.

All in all, the Weibull-mineral based model can well reproduce the cracking behavior of granite at elevated temperature, and the good agreement with lab tests indicate the effectiveness of the proposed methodology.
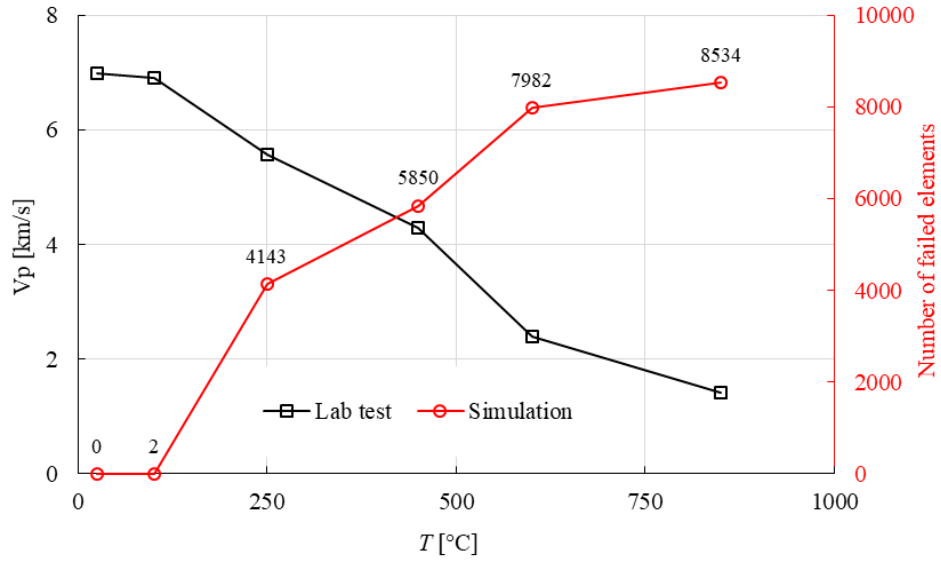
Figure 6-15 Variation of P-wave velocity and number of failed elements at different temperatures
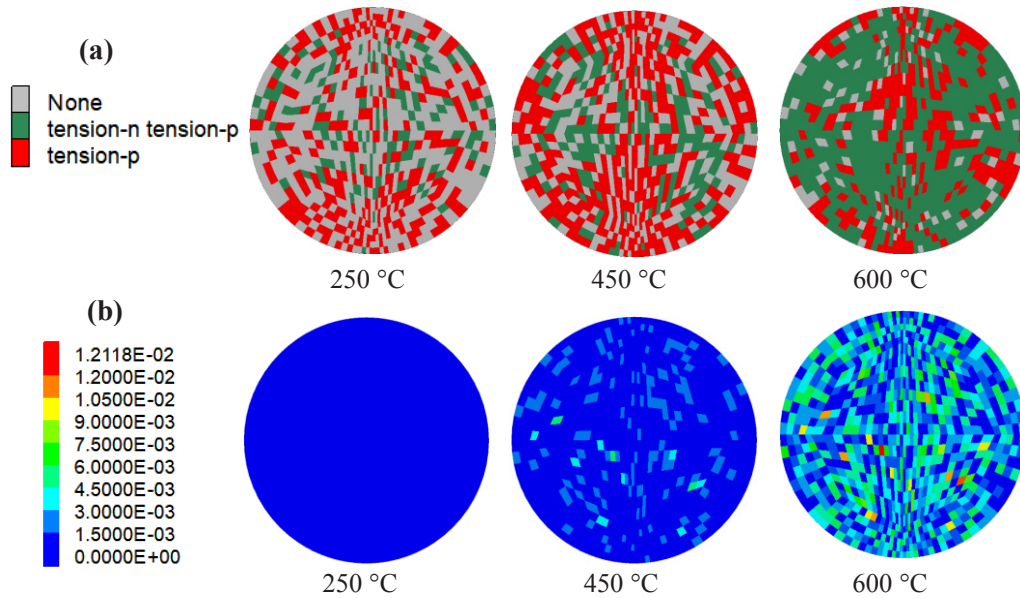
Figure 6-16 Granite disc at different temperatures. a plasticity states. b plastic tensile strain

6.4.4 Tensile strength after heat treatment

After heat treatment, a Brazilian test with flat platens is conducted. The comparison between lab testing and simulation is presented in Figure 6-17, which documents a very close agreement. A noticeable phenomenon is that the tensile strength experiences a significant decrease at 600 °C and 850 °C, which is attributed to the crack development with heating. As a result, the granite sample at 850 °C has been highly damaged by thermal treatment (Yin et al. 2015). Therefore, the Weibull-mineral based model can well reproduce and interpret thermo-mechanical behaviors of granite at various temperatures
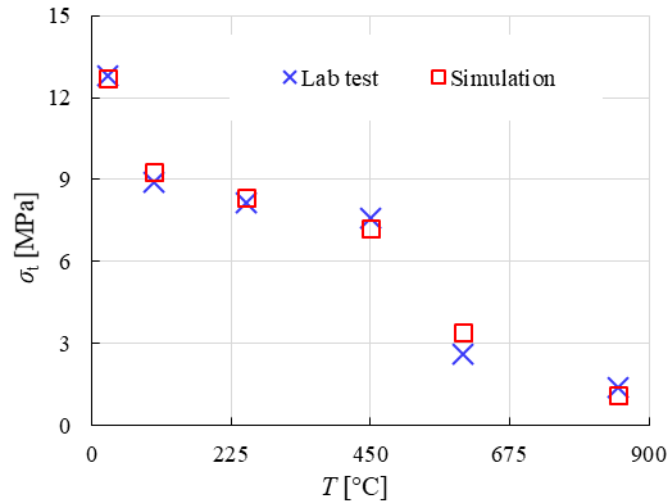
Figure 6-17 Variation of tensile strengths after heating-up to different temperatures

7 Numerical simulation of Eibenstock granite

The constitutive model developed in Chapter 5 and the Weibull-mineral based method proposed in Chapter 6 were implemented into the code FLAC^{3D} to simulate the thermal induced damage of EG at high temperatures. The corresponding thermo-mechanical properties obtained from slow heating tests were assigned to the elements (grains) accordingly.

In chapter 7.1 the thermal induced damage of granite after heat treatments with slow heating rate (5 °C/min) is described. Both, lab tests and simulations show that macrocracks which can be observed by the naked eye are induced at about 1000 °C. Although these cracks are isolated, they interact, and they are widespread across the whole sample. Microcracks induced by thermal stress occur much earlier at a threshold temperature of about 80 °C. Thermal cracking increases progressively after 80 °C and the preponderance of newly formed cracks (more than 80 % in amount) are created below the quartz transition temperature of 573 °C. These microcracks are randomly generated across the whole sample. Although most thermal induced damages are tensile failures, shear failure begins to develop quickly beyond 500 °C and becomes significant thereafter. UCS reduction of granite during heating is mainly caused by increasing shear failure. This also explains why in the lab tests the most dominant UCS reduction is observed after treatment at 600 °C. The simulation results also indicate that the dominant impact of α-β quartz transition is widening of pre-existing cracks rather than the formation of new microcracks.

In chapter 7.2 the simulation of high-speed heating scenarios (including ISO834 fire curve) of EG at elevated temperatures without cooling is illustrated. Stress-strain curves with different heating scenarios show that the maximum temperature has the dominant impact on the strength of granite samples while the influence of heating rates is relatively small. This is in agreement with the lab testing results. The negligible influence of heating rates on mechanical properties is related to the different cracking structure on the surface and inside of the granite samples.

7.1 Simulations of EG after heat treatment with slow heating rate

7.1.1 Geometry and boundary conditions

A cylindrical sample (Figure 7-1a) with a radius of 25 mm and a length of 110 mm is created in FLAC^{3D}. The corresponding Brazilian disc with a diameter of 50 mm and a thickness of 25 mm is shown in Figure 7-1b. Cylinder and disc consist of 21,600 and 16,128 elements, respectively. The heat flux is applied to all surfaces of the samples. Cylindrical sample and Brazilian disc are fixed at the bottom in XY and XZ planes which are perpendicular to gravity directions during the heating process. The heating rate is the same as during the lab tests (i.e. 5 °C/min) (see section 4). Once the target temperature is reached, the sample is continuously kept at target temperature until the temperature is uniformly distributed across the whole sample. The reduction in mechanical properties during slow heating–cooling cycles appears to be relatively small compared to continuous heating, and little structural damage occurs during the cooling phase of a thermal cycle (Johnson et al. 1978; Wang et al. 1989; Shao et al. 2014; Griffiths et al. 2018). Therefore, we assume that the influence of slow cooling can be neglected. The thermal option is switched off to simulate the mechanical loading up to failure at room temperature.
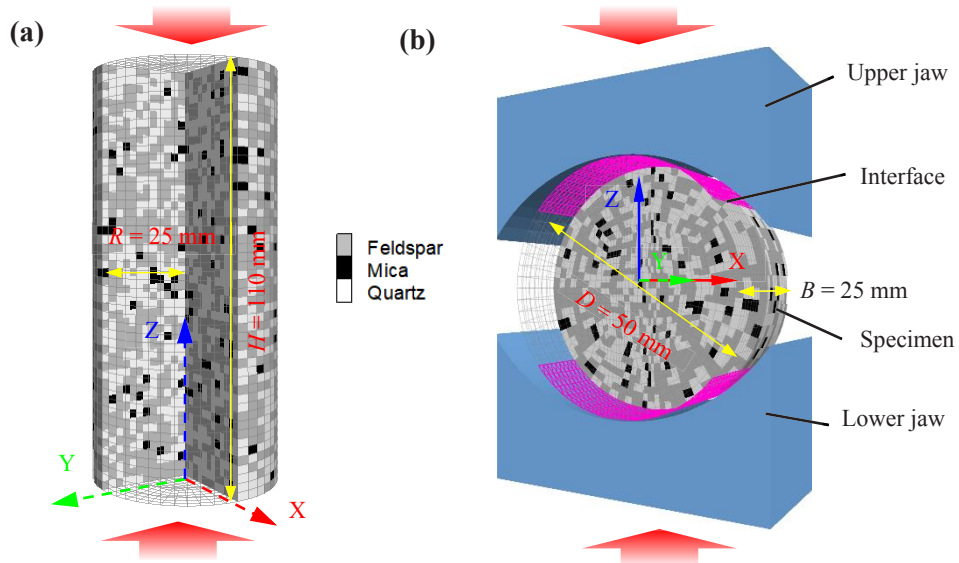
Figure 7-1 Numerical model set-up.

During the uniaxial compression test, a low velocity (1×10^{-8} m/s) is applied at the bottom and top of the cylindrical sample (see Figure 7-1a). A lower velocity (1×10^{-9} m/s) is applied at the upper and lower jaws during Brazilian tensile test (see Figure 7-1b). The radius of jaws is $1.5 \times$ specimen radius and the width of jaws is $1.1 \times$ specimen thickness (ISRM 1978). The loading jaws are elastic with a bulk and shear modulus of 160 GPa and 80 GPa, respectively. Interfaces are also created to join the two sub-grids of the loading apparatus and the specimen to simulate an automatic contact during the loading process (see Figure 7-1b). The initial normal stiffness (k_n) and shear stiffness (k_s) of the interfaces are set as 1×10^{14} Pa. The model elements are divided into feldspar, quartz and mica randomly, and the mineral proportions are 50%, 44%, and 6% respectively. The corresponding Weibull parameters are calculated (see chapter 6) and documented in Table 7-1.

Table 7-1 Mineral properties and corresponding Weibull parameters (Wang et al. 2020)

Parameters	α_t $(10^{-6}/K)$	C_v (J/kg K)	k (W/m K)	E (GPa)	φ (°)	c (MPa)	v	σ_t (MPa)	ρ (kg/m³)
m	2.7	16.8	1.8	4.2	8.3	7.7	12.1	12.7	25.8
x_0	1.12	1.03	1.12	1.1	1.05	1.06	1.04	1.04	1.02

7.1.2 Temperature-dependent parameters

Based on the lab tests described in chapter 3.2 and 4.2, the EG properties at room temperature and the normalized equations of temperature-dependent properties are obtained and documented in Table 7-2 and Table 7-3, respectively.

Table 7-2 Model parameters at room temperature

Parameters	P_0
Coefficient of linear thermal expansion α_{t0} [1/K]	4.94×10^{-6}
Specific heat C_{v0} [J/kgK]	706
Thermal conductivity k_0 [W/mK]	3.65
Young's modulus E_0 [GPa]	27.38
Poisson's ratio v_0	0.26 (Tan et al. 2016)
Tensile strength σ_{t0} [MPa]	10.0
Cohesion c_0 [MPa]	25.5 (Tan et al. 2016)
Friction angle φ_0 [°]	53.7 (Tan et al. 2016)
Density ρ_0 [kg/m³]	2604

The model is based on a strain-softening constitutive law, in which cohesion c and tensile strength σ_t soften after the onset of plastic yield. The softening behavior for cohesion and tension are provided by user defined functions in the form of tables and each table contains pairs of values: one for the plastic strain, and one for the corresponding property value (Itasca 2019). In this work, the table relating tension limit to plastic tensile strain is $(0, \sigma_{t0}{\cdot}x_i)$ $(\varepsilon^{t1}, \sigma_{ti}(T))$ $(\varepsilon^{t2}, 0)$, while the table relating cohesion to plastic shear strain is $(0, c_0{\cdot}x_i)$ $(\varepsilon^{s1}, 0.5c_i(T))$ $(\varepsilon^{s2}, 0.2c_i(T))$. Plastic shear strain (ε^s) and tensile strain (ε^t) of each element are defined as shown in Figure 7-2. Based on Table 7-1, Table 7-2, Table 7-3, and Figure 7-2, the properties of granite samples are assigned to corresponding mineral grains.

Table 7-3 Temperature dependent property equations

Property of element i	Temperature-dependent equation (in normalized form)
$\rho_i(T) = \rho_0{\cdot}x_i{\cdot}f_{\rho t/\rho 0}$	$f_{\rho/\rho_0} = 1.00191/(1+e^{-6.484+0.0048T}),\ 0{}^\circ\text{C} < T \le 1000{}^\circ\text{C}$
$E_i(T) = E_0{\cdot}x_i{\cdot}f_{E/E0}$	$f_{E/E_0} = 1/(1+e^{-6.250714+0.010708T}),\ 0{}^\circ\text{C} < T \le 1000{}^\circ\text{C}$
$\sigma_{ti}(T) = \sigma_{t0}{\cdot}x_i{\cdot}f_{\sigma t/\sigma t0}$	$f_{\sigma_t/\sigma_{t0}} = 1-1.182T^{3.115}/(608.213^{3.115}+T^{3.115}),\ 0{}^\circ\text{C} \le T \le 1000{}^\circ\text{C}$
$v_i(T) = v_0{\cdot}x_i{\cdot}f_{v/v0}$ [-]	$f_{v/v_0} = \begin{cases} -7\times10^{-4}T+1.0052,\ 0{}^\circ\text{C} \le T \le 600{}^\circ\text{C} \\ 2.240/(1+e^{13.11-0.020T}),\ 600{}^\circ\text{C} < T \le 800{}^\circ\text{C} \end{cases}$
$c_i(T) = c_0{\cdot}x_i{\cdot}f_{c/c0}$	$f_{c/c_0} = \begin{cases} 0.003T+0.9933,\ 0{}^\circ\text{C} \le T \le 400{}^\circ\text{C} \\ 1\times10^{-6}T^2-0.0008T+1.606,\ 400{}^\circ\text{C} < T \le 800{}^\circ\text{C} \\ -0.0012T+1.22,\ 800{}^\circ\text{C} < T \le 1000{}^\circ\text{C} \end{cases}$
$\alpha_{Ti}(T) = \alpha_{T0}{\cdot}x_i{\cdot}f_{\alpha T/\alpha T0}$	$f_{\alpha_t/\alpha_{t0}} = \begin{cases} (2.5138-0.00039T)/(1-0.0025T+1.324\times10^{-5}T^2),\ 0{}^\circ\text{C} < T \le 573{}^\circ\text{C} \\ 1/(198.23327-0.690845T+6.01976\times10^{-4}T^2),\ 573{}^\circ\text{C} < T \le 600{}^\circ\text{C} \\ 4.3797+2.3956\cos(0.00905T-2.798),\ 600{}^\circ\text{C} < T \le 887{}^\circ\text{C} \\ 22.731979+18.773112\cos(0.02618T-0.826438),\ 887{}^\circ\text{C} < T \le 980{}^\circ\text{C} \\ 991.42-0.97T,\ 980{}^\circ\text{C} < T \le 1000{}^\circ\text{C} \end{cases}$
$C_{vi}(T) = C_{v0}{\cdot}x_i{\cdot}f_{Cv/Cv0}$	$f_{C_v/C_{v0}} = \begin{cases} 0.0005T+0.9856,\ 0{}^\circ\text{C} \le T \le 600{}^\circ\text{C} \\ 1.27,\ 600{}^\circ\text{C} < T \le 1000{}^\circ\text{C} \end{cases}$
$\lambda_i(T) = \lambda_0{\cdot}x_i{\cdot}f_{k/k0}$	$f_{\lambda/\lambda_0} = 0.174+0.897\times0.9963^T+0.00013T,\ 0{}^\circ\text{C} \le T \le 1000{}^\circ\text{C}$

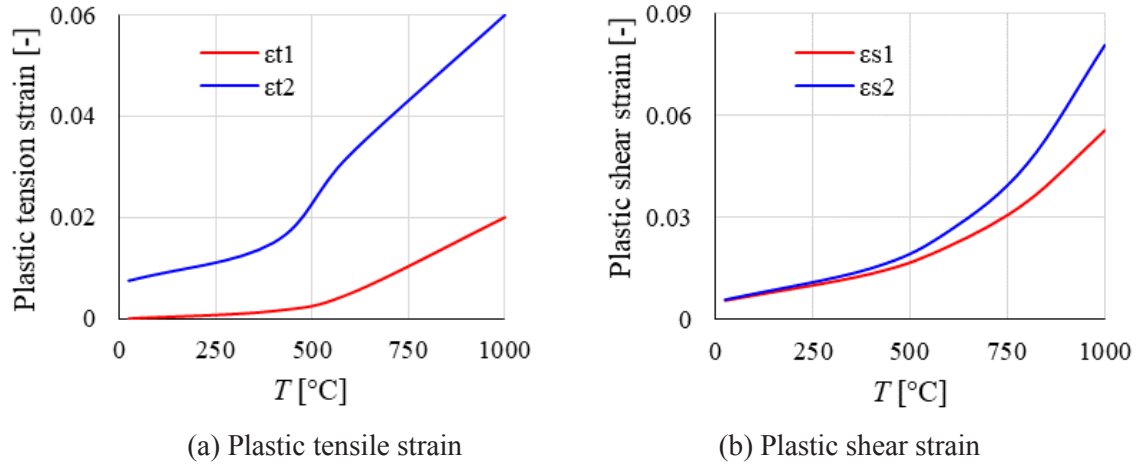(a) Plastic tensile strain   (b) Plastic shear strain

Figure 7-2 Temperature-dependent parameters for softening tables

Exemplary, Figure 7-3 illustrates the distribution of tensile strength and linear thermal expansion coefficient of different mineral grains at room temperature.
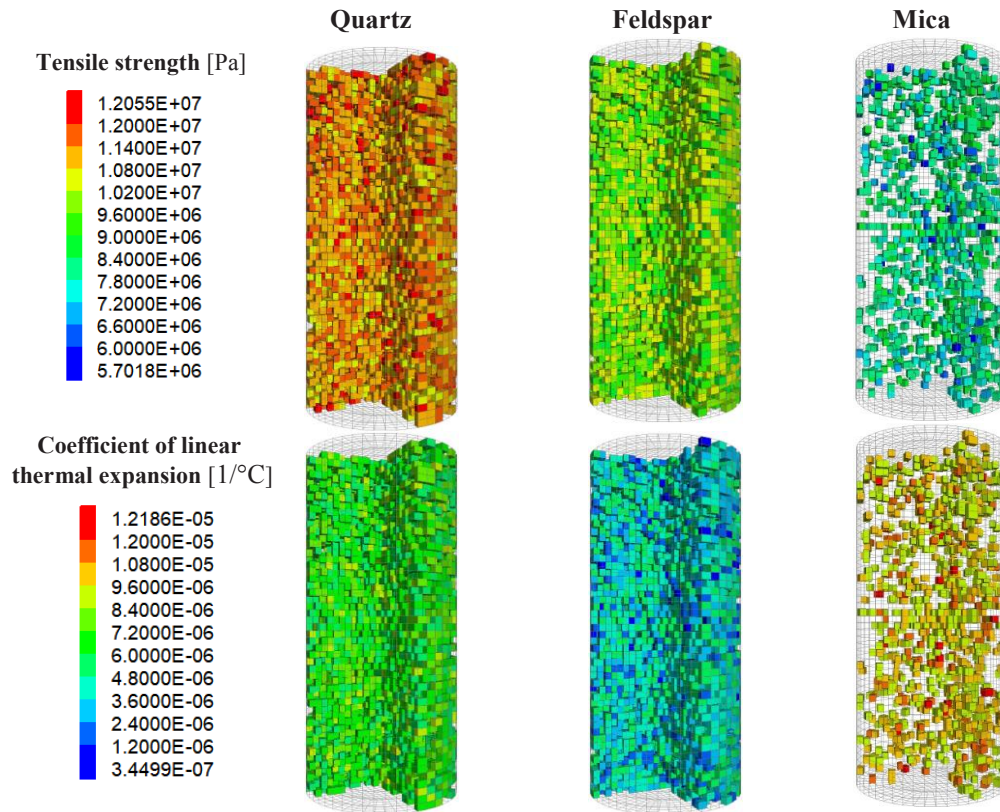
Figure 7-3 Property distributions of different minerals at room temperature

Since the dominant variation of thermal expansion coefficient of granite is caused by the *α-β* quartz transition, which will lead to significant volumetric expansion (Nordlund et al. 2014; Polyakova 2014), the expansion coefficient of quartz grains follows the temperature-dependence given in Table 7-3. Considering that the proportion of mica is very small (only 6%) and that the thermal expansion coefficients of some micas can become extraordinary high around 600 °C (Hidnert and Dickson 1945), the thermal expansion coefficient of mica also follows the equation given in Table 7-3 for simplicity. The thermal expansion variation of feldspars is relatively small and experiences an increase by a factor of 1.7 in the temperature range from 298 *K* to 900 *K* (Tribaudino et al. 2010; Nordlund et al. 2014). This trend is implemented in the numerical model as temperature-dependent expansion coefficient for feldspar.

7.1.3 Simulation results

7.1.3.1 Thermal induced cracks

Before mechanical loading, no obvious cracks caused by thermal stresses are observed directly in the temperature range between 25 °C and 800 °C. However, samples experienced 1000 °C heat treatment show obvious macrocracks which can be observed by the naked eye (see Figure 7-4a and c). Although these cracks appear isolated, they interact with each other, and they are widespread across the whole sample. In a continuum numerical model, the macrocracks can be represented by a certain value of plastic strain (see Figure 7-4b and d). It is visible that the crack patterns of the simulations are in good agreement with the lab test observations in terms of macrocracks, if a strain value of about 0.09 is interpreted as macroscopic crack.

Although the macrocracks are only visible above certain temperatures, change in P-wave velocity and open porosity (Figure 4-11) indicates that microracks induced by thermal stresses occur much earlier. Johnson et al. (1978) has also found that thermal cracking occurs when a certain threshold temperature is exceeded, which is different for different rocks (e.g. 75 °C for Westerly granite and 200 °C for Sioux quartzite). They also found that thermal cracking increases progressively after threshold temperature and the preponderance of cracking occurs below the quartz transition temperature of 573 °C. This trend is also observed in our simulations.

Figure 7-5 shows the variation of P-wave velocity (lab testing) and the number of failed elements (i.e. element with plasticity states) at different temperatures in the simulation. Failed elements can be interpreted as thermally induced microcracks. Their evolution in time shows a reverse tendency compared to the development of P-wave velocity. The quantity of induced cracks is increasing with increasing temperature and more than about 80% of the cracks are induced before 600 °C. Figure 7-6 shows the plasticity states (i.e. microcracks) and plasticity tensile strain (cracks with certain widths) on the axial plane of the cylindrical sample. The crack initiation temperature is about 80 °C with a few randomly induced microcracks across the sample. The element failures begin to occur progressively after the threshold temperature. Most elements fail in tension in the temperature range from 80 °C to 1000 °C. However, at about 500 °C shear failure begins to develop quickly with increasing temperature (see Figure 7-6a).

(a) Crack pattern of a cylindrical sample in lab   (b) Failure pattern (plastic-tension-strain) in simulation

(c) Crack pattern of a Brazilian disc in lab   (d) Failure pattern (plastic-tension-strain) in simulation
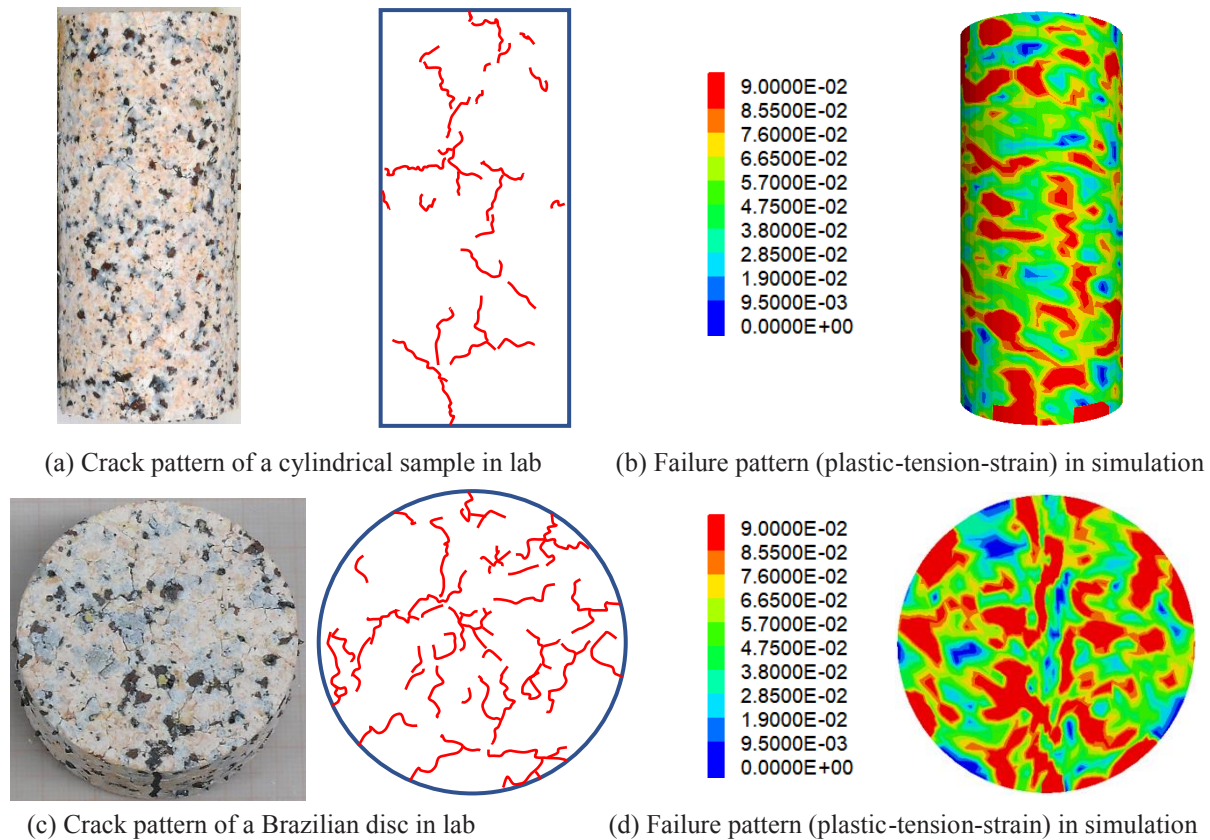
Figure 7-4 Thermal induced macrocracks of granite samples after 1000 °C heat treatment
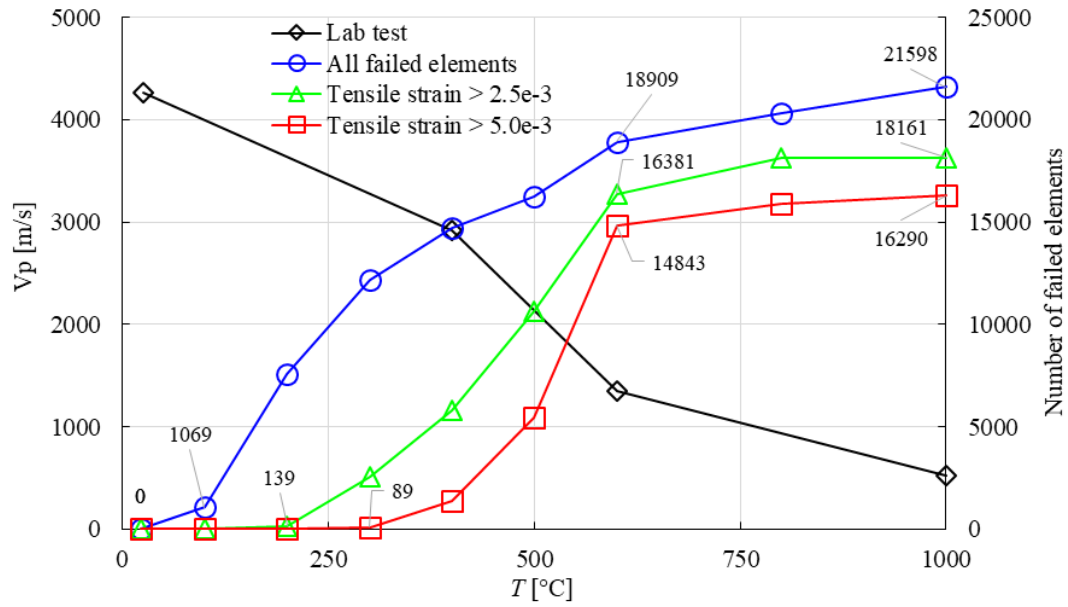
Figure 7-5 Variation of P-wave velocity and number of failed elements at different temperatures
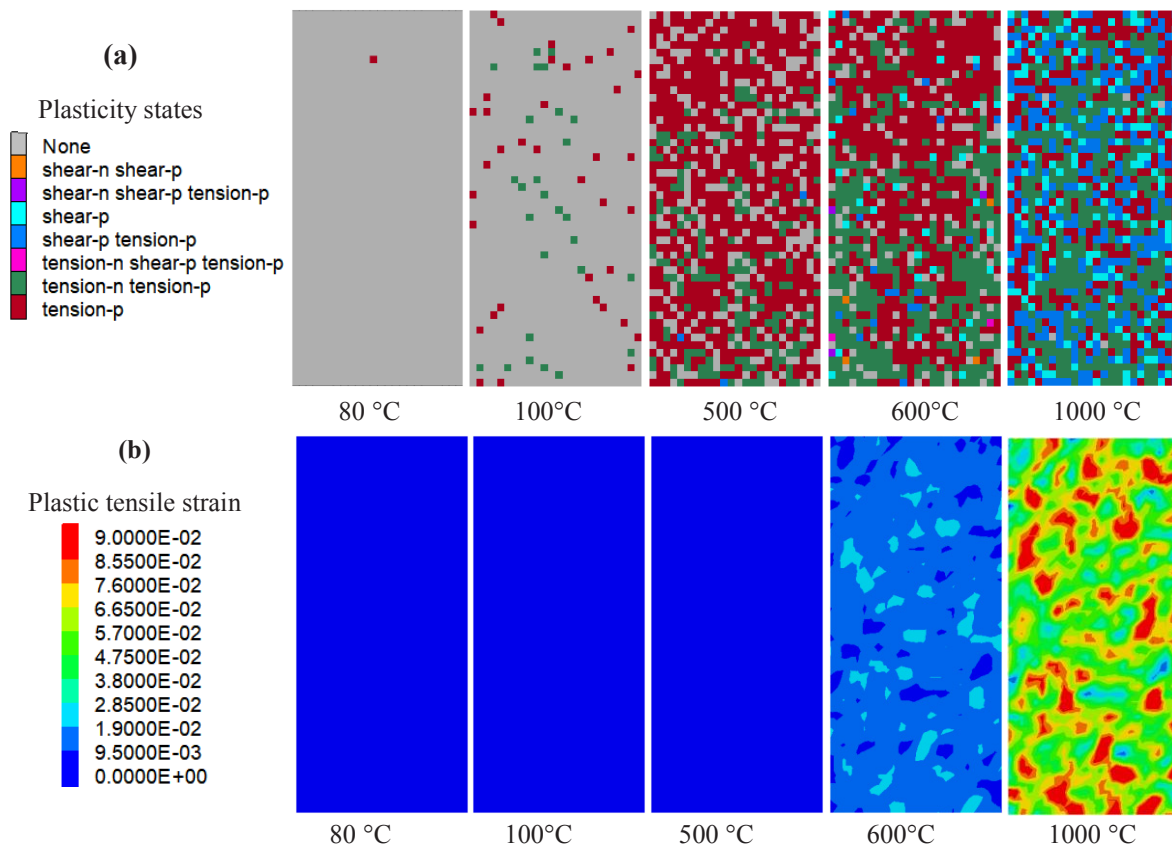

Figure 7-6 Failed elements and plastic tensile strain at elevated temperatures

Obvious macro damage cannot be observed directly with naked eyes before a certain high temperature (e.g. 1000 °C) is reached, because significant widening of the pre-induced cracks happens at higher temperatures. Lab tests have shown that below the quartz transition temperature of 573 °C, the decrease of P-wave velocity is associated with microcrack evolution, but above 573 °C, new crack formation is relatively seldom and the P-wave velocity decrease is mainly caused by the widening of earlier formed microcracks (Johnson et al. 1978; Bauer and Johnson 1979; Lin 2002). When plastic tensile strain in a failed element is bigger than 2.5e-3, the number of cracks widened by thermal stresses is much smaller than for cracks with tensile strain > 0 (see Figure 7-5). This trend becomes more obvious for cracks with tensile strain > 5e-3. Especially around 573 °C, the number of widened cracks shows the sharpest increase. After 600 °C, both, the decreasing rate of P-wave velocity and the increasing rate of number of failed elements show a simultaneous reduction. Therefore it is concluded, that the majority of newly created thermal cracks occurs in the range between 100 °C to 600 °C. The dominant impact of the α-β quartz transition is widening of pre-existing cracks rather than the formation of new microcracks.

7.1.3.2 Granite strength after heat treatment

After cooling down to room temperature, the granite samples were mechanically loaded. Figure 7-7 compares the ultimate failure modes of granite samples before and after heating as observed in lab test and numerical simulations. The comparison of the failure modes of granite without and after heating (take 1000 °C as an example) indicates a significant influence of temperature treatment on failure behavior. At room temperature, the granite shows typically brittle behavior, and the samples split into several parts. For samples heated to 1000 °C, the cylindrical samples are crushed into fine pieces producing extended shear zones rather than sharp, single failure planes. At room temperature Brazilian discs are perfectly split in two parts through a tensile fracture in the loading plane while the lateral parts of the specimen remain fairly undamaged. However, after heating to 1000 °C in addition to the main fracture which still will split the Brazilian disc into two parts, a multiple fracturing process with many minor, secondary cracks is observed (compare Figure 7-4c, d and Figure 7-7g, h). The failure modes obtained by the numerical simulations are quite similar to those documented by the lab tests. This confirms the accuracy and reliability of the proposed numerical modelling strategy.
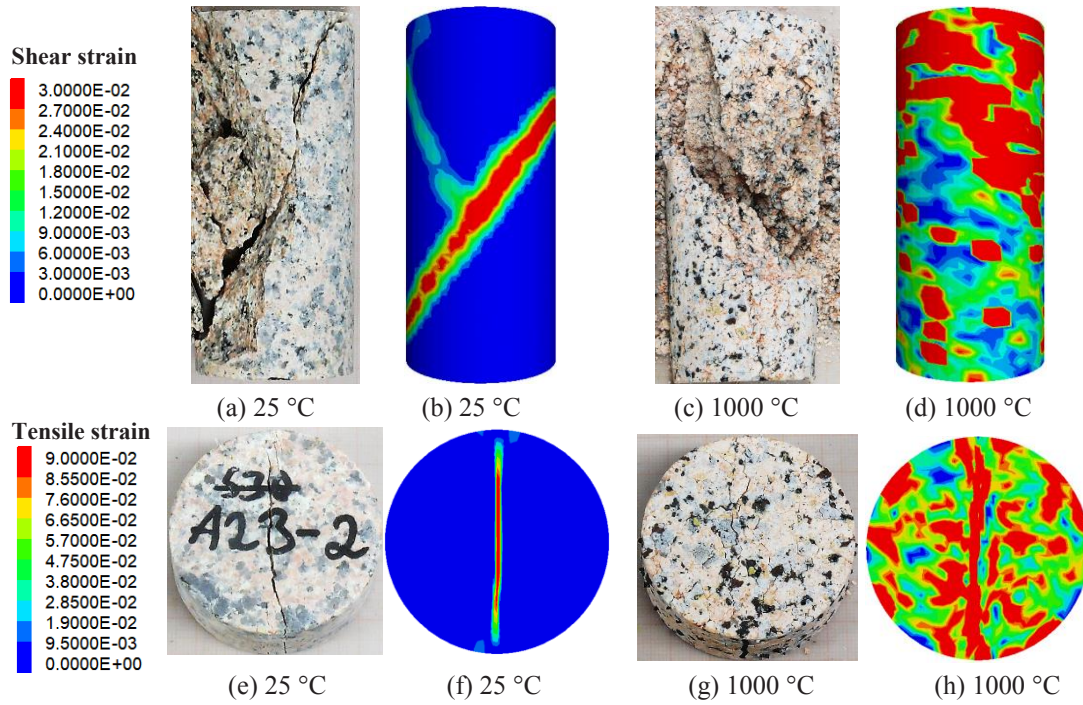
Figure 7-7 Comparison of failure patterns of specimens after mechanical tests in lab and simulation (at room temperature and after heating-up to 1000°C)

The axial stress-strain curves of cylindrical models are plotted in Figure 7-8. Before heating, the granite samples show a typical brittle stress-strain behavior. Strength and brittleness is gradually lost at elevated temperatures, especially beyond 600 °C. Samples heated-up to 800 °C and 1000 °C show a clear ductile behavior. Figure 7-9 compares uniaxial compression and tensile strength obtained by lab tests and simulations. Simulation results are consistent with the lab test results.
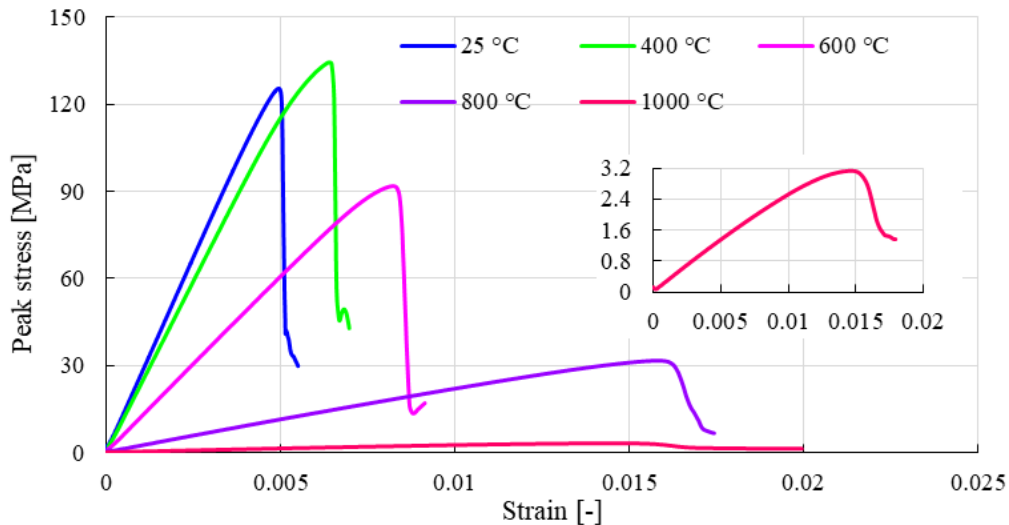
Figure 7-8 Axial stress-strain curves of uniaxial compression tests (simulations)

(a) Uniaxial compression strength
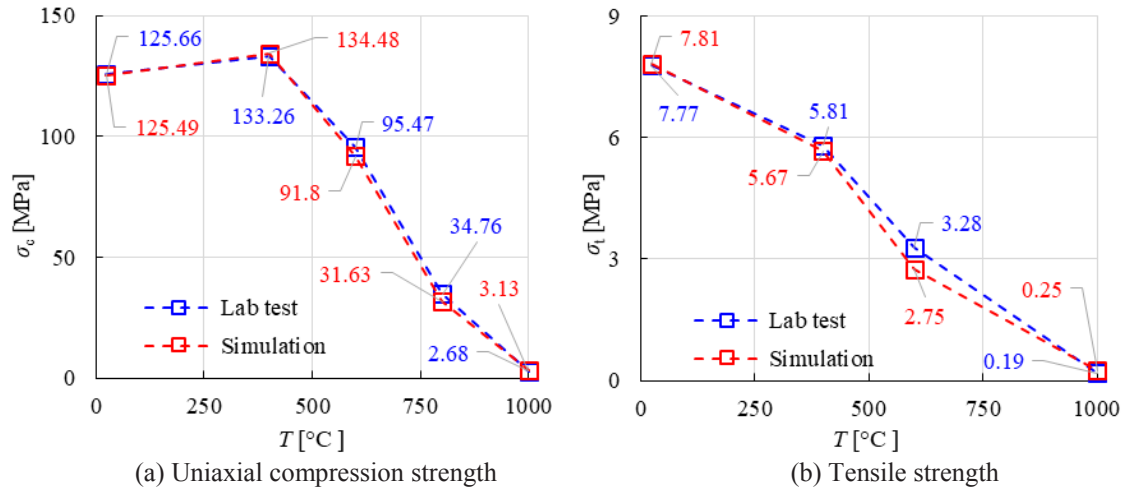
(b) Tensile strength

Figure 7-9 UCS and tensile strength measured at room temperature after heating to certain temperatures

Crack density and width show a strong increase after the threshold temperature of 80 °C (see Figure 7-5 and Figure 7-6), and the tensile strength of granite shows a decrease with increasing temperature (see Figure 7-9b). However, UCS does not show a decrease up to about 400 °C although the number of failed elements keeps increasing (see Figure 7-9a). As Figure 7-10 clearly shows, shear failure only is dominant in samples previously treated at temperatures beyond 400 °C. Therefore, the obvious UCS reduction of granite due to heating is likely to be caused by increasing shear failures to a great extent.
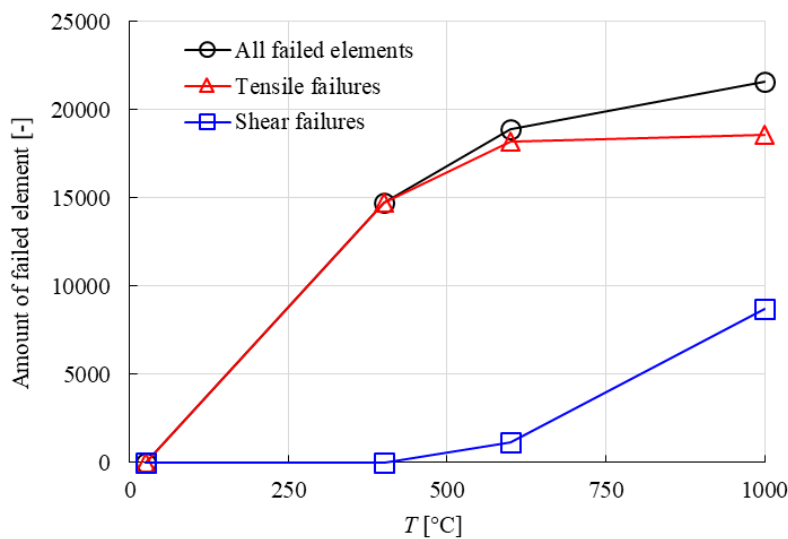
Figure 7-10 Amount of different types of failed elements at elevated temperatures

7.2 Simulations of EG considering high-speed heating

7.2.1 Influence of heating rates on mechanical properties of EG

To duplicate the lab test conditions in a simplified way (see Figure 7-11 a and c), the heat flux is applied directly to the middle part of the sample surface with a height of 66 mm (see Figure 7-11c). In lab tests, the mullite block consists of four cubes, and each cube has a dimension of $60 \times 60 \times 60$ mm. The density of mullite is about 3200 kg/m^3. The fixed stress induced by mulllite block ($\sigma_{mullite}$) is therefore applied to the top of the sample in Flac3D (see Figure 7-11c). Since compression test under temperature is very time consuming, only a quarter of sample is used in this section. The fixed boundary of the quarter of the sample is the same as in Figure 5-20.

(a) Heating device in lab testing   (b) Sketch of heating device   (c) Numerical model
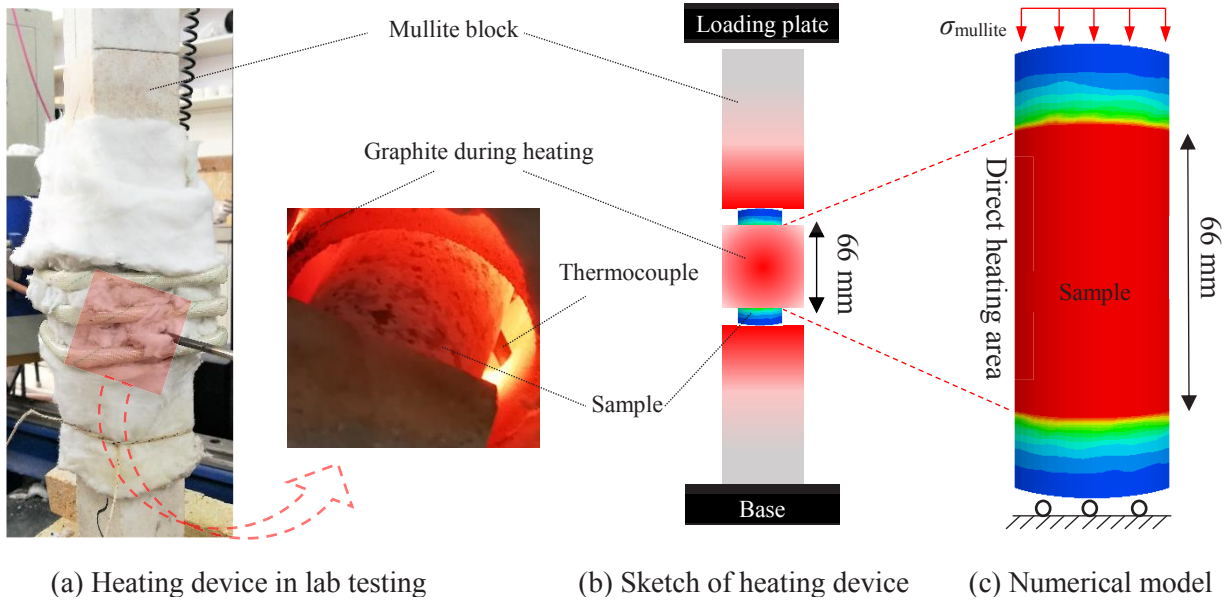
Figure 7-11 Numerical model set-up based on lab test set-up

A numerical model of EG with a radius of 25 mm and a length of 100 mm was built. Temperature-dependent parameters are the same as the EG model in section 7.1. According to the simulation results shown in Figure 7-4 and Figure 7-7, the failed elements with plastic tensile strain > 7.5e-2 or plastic shear strain > 2.5e-2 can be treated as macrocracks with large widths. Since the crack width cannot grow infinitely even under large thermal gradients (i.e. big thermal shock), thermal expansion of the element with 'macrocrack' is set to be 0. The thermal conductivity of air is

≈ 0.02 W/mK (Renteria et al. 2015) which is about 0.01 times that of the granite material. As a result, the thermal conductivity of elements with 'macrocracks' will be reduced 100 times to simulate the air condition in the 'macrocracks'.

The high-speed heating results have shown that the influence of heating rate on overall strength is relatively small compared with the influence of maximum temperature (see chapter 3.1). Although the thermo-couple was designed to detect the surface temperature of the sample in lab testing, the contact of thermocouple and graphite is not avoidable (see Figure 7-11a). This means the temperature obtained is significantly influenced by the graphite which has a much higher temperature than the sample surface temperature. Moreover, the heat insulation cotton cannot guarantee a thermal insulation effect as good as in an oven. Consequently, the sample surface temperature is actually lower than the target temperature. This means the strengths obtained at, for example 800 °C, are actually the values at a lower temperature (e.g. 650 °C). In addition, the deformation of single mullite cubes and the contact among connected cubes during load transmission can also influence the accuracy of uniaxial compression results. The absolute values of tested properties (especially the deformation) would be different from the properties obtained without mullite cubes (or real properties) to some extent. This difference does not influence the conclusion obtained from lab test since all the tests were conducted under the same loading condition, but it can produce difficulties in numerical simulations.

In numerical simulations, these external factors cannot be reproduced. Therefore, a series of heating scenarios with target temperature of 600, 700, and 800 °C applying heating rates of 5, 25, 50, 100, 200, 300 °C/min are designed to find out the most possible surface temperature for sample at 800 °C in lab testing. As in lab testing, the uniaxial compression tests were conducted at target temperatures after 1 h holding time.

Figure 7-12 shows the simulation results of stress-strain curves applying different heating scenarios. The characteristic of the simulation results, i.e. the maximum temperature has the dominant impact on the strength of granite sample while the influence of heating rates is negligible, is in good agreement with the lab test results (see chapter 3). We can also deduce that the real surface temperature of the samples with 800 °C target temperature is around 700 °C.
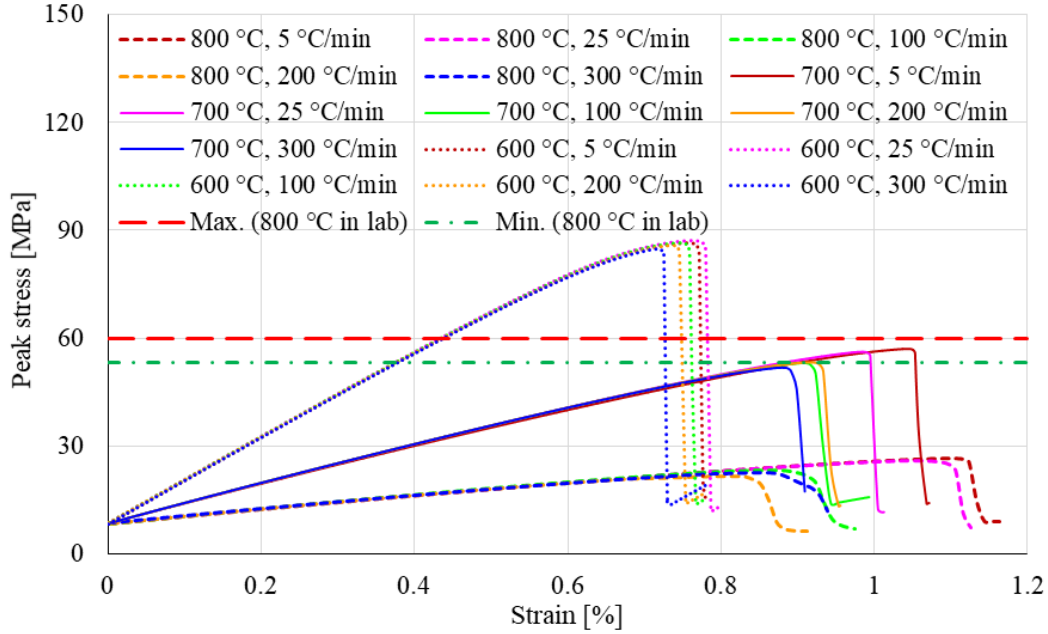
Figure 7-12 Simulated stress-strain curves applying different heating scenarios

The negligible influence of heating rates on mechanical properties such as UCS is related to the different cracking structure on the surface and inside of the granite sample. When heated to 700 °C (i.e. 800 °C in lab test), the high-speed heating causes several significant tensile-cracks due to large temperature gradients (see Figure 7-13d and e), while the slow heating rate leads to a more homogenous tensile crack distribution across the whole sample (see Figure 7-13b). Another difference is that almost no shear failures can be observed inside the samples experienced high speed heating of 300 °C/min (see Figure 7-13f), while slow heating rates can lead to a large number of shear failures throughout the sample (see Figure 7-13c). After 1 hour holding time at 700 °C (i.e. 800 °C in lab test), the cracks in sample with 300 °C/min heating become more developed and some shear failures also appear inside (Figure 7-14). The change of sample with 5 °C/min heating during the hodling stage is relatively small.

Therefore, the speed of heating can influence the crack pattern significantly. However, the combined effect of tensile and shear microcracks could be the reason for the relatively small difference in overall strength and stiffness. Moreover, the situation is even more complicated in reality since the crack distribution also influences the heat conduction (Clauser and Huenges 1995; Kumari et al. 2017a). Considering some other factors like maximum temperature, sample size, material properties, cooling method (e.g. furnace, air, or water cooling) etc., the crack pattern will

be even more complicated. Nevertheless, the small strength variation in respect to different heating rates is caused by a different induced crack patterns.

(a) Temperature [°C]　　　　(b) Tensile strain　　　　(c) Shear strain

(d) Temperature [°C]　　　　(e) Tensile strain　　　　(f) Shear strain
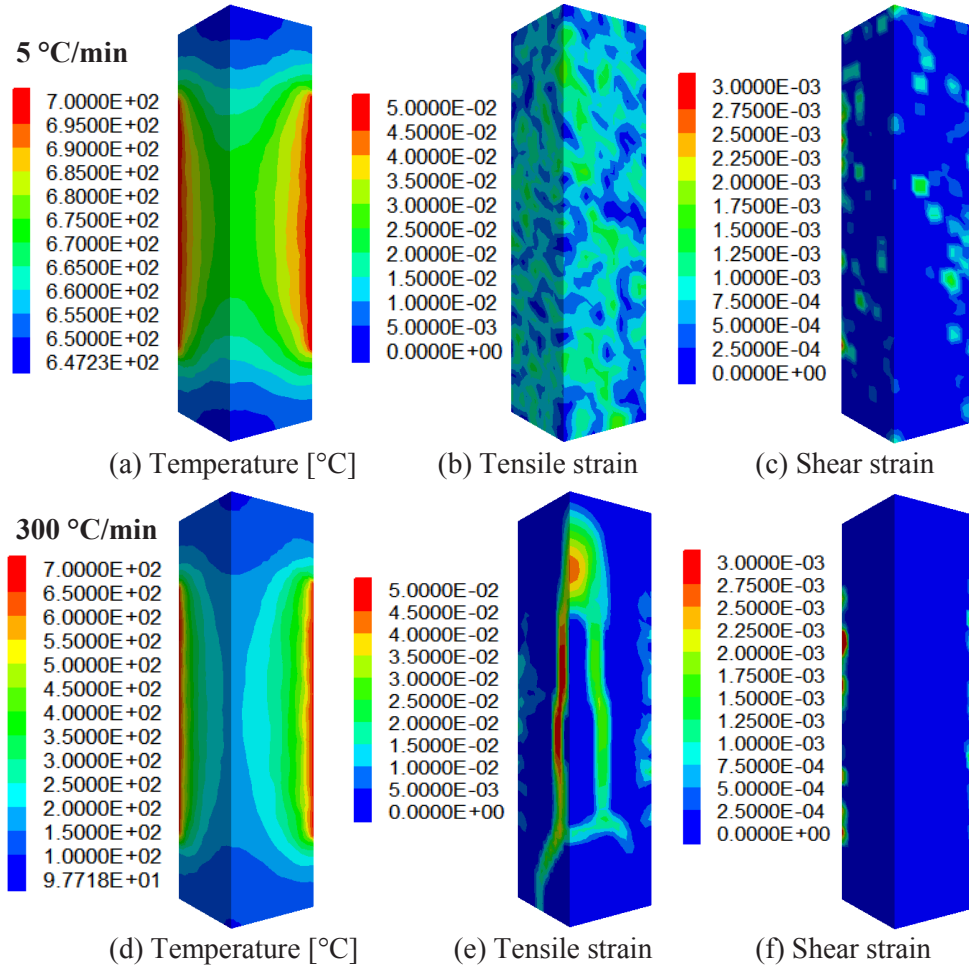
Figure 7-13 Simulation results of sample heated to 700 °C applying different heating rates

(a) 5 °C/min　　　(b) 300 °C/min
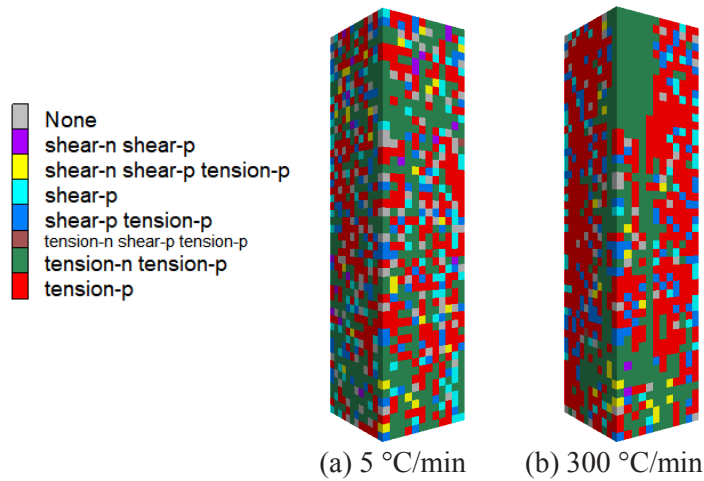
Figure 7-14 Plasticity state of sample heated to 700 °C after 1 hour holding time

7.2.2 Thermo-mechanical behavior of EG according to ISO 834 fire curve

Figure 7-15 shows the UCS of EG at 700 °C (i.e. 800 °C in lab testing) applying different heating rates. The heating rates show an influence on the strength of granite to some extent but the influence is relatively small (also see Figure 7-12). This finding is the same as in lab tests (see chapter 3.1)

Figure 7-16 shows plasticity states in numerical models heated to different temperatures up to 700 °C (i.e. 800 °C in lab testing) according to ISO 834 fire curve. Tensile failures begin to occur when sample surface temperature reaches about 200 °C (Figure 7-16a) in the direct heating area (see Figure 7-11). Microcracks are induced continuously when temperature increases and propagate across the whole sample after 500 °C. Most elements fail in tension at elevated temperatures, and shear failure begins to develop quickly after 500 °C.
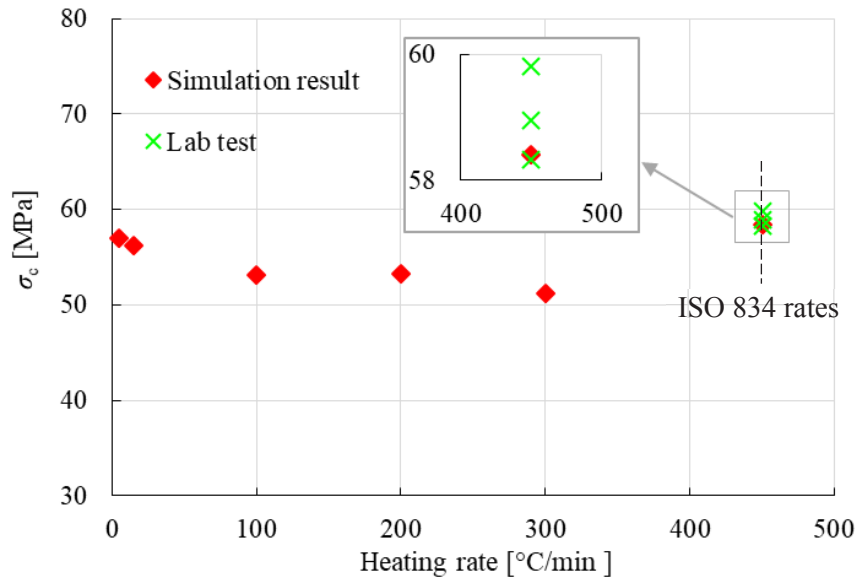
Figure 7-15 UCS of EG at 700 °C (i.e. 800 °C in lab testing) applying different heating rates

Figure 7-17a shows the temperature distribution of EG sample heated-up to 500 °C, 600 °C, and 700 °C. At 600 °C, the inside temperatures are around 400 to 500 °C in most parts. This means the α-β quartz transition only occurs in the surface area. The temperatures of most parts of the sample exceed the quartz transition temperature after heated-up to 700 °C. Therefore, the quartz transition happened inside of the sample heated-up to over 700 °C. From Figure 7-16 we can see that shear

failures have a significant increase after the α-β quartz transition, which has a great impact on the reduction of granite strength.

The cracks are mainly widened after the quartz transition (Figure 7-17b), which is also true for slow heating scenarios.
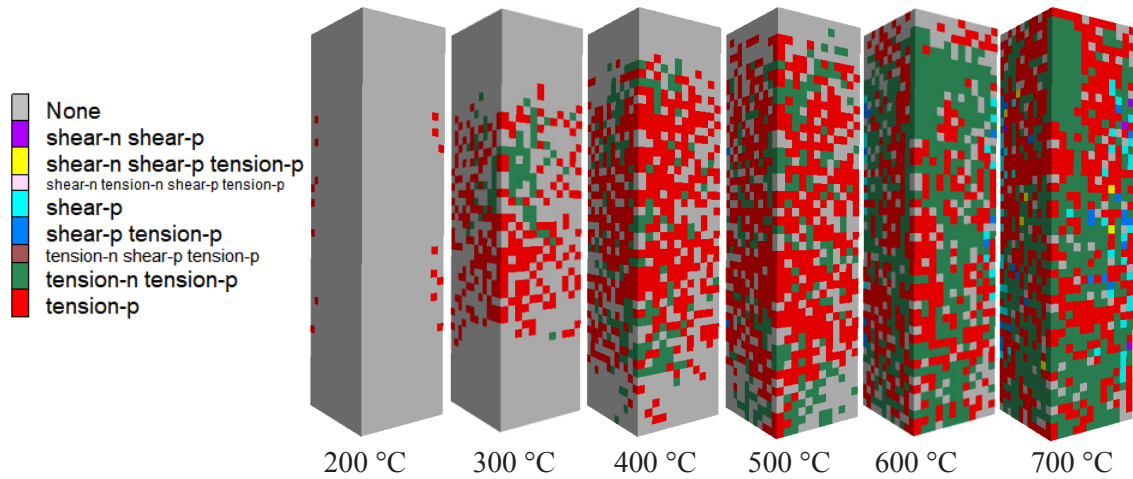
Figure 7-16 Plasticity states of samples heated-up to different temperatures up to 700 °C (i.e. 800 °C in lab testing) with ISO 834 fire curve

(a) Temperature distribution [°C] (b) Plastic tensile strain
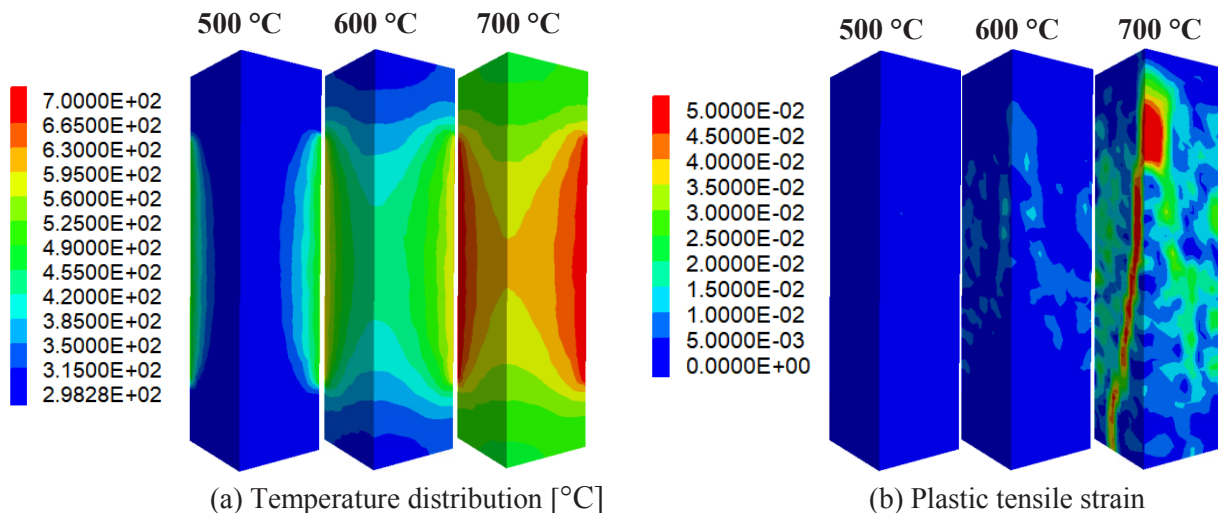
Figure 7-17 Simulation results of models heated-up to different temperatures

117

8 Conclusions and outlook

8.1 Main conclusions

The influence of temperature and heating rate on mechanical properties (i.e. Young's modulus, UCS, peak axial strain, and strength parameters) and failure mode of Eibenstock granite under elevated temperatures have been studied. Supersonic frequency induction heating systems seem to be suited to perform lab tests with high speed heating rates and can even reproduce the non-linear ISO 834 standard fire temperature-time curve. The maximum temperature has the dominant impact on the mechanical properties of granite samples, while the influence of heating rates is relatively small. The small property variation in respect to different heating rates is caused by a different induced crack pattern.

The impact of temperature up to 1000 °C on physical, mechanical and thermal properties as well as thermo-mechanical coupled behavior of EG were investigated. The physical properties including mineral composition, density, P-wave velocity, and open porosity are measured to be temperature-dependent. P-wave velocity and porosity variations indicate continuously induced crack evolution at elevated temperatures and pronounced crack coalescence from 600 °C to 1000 °C. Uniaxial compression and Brazilian tests were carried out to measure UCS, Young's modulus, stress-strain relationship, and tensile strength of EG before and after thermal treatment, respectively. Test results show that UCS slightly increases from 25 °C to 400 °C before decreasing rapidly up to 1000 °C, while Young's modulus and tensile strength decrease continuously with rising temperature. Failure characteristics change from brittle failure up to a temperature of 600 °C to ductile behavior at 800 °C and 1000 °C.

The numerical simulation code FLAC^{3D} was used to develop a numerical scheme to simulate the thermal induced damage of granite at high temperatures. Based on an extensive analysis of existing data, general relations between temperature and several thermo-mechanical parameters were established. Several versions of the well-known Mohr-Coulomb constitutive model with tension cut-off and strain softening were extended by the established thermo-mechanical parameter relations to investigate the potential of realistic simulation of thermal induced damage. Statistical methods combined with real mineral composition were used to characterize the heterogeneity of

granite. Simulation results reveal the importance of thermo-mechanical property distributions at the grain size level for the overall thermo-mechanical behaviors at larger scale. The proposed numerical model can well reproduce the lab results of thermal induced micro- and macro-cracks, as well as the stress–strain behavior and the final failure pattern of granite after heat treatments.

The speed of heating can influence the crack pattern significantly. The simulation results also reveal that the thermal induced microcracks at slow heating scenarios are randomly distributed across the whole sample, while several major cracks will form before the homogeneous distribution of microcracks for granite with high-speed heating. The small strength variation in respect to different heating rates is caused by a different induced crack pattern. Although most thermal induced damages are tensile failures, shear failure begins to develop quickly after 500 °C / 600 °C depending on heating speed. UCS reduction of granite due to heating is greatly influenced by the increase of shear failures. The simulation also shows that the dominant impact of the α-β quartz transition is widening pre-existing cracks rather than forming new microcracks.

8.2 Limitation and Recommendations for future work

Although a great progress has been made on investigating the thermal cracking of granite in both lab test and numerical simulation, further efforts are still necessary to extend the findings achieved.

(1) The mechanical property variations of granite are likely very small considering the influence of slow and high-speed heating rates. However, the variations of thermal properties remain unknown. Especially the thermal expansion coefficient could have a significant impact on the stress variation and deformation of granite materials. Knowing the heating-rate dependence of thermal properties can help to obtain more reliable simulation results in respect to the thermo-mechanical behavior of granite.

(2) The investigation of the cooling process is limited in this thesis. Some preliminary tests have indicated the complexity of the influence of the cooling process on crack closure. The mechanical behavior of granite might be affected by the factors including the maximum temperature, heating rate, sample size, material properties, cooling method (e.g. furnace, air, water cooling) etc. More

comprehensive tests are still necessary to investigate how cooling rate influences the mechanical properties of granite.

(3) A reliable simulation of the thermo-mechanical behavior induced by cooling is greatly influenced by accurate expansion/contraction coefficients during cooling. Since the mineral phase transition is reversible and the cracks tend to close during the cooling process, the thermal parameters become more complicated than during heating. Moreover, the parameter values might become significantly different in dependence on the cooling methods, especially in case of water cooling.

References

Ackermann RJ, Sorrell CA (1974) Thermal expansion and the high–low transformation in quartz. I. High-temperature X-ray studies. J Appl Crystallogr 7:461–467. doi: 10.1107/S0021889874010211

Bauer SJJ, Johnson B (1979) Effects Of Slow Uniform Heating On The Physical Properties Of The Westerly And Charcoal Granites. Proc 20th US Symp Rock Mech 7–18

Brotóns V, Tomás R, Ivorra S, Alarcón JC (2013) Temperature influence on the physical and mechanical properties of a porous rock: San Julian's calcarenite. Eng Geol 167:117–127. doi: 10.1016/j.enggeo.2013.10.012

Cao W, Zhao M, Liu C (2004) Study on the model and its modifying method for rock softening and damage based on Weibull random distribution. Chinese J Rock Mech Eng 23:3226–3231

Chaki S, Takarli M, Agbodjan WP (2008) Influence of thermal damage on physical properties of a granite rock: Porosity, permeability and ultrasonic wave evolutions. Constr Build Mater 22:1456–1461. doi: 10.1016/j.conbuildmat.2007.04.002

Chayé d'Albissin M, Sirieys P (1989) Thermal deformability of rocks: relation to rock structure. In: Rock at Great Depth, Maury & Fourmaintraux. Balkema, Rotterdam, pp 363–370

Chen S, Yang C, Wang G (2017a) Evolution of thermal damage and permeability of Beishan granite. Appl Therm Eng 110:1533–1542. doi: 10.1016/j.applthermaleng.2016.09.075

Chen S, Yue ZQ, Tham LG (2004) Digital image-based numerical modeling method for prediction of inhomogeneous rock failure. Int J Rock Mech Min Sci 41:939–957. doi: 10.1016/j.ijrmms.2004.03.002

Chen W, Konietzky H (2014) Simulation of heterogeneity, creep, damage and lifetime for loaded brittle rocks. Tectonophysics 633:164–175. doi: 10.1016/j.tecto.2014.06.033

Chen Y, Wang S, Ni J, et al (2017b) An experimental study of the mechanical properties of granite after high temperature exposure based on mineral characteristics. Eng Geol 220:234–242. doi: 10.1016/j.enggeo.2017.02.010

Clauser C, Huenges E (1995) Thermal Conductivity of Rocks and Minerals. In: Ahrens TJ (ed) Rock Physics & Phase Relations: A Handbook of Physical Constants. American Geophysical Union, pp 105–126

Cooper HW, Simmons G (1977) The effect of cracks on the thermal expansion of rocks. Earth Planet Sci Lett 36:404–412. doi: 10.1016/0012-821X(77)90065-6

Dai Y, Gruber D, Harmuth H (2017) Observation and quantification of the fracture process zone

for two magnesia refractories with different brittleness. J Eur Ceram Soc 37:2521–2529. doi: 10.1016/j.jeurceramsoc.2017.02.005

Davidge RW, Green TJ (1968) The strength of two-phase ceramic/glass materials. J Mater Sci 3:629–634. doi: 10.1007/BF00757910

Davies IJ (2001) Empirical correction factor for the best estimate of Weibull modulus. J Mater Sci Lett 20:997–999

Deng B, Jiang D (2017) Determination of the Weibull parameters from the mean value and the coefficient of variation of the measured strength for brittle ceramics. J Adv Ceram 6:149–156. doi: 10.1007/s40145-017-0227-3

DIN EN 1936 (2007) Natural stone test method - Determination of real density and apparent density, and of total and open porosity. Deutsches Institut für Normung [DIN], Berlin, Germany

Dinh QD (2011) Brazilian Test on Anisotropic Rocks – Laboratory Experiment , Numerical Simulation and Interpretation, PhD Thesis. Technischen Universität Bergakademie Freiberg

Dong J, Zhu H, Chen D (2015) Universal elastic-hardening-driven mechanical instability in α-quartz and quartz homeotypes under pressure. Sci Rep 5:1–9. doi: 10.1038/srep10810

Dwivedi RD, Goel RK, Prasad VVR, Sinha A (2008) Thermo-mechanical properties of Indian and other granites. Int J Rock Mech Min Sci 45:303–315. doi: 10.1016/j.ijrmms.2007.05.008

Fei Y (1995) Thermal expansion. Rock Phys Phase Relations 29–44. doi: 10.1029/RF002p0029

Fourmeau M, Gomon D, Vacher R, et al (2014) Application of DIC Technique for Studies of Kuru Granite Rock under Static and Dynamic Loading. Procedia Mater Sci 3:691–697. doi: 10.1016/j.mspro.2014.06.114

Freire-Lista DM, Fort R, Varas-Muriel MJ (2016) Thermal stress-induced microcracking in building granite. Eng Geol 206:83–93. doi: 10.1016/j.enggeo.2016.03.005

Friedman M, Handin JN, Higgs G, Lantz JR (1979) Strength and ductility of four dry igneous rocks at low pressures and temperatures to partial melting. Proc Symp Rock Mech, Balkema, Rotterdam 35-50 pp

Gao F, Guan X, Zhu H, Ye Y (2018) Fire-Resistance Behavior of Completely Overlapped Tubular Joints under Lap Brace Axial Loading. J Struct Eng (United States) 144:1–16. doi: 10.1061/(ASCE)ST.1943-541X.0002130

Gautam PK, Verma AK, Maheshwar S, Singh TN (2016) Thermomechanical Analysis of Different Types of Sandstone at Elevated Temperature. Rock Mech Rock Eng 49:1985–1993. doi:

10.1007/s00603-015-0797-8

Glover PWJJ, Baud P, Darot M, et al (1995) α/β phase transition in quartz monitored using acoustic emissions. Geophys J Int 120:775–782. doi: 10.1111/j.1365-246X.1995.tb01852.x

Gomez-Heras M, McCabe S, Smith BJ, Fort R (2009) Impacts of fire on stone-built Heritage: An overview. J Archit Conserv 15:47–58. doi: 10.1080/13556207.2009.10785047

Griffiths L, Lengliné O, Heap MJ, et al (2018) Thermal Cracking in Westerly Granite Monitored Using Direct Wave Velocity, Coda Wave Interferometry, and Acoustic Emissions. J Geophys Res Solid Earth 123:2246–2261. doi: 10.1002/2017JB015191

Hajpál M (2010) Fire Damaged Stone Structures in Historical Monuments . Laboratory Analyses of Changes in Natural Stones by Heat Effect. Building 164–173

Hajpál M (2002) Changes in sandstones of historical monuments exposed to fire or high temperature. Fire Technol 38:373–382. doi: 10.1023/A:1020174500861

Hamidouche M, Bouaouadja N, Olagnon C, Fantozzi G (2003) Thermal shock behaviour of mullite ceramic. Ceram Int 29:599–609. doi: 10.1016/S0272-8842(02)00207-9

Hartlieb P, Toifl M, Kuchar F, et al (2016) Thermo-physical properties of selected hard rocks and their relation to microwave-assisted comminution. Miner Eng 91:34–41. doi: 10.1016/j.mineng.2015.11.008

Heap MJ, Lavallée Y, Laumann A, et al (2013) The influence of thermal-stressing (up to 1000 °c) on the physical, mechanical, and chemical properties of siliceous-aggregate, high-strength concrete. Constr Build Mater 42:248–265. doi: 10.1016/j.conbuildmat.2013.01.020

Heuze FE (1983) High-temperature mechanical, physical and Thermal properties of granitic rocks— A review. Int J Rock Mech Min Sci Geomech Abstr 20:3–10

Heuze FE (1981) Geotechnical Modeling of High-Level Nuclear Waste Disposal by Rock Melting (No. UCRL-53183)

Hidnert P, Dickson G (1945) Some physical properties of mica. J Res Natl Bur Stand (1934) 35:309–353

Homand-Etienne F, Houpert R (1989) Thermally induced microcracking in granites: characterization and analysis. Int J Rock Mech Min Sci 26:125–134. doi: 10.1016/0148-9062(89)90001-6

Huotari T, Kukkonen I (2004) Thermal expansion properties of rocks : literature survey and estimation of thermal expansion coefficient for Olkiluoto mica gneiss. 15–19

Inserra C, Biwa S, Chen Y (2013) Influence of thermal damage on linear and nonlinear acoustic

properties of granite. Int J Rock Mech Min Sci 62:96–104. doi: 10.1016/j.ijrmms.2013.05.001

ISO 834-1 (1999) Fire resistance tests – elements of building construction – part 1: general requirements. Geneva, Switzerland

ISRM (1979) Suggested methods for determining the uniaxial compressive strength and deformability of rock materials. Int J Rock Mech Min Sci Geomech Abstr 16:137–140. doi: 10.1016/0148-9062(79)91450-5

ISRM (1978) Suggested methods for determining tensile strength of rock materials. Int J Rock Mech Min Sci Geomech Abstr 15:99–103

Itasca (2019) FLAC3D Fast Lagrangian Analysis of Continua in 3 Dimensions -FLAC3D 7.0 Documentation

James JD, Spittle JA, Brown SGR, Evans RW (2001) A review of measurement techniques for the thermal expansion coefficient of metals and alloys at elevated temperatures. Meas Sci Technol 12:R1–R15. doi: 10.1088/0957-0233/12/3/201

Jiao YY, Zhang XL, Zhang HQ, et al (2015) A coupled thermo-mechanical discontinuum model for simulating rock cracking induced by temperature stresses. Comput Geotech 67:142–149. doi: 10.1016/j.compgeo.2015.03.009

Johnson B, Gangi AF, Handin J (1978) Thermal cracking of rock subjected to slow, uniform temperature changes. Procedings 19th US Symp Rock Mech 19:259–267. doi: 10.1016/0148-9062(79)91483-9

Kumari WGP, Ranjith PG, Perera MSA, et al (2017a) Mechanical behaviour of Australian Strathbogie granite under in-situ stress and temperature conditions: An application to geothermal energy extraction. Geothermics 65:44–59. doi: 10.1016/j.geothermics.2016.07.002

Kumari WGP, Ranjith PG, Perera MSA, et al (2017b) Temperature-dependent mechanical behaviour of Australian Strathbogie granite with different cooling treatments. Eng Geol 229:31–44. doi: 10.1016/j.enggeo.2017.09.012

Kwok CY, Duan K (2015) DEM simulation of fracture process of inherently anisotropic rock under Brazilian test condition. 49th US Rock Mech / Geomech Symp 2015 2:

Larsson K (2006) Fires in tunnels and their effect on rock. Luleå University of Technology Department

Li GQ, Zhang C, Lou GB, et al (2012) Assess the Fire Resistance of Intumescent Coatings by Equivalent Constant Thermal Resistance. Fire Technol 48:529–546. doi: 10.1007/s10694-

011-0243-8

Li XF, Li HB, Zhao J (2017) 3D polycrystalline discrete element method (3PDEM) for simulation of crack initiation and propagation in granular rock. Comput Geotech 90:96–112. doi: 10.1016/j.compgeo.2017.05.023

Lin W (2002) Permanent strain of thermal expansion and thermally induced microcracking in Inada granite. J Geophys Res Solid Earth 107:ECV 3-1-ECV 3-16. doi: 10.1029/2001JB000648

Lindroth D, Krawza W (1971) Heat content and specific heat of six rock types at temperatures to 1000°C. [Washington, D.C.] : U.S. Dept. of Interior, Bureau of Mines

Liu HY, Roquete M, Kou SQ, Lindqvist PA (2004) Characterization of rock heterogeneity and numerical verification. Eng Geol 72:89–119. doi: 10.1016/j.enggeo.2003.06.004

Mahabadi OK, Tatone BSAA, Grasselli G (2014) Influence of microscale heterogeneity and microstructure on the tensile behavior of crystalline rocks. J Geophys Res Solid Earth 119:5324–5341. doi: 10.1002/2014JB011064

Mckinstry H a. (1965) Thermal expansion of clay minerals. Am Mineral 50:212–222

Nasseri MHB, Schubnel A, Young RP (2007) Coupled evolutions of fracture toughness and elastic wave velocities at high crack density in thermally treated Westerly granite. Int J Rock Mech Min Sci 44:601–616. doi: 10.1016/j.ijrmms.2006.09.008

Nasseri MHB, Tatone BSA, Grasselli G, Young RP (2009) Fracture toughness and fracture roughness interrelationship in thermally treated westerly granite. Pure Appl Geophys 166:801–822. doi: 10.1007/s00024-009-0476-3

Nordlund E, Zhang P, Dineva S, et al (2014) Impact of fire on the stability of hard rock tunnels in Sweden. Stiftelsen bergteknisk forskning-Befo, Stockholm

Pabst W, Gregorová E, Uhlířová T, Musilová A (2013) Elastic properties of mullite and mullite-containing ceramics part 1: Theoretical aspects and review of monocrystal data. Ceram - Silikaty 57:265–274

Pan B, Qian K, Xie H, Asundi A (2009) Two-dimensional digital image correlation for in-plane displacement and strain measurement: A review. Meas Sci Technol 20:. doi: 10.1088/0957-0233/20/6/062001

Polyakova IG (2014) The main silica phases and some of their properties. In: Schmelzer JWP (ed) Glass: Selected Properties and Crystallization. DE GRUYTER, Berlin, pp 197–268

Ramana Y V., Sarma LP (1980) Thermal expansion of a few Indian granitic rocks. Phys Earth Planet Inter 22:36–41. doi: 10.1016/0031-9201(80)90098-9

Renteria JD, Ramirez S, Malekpour H, et al (2015) Strongly Anisotropic Thermal Conductivity of Free-Standing Reduced Graphene Oxide Films Annealed at High Temperature. Adv Funct Mater 25:4664–4672. doi: 10.1002/adfm.201501429

Richter D, Simmons G (1974) Thermal Expansion Behavior of Igneous Rocks. Int J Rock Mech Min Sci 11:403–411

Robertson EC (1988) Thermal Properties of Rocks. US Dep Inter Geol Surv 88–441

Rodrigues JPC, Laím L (2017) Fire resistance of restrained composite columns made of concrete filled hollow sections. J Constr Steel Res 133:65–76. doi: 10.1016/j.jcsr.2017.02.011

Romine WL, Whittington AG, Nabelek PI, Hofmeister AM (2012) Thermal diffusivity of rhyolitic glasses and melts: Effects of temperature, crystals and dissolved water. Bull Volcanol 74:2273–2287. doi: 10.1007/s00445-012-0661-6

Saiang C, Miskovsky K (2011) Effect of heat on the mechanical properties of selected rock types – a laboratory study. In: 12th ISRM Congress. International Society for Rock Mechanics and Rock Engineering

Shao S, Ranjith PG, Wasantha PLP, Chen BK (2015) Experimental and numerical studies on the mechanical behaviour of Australian Strathbogie granite at high temperatures: An application to geothermal energy. Geothermics 54:96–108. doi: 10.1016/j.geothermics.2014.11.005

Shao S, Wasantha PLP, Ranjith PG, Chen BK (2014) Effect of cooling rate on the mechanical behavior of heated Strathbogie granite with different grain sizes. Int J Rock Mech Min Sci 70:381–387. doi: 10.1016/j.ijrmms.2014.04.003

Siegesmund S, Snethlage R (2013) Stone in Architecture, 4th edn. Springer Berlin Heidelberg, Berlin, Heidelberg

Sippel J, Siegesmund S, Weiss T, et al (2007) Decay of natural stones caused by fire damage. Geol Soc London, Spec Publ 271:139–151. doi: 10.1144/gsl.sp.2007.271.01.15

Szumiga M (2015) A Comparison of the Rise of the Temperature of an Unprotected Steel Column Subjected to the Standard Fire Curve ISO 834 and to a Natural Fire Model. 157–170

Tan X (2013) Hydro-mechanical coupled behavior of brittle rocks - laboratory experiments and numerical simulations. Technischen Universität Bergakademie Freiberg

Tan X, Konietzky H, Chen W (2016) Numerical simulation of heterogeneous rock using discrete element model based on digital image processing. Rock Mech Rock Eng 49:4957–4964. doi: 10.1007/s00603-016-1030-0

Tham LG, Cheung YK, Tang CA (2001) Numerical simulation of the failure process of rocks.

Tamkang J Sci Eng 4:239–252

Tian H, Kempka T, Yu S, Ziegler M (2016) Mechanical Properties of Sandstones Exposed to High Temperature. Rock Mech Rock Eng 49:. doi: 10.1007/s00603-015-0724-z

Török A, Török Á (2015) The effect of temperature on the strength of two different granites. Cent Eur Geol 58:356–369. doi: 10.1556/24.58.2015.4.5

Tribaudino M, Angel RJ, Cámara F, et al (2010) Thermal expansion of plagioclase feldspars. Contrib to Mineral Petrol 160:899–908. doi: 10.1007/s00410-010-0513-3

Vales F, Rezakhanlou R (1999) Determination of the fracture mechanical parameters of porous ceramics from microstructure parameters measured by quantitative image analysis. J Mater Sci 4:4081–4088. doi: 10.1023/A:1004632503249

Van der Molen I (1981) The shift of the α-β transition temperature of quartz associated with the thermal expansion of granite at high pressure. Tectonophysics 73:323–342

Vázquez P, Shushakova V, Gómez-Heras M (2015) Influence of mineralogy on granite decay induced by temperature increase: Experimental observations and stress simulation. Eng Geol 189:58–67. doi: 10.1016/j.enggeo.2015.01.026

Vignjevic R, Djordjevic N, Vuyst T De, Gemkow S (2018) Modelling of strain softening materials based on equivalent damage force. Comput Methods Appl Mech Eng 335:52–68. doi: 10.1016/j.cma.2018.01.049

Wang F, Konietzky H (2019) Thermo-Mechanical Properties of Granite at Elevated Temperatures and Numerical Simulation of Thermal Cracking. Rock Mech Rock Eng. doi: 10.1007/s00603-019-01837-1

Wang F, Konietzky H, Frühwirt T, Dai Y (2020) Laboratory testing and numerical simulation of properties and thermal-induced cracking of Eibenstock granite at elevated temperatures. Acta Geotech 8:. doi: 10.1007/s11440-020-00926-8

Wang HF, Bonner BP, Carlson SR, et al (1989) Thermal stress cracking in granite. J Geophys Res 94:1745. doi: 10.1029/JB094iB02p01745

Wang Y (2015) Numerical modelling of heterogeneous rock breakage behaviour based on texture images. Miner Eng 74:130–141. doi: 10.1016/j.mineng.2014.12.030

Wei C (2015) Damage characteristics of brittle rocks inside the pre-failure range : numerical simulation and lab testing. Technischen Universität Bergakademie Freiberg

Weibull W (1951) A statistical distribution function of wide applicability. J Appl Mech 103:293–297

Weinhold S (2018) Changes of mechanical properties and mineralogical composition of Eibenstock granite through thermal treatment (in German). Technische Universität Bergakademie Freiberg

Wen H, Lu JH, Xiao Y, Deng J (2015) Temperature dependence of thermal conductivity, diffusion and specific heat capacity for coal and rocks from coalfield. Thermochim Acta 619:41–47. doi: 10.1016/j.tca.2015.09.018

Wikipedia (2019) Notre-Dame de Paris fire. https://en.wikipedia.org/wiki/Notre-Dame_de_Paris_fire. Accessed 15 Apr 2019

Xia K, Yao W (2015) Dynamic rock tests using split Hopkinson (Kolsky) bar system - A review. J Rock Mech Geotech Eng 7:27–59. doi: 10.1016/j.jrmge.2014.07.008

Xie X, Cheng Y, Wu K, Xiao B (2012) Study on α-β quartz phase transition and its effect on dielectric properties. J Appl Phys 111:104116. doi: 10.1063/1.4722217

Xu T, Zhou GL, Heap MJ, et al (2017) The Influence of Temperature on Time-Dependent Deformation and Failure in Granite: A Mesoscale Modeling Approach. Rock Mech Rock Eng 50:2345–2364. doi: 10.1007/s00603-017-1228-9

Xu X, Gao F, Zhang Z (2014) Research on triaxial compression test of granite after high temperatures. Rock Soil Mech 35:3177－83

Yang S-Q, Ranjith PG, Jing H-W, et al (2017) An experimental investigation on thermal damage and failure mechanical behavior of granite after exposure to different high temperature treatments. Geothermics 65:180–197. doi: 10.1016/j.geothermics.2016.09.008

Yang SQ, Tian WL, Huang YH (2018) Failure mechanical behavior of pre-holed granite specimens after elevated temperature treatment by particle flow code. Geothermics 72:124–137. doi: 10.1016/j.geothermics.2017.10.018

Yin T, Li X, Cao W (2015) Effects of thermal treatment on tensile strength of Laurentian granite using Brazilian test. Rock Mech Rock Eng 2213–2223. doi: 10.1007/s00603-015-0712-3

Yong C, Wang C -y (1980) Thermally induced acoustic emission in westerly granite. Geophys Res Lett 7:1089–1092. doi: 10.1029/GL007i012p01089

Yu Q, Zheng C, Yang T, et al (2012) Meso-structure characterization based on coupled thermal-mechanical model for rock failure process and applications. Chinese J Rock Mech Eng 31:42–51

Žák J, Vyhnálek B, Kabele P (2006) Is there a relationship between magmatic fabrics and brittle fractures in plutons?. A view based on structural analysis, anisotropy of magnetic

susceptibility and thermo-mechanical modelling of the Tanvald pluton (Bohemian Massif). Phys Earth Planet Inter 157:286–310. doi: 10.1016/j.pepi.2006.05.001

Zhao XG, Zhao Z, Guo Z, et al (2018) Influence of Thermal Treatment on the Thermal Conductivity of Beishan Granite. Rock Mech Rock Eng 1–20. doi: 10.1007/s00603-018-1479-0

Zhao Z (2016) Thermal influence on mechanical properties of granite: a microcracking perspective. Rock Mech Rock Eng 49:747–762. doi: 10.1007/s00603-015-0767-1

Zhou J, Zhang L, Yang D, et al (2017) Investigation of the quasi-brittle failure of Alashan granite viewed from laboratory experiments and grain-based discrete element modeling. Materials (Basel) 10:. doi: 10.3390/ma10070835

Zuo JP, Sun JWY, Chen Y, et al (2017) Effects of thermal treatment on fracture characteristics of granite from Beishan, a possible high-level radioactive waste disposal site in China. Eng Fract Mech 182:425–437. doi: 10.1016/j.engfracmech.2017.04.043